Graduate Theses and Dissertations   Graduate School

July 2018

Selective Sensing in Hybrid Imagers with Vertically Integrated Perovskite Pixels

Fatemeh Rahimi

University of South Florida, frahimi@mail.usf.edu

Follow this and additional works at: https://scholarcommons.usf.edu/etd

Part of the Engineering Commons

www.manaraa.com

Selective Sensing in Hybrid Imagers with Vertically Integrated Perovskite Pixels

by

Fatemeh Rahimi

A dissertation submitted in partial fulfillment
of the requirements for the degree of
Doctor of Philosophy in Electrical Engineering
Department of Electrical Engineering
College of Engineering
University of South Florida

Major Professor: Andrew M. Hoff, Ph.D.
Christos S. Ferekides, Ph.D.
John N. Kuhn, Ph.D.
Shengqian Ma, Ph.D.
Stephen E. Saddow, Ph.D.

Date of Approval:
June 29, 2018

Keywords: Image Sensor, Color Discrimination, Quantum Efficiency, Linear Dynamic Range, Defect Engineering

DEDICATION

This dissertation is dedicated to my beloved father, Dr. Hasan Rahimi, for his unconditional love and support in every step of my life specially my graduate studies. And to my dear mother, Mrs. Zahra Qorbani, who has always been my source of inspiration and encouragement.

ACKNOWLEDGMENTS

TABLE OF CONTENTS

LIST OF TABLES

LIST OF FIGURES

ABSTRACT

The rise of organometal halide perovskite materials with extremely intriguing properties have opened a new horizon in the design of high speed and low price optoelectronic devices. The bandgap in the crystalline structure of these materials can be easily tuned for various applications and their dominant non-excitonic dynamics eliminate the requirement of a bulk or heterostructure for charge carrier separation. These unique properties increase the photo-sensitivity of perovskite-based optoelectronics and provide them with a low time constant, resulting in high precision fast devices. Realization of perovskite-based devices translates directly to inexpensive and simplified architectures of optoelectronic systems.

In perovskite-based devices, costly silicon or wide bandgap semiconductor fabrication technology is largely replaced by solution processable methods. Their bandgap tunability allows the reduction of the required optical accessories and interconnects in optoelectronic components. For instance, a tuned perovskite-based detector can substitute a narrowband detecting system consisting of a conventional detector and its required optical accessories such as lenses and color filters. These properties of perovskite-based devices lead to the realization of inexpensive, low power and high-performance optoelectronic systems. In this work, the design of a narrowband, low noise, high performance and stable photodetector based on organic-inorganic hybrid perovskite structure is proposed. The full width at half maximum (FWHM) of the device would be in the nanometer range. The response of the device can be tuned using either

different ratios of the lead salts or synthetic dyes (macromolecules) in the crystalline structure for color discrimination in machine vision and imaging applications.

Non-excitonic photocarrier generation, tunability of the optical bandgap and low voltage requirements for charge carrier generation are the keys to the utility of this optoelectronic device. The goals of this project were to identify the required functional materials (lead salts and synthetic dyes based on their molecular structures) and optimize their performance; the study of their effect on the charge collection narrowing mechanism and bandwidth specifications defined for detectivity, linear dynamic range (LDR) and photoresponse speed. To achieve these goals, it was proposed to study the light detection properties as well as spectroscopic and semiconductor parameter characteristics of fabricated devices. The design considerations of such devices are versatile and may be modulated for different applications.

CHAPTER 1 : INTRODUCTION

The global market value of optoelectronic components is expected to exceed USD 55 billion by 2020 at CAGR of 18.83%, faster than any other existing industry. This forecast is merely attributed to the optoelectronics based on conventional semiconductors known for their low Fill Factor (FF) and high manufacturing costs. The market drive for these components is the emerging applications of the optoelectronics in the medical arena, machine vision, and artificial intelligence. Limited carbon-based natural resources and global warming considerations are other driving forces behind the increasing capital investment in optoelectronic components with energy generating capability[1]. Therefore, advancing the optoelectronics technology and achieving their theoretical limits are highly desired.

Application specific synthesis of new materials and facile manufacturing methods seem to be the key to eliminating the limiting factors in the manufacturing expenses of the optoelectronics and reaching their maximum theoretical efficiency[2]. Recently, a well-known material framework called perovskite has gained significant ground on its photosensitive compounds for optoelectronic applications[3]. This framework offers application-specific properties in optoelectronic components to source, detect and control light.

Photosensitive perovskite materials display remarkably high photoluminescence quantum efficiencies and have proven to be solid competitors of silicon-based ones[4]. The power conversion efficiency (PCE) in perovskite-based solar cells (PSCs) have skyrocketed from

1

3% to 22% in less than five years[5]. The solution processable nature of the thin film perovskites as well as other inexpensive deposition methods utilized in their processing justify the economic drive for their commercialization[6, 7]. Similar to every new technology, perovskite-based components require further modification to find their way to the market; in particular, their instability and toxicity must be addressed[8].

1.1. Prospect

In this dissertation, design, fabrication, and characterization of application-specific image sensors with greater color constancy and lower cost have been presented. Image sensors are one of the most prominent members of the optoelectronics family that detect and transfer the necessary information required to constitute an image. The current technology of the image sensors is based on the operational principles of Charged Coupled Devices (CCD)s and Complementary Metal Oxide Semiconductors (CMOS)s. The advent of photosensitive perovskites widens the horizon and further the advancement in image sensors provided their instability is properly addressed. A part of this dissertation is dedicated to root cause analysis of instability in these structures and elimination of the cause.

Perovskite-based image sensors offer bandwidth tunability over the visible spectrum which translates directly to light detection independent of varying background illumination. This concept has been exercised in the second part of this document. The effect of various dopants, organic compounds and synthetic molecules on the performance of these devices have been scrutinized. The unique properties of these electronic materials also eliminate the requirements for optical components such as filters and lenses. In this dissertation, the integration of these functional materials and conventional structures is studied. This document is concluded based

2

on a recipe for fabrication of filterless, narrowband perovskite-based image sensors with greater color constancy and lower cost using a chloride salt.

1.2. Motivation

The future market statistics in the field of optoelectronics and the changing landscape of their applications leave no doubt on the essential of further research and development in this industry. Undeniably, the conventional electronic materials such as silicon have transformed the technology and raised the standards of living. However, their intrinsic characteristics introduce compatibility issues related to the future market demands. Advanced functional materials are required to drive the highly flexible additive manufacturing techniques that fit into the requirements of the modern optoelectronics industry.

Perovskite framework with the generic formula of ABX_3 , shown in Figure 1.1, has been proven to offer the highest power conversion efficiency and flexibility as well as the lowest cost among other advanced materials[9]. This is derived from the fact that various elements can participate in forming the structure, a principal factor for light absorption. Different elements possess different absorption spectra. Hence, the absorption spectrum of the perovskite changes based on its constituent materials. This property can potentially feature reconfigurable and tunable optoelectronic components.

The perovskite crystalline structure is formed using low cost deposition techniques such as solution processing, easily adopted in additive manufacturing. The presence of perovskites eliminates the requirement of optical accessories in the architecture of the device. This also helps with further cost reduction justifying the fast pace towards commercialization of this new technology.
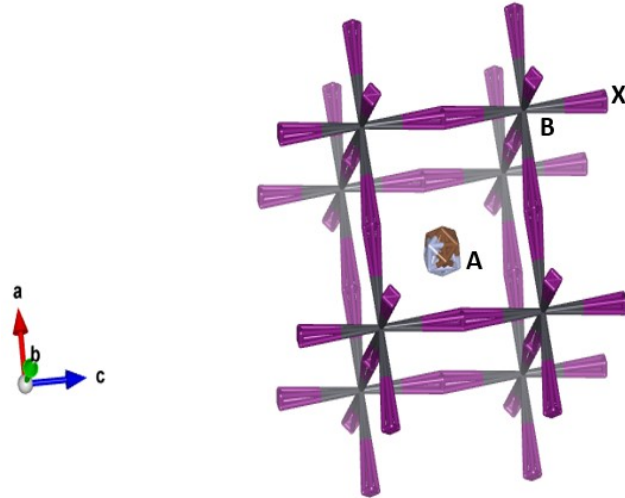
Figure 1.1. Perovskite framework filled with photosensitive compounds. Shown are methylammonium(A), lead (B) and iodide (X).

1.3. Methods

The superior light absorbing characteristics of organo-metal trihalide perovskites qualifies their application in optoelectronic transducer such as light emitting diodes, photodetectors and image sensors[3]. Once steady and stable, the tunable bandwidth of the perovskites offers unique photo-detecting properties; high color discrimination and constancy with no requirement for optical components such as filters or lenses.

To design and fabricate application specific perovskite-based image sensors, an electron hole separation mechanism must be implemented. A layered structure consisting of organo-metal halide perovskites sandwiched between electron and hole transporting layers constitute the basic structure of the device. The absorption bandwidth of the perovskites can be adjusted by changing the ratios of the halides in the perovskite compounds and administering various concentrations of micro-molecules. The principles of the bandwidth tunability is shown in Figure 1.2.

4
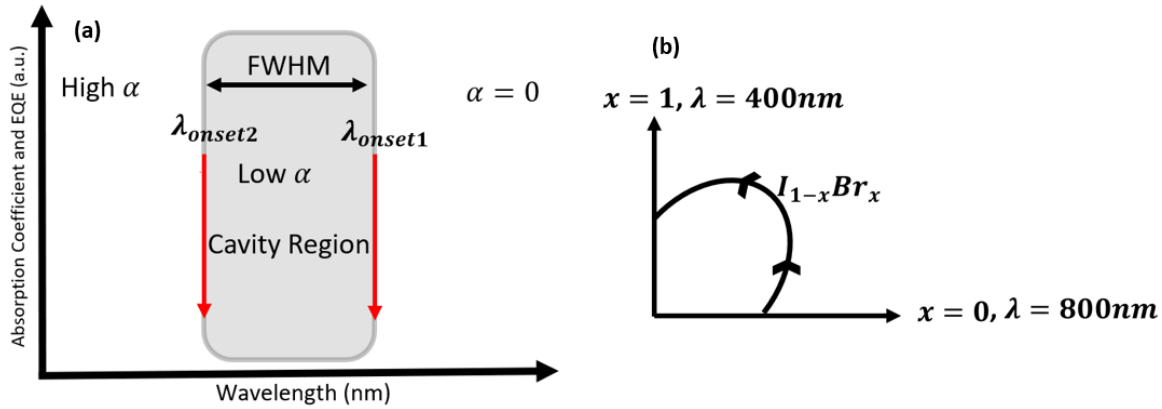
Figure 1.2. (a) Selective light detection technique using various ratios of halides for the lower limit (λ_{onset1}) and synthetic micro-molecules for the upper limit (λ_{onset2}). (b) A schematic of wavelength variation as a function of halide ratios.

1.4. Challenges

The recent certified PCE of 22.7% and the feasibility of PCEs around 30% through tandem structures with silicon or copper indium gallium selenide-based bottom cell and PSC top cell, necessitates further scrutiny to eliminate the toxicity and instability of the perovskites[8, 10-13]. The toxicity of perovskite is due to its lead atom well known as an environmentally hazardous heavy metal. However, it could not be considered as the main impediment in the commercialization of PSCs as seen in similar cases such as cadmium telluride (CdTe)[14]. CdTe thin film solar cells with PCE of above 22% occupy the largest portion of thin film photovoltaics in the market despite their carcinogenic nature[15]. In addition, well established lead recycling procedures have been developed for battery productions and would be applicable for the case of PSCs[16].

Regardless of the economic justification or available recycling techniques, the lead content in photovoltaics must be reduced. This would be possible using novel materials in the architecture of the optoelectronic components. For example, employing materials such as polymers with extensively large surface area allows application of an extremely thin layer of

5

perovskite material producing the same device performance as if a considerable amount of these crystalline structures is utilized[17]. The remaining issue on these emerging materials is their stability[18].

In this dissertation, the basic structure of electronic devices that source, detect and control the light were discussed. The design considerations in the conventional architecture of these devices versus those of the new class of optoelectronics were studied. Finally, the results of the projected research on perovskite-based optoelectronics were presented. Challenges and possible solutions were demonstrated. Recipes were developed on the fabrication of colored pixels for narrowband absorption.

CHAPTER 2 : LITERATURE REVIEW

This chapter provides an overview of the historical background of the imaging technology. It also includes a detailed discussion on the theoretical and practical aspects of image sensing technology from the invention of CCDs to Organic Light Emitting Diodes (OLED)s with the emphasis on the materials, photoactive perovskites, in the device architectures. The figures of merit of photodetectors/pixels are introduced and the optimization methods are described. The current challenges in the development process of the image sensors based on the perovskites, the possible resolutions and the possibilities to integrate this new generation of materials with conventional structures are discussed.

2.1. Background

Imaging or capturing visual representations of objects and living creatures is a technique based on transduction of optical energy to electrical energy. The photons emitted from the objects carry information regarding the color of the object in the form of energy; as the energy of each photon corresponds to a certain wavelength in the visible spectrum. The first practical color image sensor was invented in 1839 by Louis Daguerre. The technique involved unilateral chemical reactions on photosensitive materials[19]. The invention was superseded shortly after and evolved from silver-plated copper sheets polished to mirror finish, coated with photosensitive materials to roll films in 1881[20]. In less than a century, the semiconductor

7

industry offered an entirely new venue to the image sensing by the invention of Charged Coupled Devices (CCD)s[21].

Although the architecture of Complementary Metal-Oxide Semiconductors (CMOS)s was known before the invention of CCDs, their unstable threshold voltage delayed their imaging application[22]. CMOS image sensors were first developed in NASA jet propulsion labs by Eric Fossum in early 1990s[23]. The low power consumption of CMOS imagers as well as their inexpensive manufacture have overshadowed the higher light sensitivity and linear dynamic range of the CCDs[24]. As a result, digital image acquisition has been established mostly on the basis of CMOS technology[25]. In less than 20 years, CMOS image sensors have found their way to scientific, medical, entertainment and automotive applications as well as daily life. Their ubiquitous presence in the modern era has taken a new turn for the emerging applications such as machine vision, intelligent transport systems (ITS) or flexible medical imaging[26].

The progress in image processing and pattern recognition techniques relies on the advancement of the imaging technologies. Smart imagers with higher signal to noise ratios, greater linear dynamic range, more analog to digital functions, lower power consumption, higher fill factor, and interaction capability with a variety of interfaces are required. In addition, the processed images based on the current technology have always been a subject of color change depending on the brightness in the environment. This so-called "color constancy" challenge must be resolved for accuracy and precise detection applications.

The working principle of an image pixel is as follows: first, the photodiode must be reversed biased to a high voltage; second, a voltage drop occurs across the diode upon the exposure of the photosensitive materials to the photons; third, at the end of the exposure, the

8

remaining voltage across the diode is measured- the voltage difference is an indication of the number of photons impinging the photoactive area; fourth, the photodiode is reset for a new cycle[24]. The voltage change causes the accumulation of the charge carriers in a two-dimensional array that must be read-out. The detected charge carriers are then converted to digital data. An Application Specific Integrated Circuit (ASIC) processes the digital data to form the final image[27]. The read-out mechanism varies in different imaging systems. For example, CCDs require several clocking steps to be read-out whereas, in CMOS imagers, each pixel is read-out individually. Charge Injection Devices (CIDs) are read-out based on the concept of displacement current and in image pickup tubes the resulting current of scanning the cathode ray on the objects defines the final image or video[28].

Imaging requirements of each application results in changes in pixel sensing arrangement (passive or active), the architecture of the image sensor, integration of smart functions onto the image sensor chips, color-separation mechanisms and systems, selection of the photosensitive materials and image processing software[27, 29, 30]. Among all the forenamed considerations, the photosensitive materials play the most dominant role in determining the spectral response of the devices, their sensitivity, dynamic range, color accuracy and resolution. In addition, the physical properties of the image sensors such as flexibility and weight stem from the mechanical properties of their constructing photosensitive materials.

Image sensors may be classified as broadband (panchromatic) or narrowband (monochromatic) based on the absorption characteristics of their constructing photosensitive materials and their operating color separation mechanisms.

9

Inorganic semiconductors such as silicon (hydrogenated amorphous as well as crystalline) possess relatively high dielectric constants resulting in low exciton binding energies which make them suitable candidates for light absorption purposes of color imaging. Some of the prominent features of these inorganic semiconductors might be unfavorable for imaging purposes. For example, long carrier lifetime in silicon might cause crosstalk between the pixels. The materials by themselves are considered broadband and would require optical accessories to meet the specifications in color imaging. Silicon-based imagers are prone to undesired infrared (IR) sensitivity which necessitates the presence of IR filters. Also, these inorganic materials would never fulfill the requirements of flexible additive manufacturing on the horizon. The resolution to these challenges seems to be intertwined with the development of organic-based color imaging which offers a new set of possibilities for future advancements in medical and technological arenas.

2.2. Color Discrimination Techniques

There have been two major approaches for color imaging based on conventional semiconductors such as silicon or gallium arsenide. The first approach is developed based on the utilization of auxiliary structures such as filter arrays or lenses to detect photon with a specific wavelength. The second approach relies on the capability of the photoactive materials employed in the structure of the sensors to discriminate different colors. A detailed review on each approach is provided in the following sections:

2.2.1. Color Discrimination Based on the Auxiliary Structures

This approach results in broadband color imaging using conventional semiconductors and includes several different configurations.

2.2.1.1. Utilization of Bayer Filter Mosaic

In this configuration, a color filter array (CFA) is positioned on each sensor cell. There are twice as many Greens (G)s in Bayer's structure as Blues (B)s and Reds (R)s to emulate a biological human eye. In this configuration, the incident light is filtered onto the individual pixels of the imaging array. Consequently, two-thirds of the light are absorbed by the CFA resulting in lower quantum efficiency and spatial resolution in each pixel. Also, the space occupied by the CFAs limits the miniaturization scales. The final image must undergo an extra step of de-mosaicing which makes it prone to lower color constancy and quality. This configuration is mainly used in digital cameras shown in Figure 2.1(a).

2.2.1.2. Color Wheel

The auxiliary structure in this configuration is a color wheel that produces three consecutive images as it rotates 360 degrees. The final image is constructed based on the combination of these three images. This configuration is a subject of image distortion due to its low clock rate, shown in Figure 2.1(b).

2.2.1.3. Beam Splitter

In this configuration, a beam splitter diffracts the light to its three main colors and deploys each beam separately to its corresponding pixel. This method requires three separate pixels for sensing and called a three-chip system. This requirement puts a constraint on the miniaturization of this configuration, shown in Figure 2.1(c).

11

2.2.1.4. Integrated Metal Strips

Integration of 1D or 2D array of metal strips within each imaging cell called integrated color pixel (ICP) that results in simultaneous color separation and image capture. This configuration results in the least image distortion and highest resolution, shown in Figure 2.1(d).
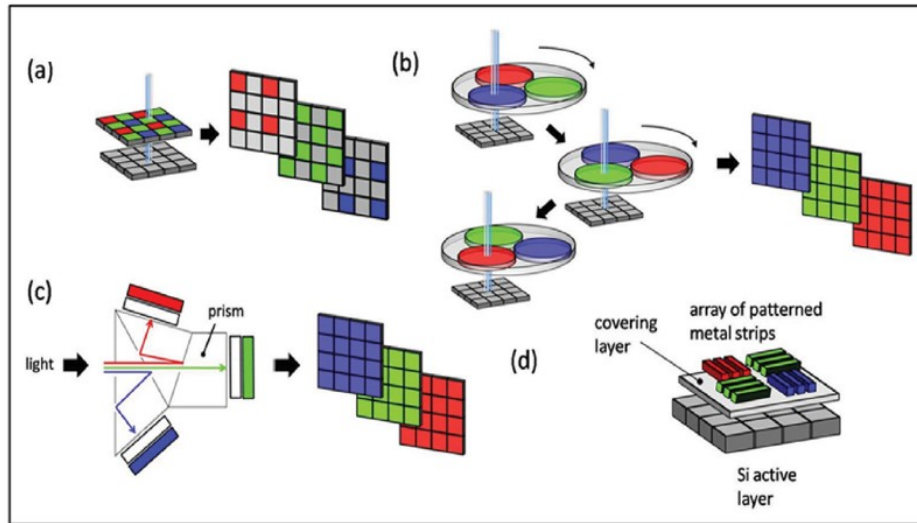
Figure 2.1. Color discrimination methods based on the auxiliary structures. Copyright permission is provided in the appendix[31]

There are several other developing technologies to overcome the low light transmission and lift the miniaturization constraint introduced due to the presence of the auxiliary structures. Diffractive filter arrays and plasmonic hole arrays are two of the many to improve the light absorption without manipulating the photosensitive materials. All these techniques add extra steps to the manufacturing process and increase the cost of the final product.

2.2.2. Color Discrimination Based on the Photosensitive Materials

This approach is based on the electromagnetic nature of light and its penetration depth. This approach has been practiced on two different configurations.

2.2.2.1. Stacking Color Pixels

The three-layer arrangement of color filters stacked on every single pixel allows the pixel to absorb all the three colors based on their penetration depth in the substrate and construct the final image. Although this method improves the fill factor, the cross talk between the layers still poses a real challenge in the development of this method, shown in Figure 2.2(a).

2.2.2.2. Transverse Field Effect

This approach relies on the manipulation of the electric field across the device and charge carrier generation in different depths within the substrate, shown in Figure 2.2(b).
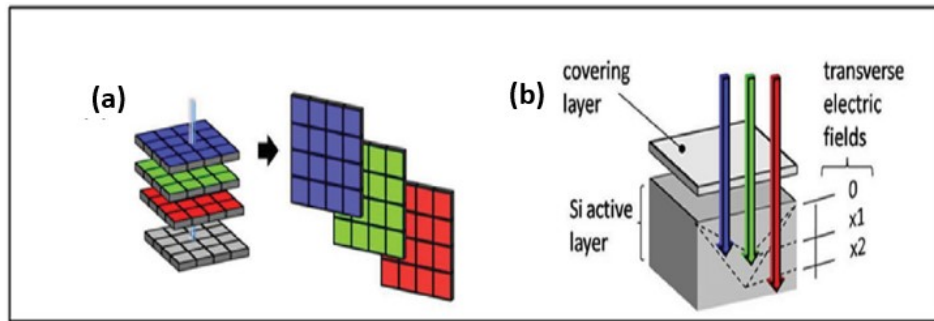
Figure 2.2. Color discrimination methods based on the photosensitive materials. Copyright permission is provided in the appendix[31]

There have been several attempts to replace the semiconducting bulks with nanostructures and quantum dots. The second approach has been the center of focus in research and development of high efficiency, filterless image sensors.

2.3. Color Constancy in Color Imaging

The term "color constancy" refers to a feature of the human color perception system. It is expected that the perceived color of an object must remain constant by an observer under varying illumination conditions. The current color imaging systems fail to capture color images that are independent of the characteristics of the illuminant. This problem is attributed to the

13

wideband absorption spectrum of the imagers. Most of the light is absorbed from the environment regardless of its origin, it may come from the object or its ambient. This light then contributes to the construction of the final image. The use of color filters also reduces the accuracy of color imaging as it confines the distribution of the color spectrum to only three main colors. The attempts to overcome this problem are acknowledgments of the shortcomings of the current technology.

2.4. Perovskites, Resolution to Color Constancy

The current technology based on the conventional semiconductors at its highest practical efficiency still experiences difficulties to maintain the pace with the demands of the future market[32]. Portability, flexibility, higher efficiency, lower cost and smaller size with smart functions are the required features for future optoelectronic components. These features can only be realized using perovskite semiconductor pigments[33]. As a framework, perovskite structures offer a variety of lattice phases and their facile formation techniques such as solution processing simplify their doping methods and bandwidth tunability[34]. In less than a decade from their emergence, perovskite-based photovoltaic cells have established the highest growth rate amongst others as shown in Figure 2.3.

The generic formula of the perovskite materials is ABX_3, with A as the organic, B as the lead and X as the halide site in organolead trihalide photoactive perovskites. The X site of such perovskites may contain various ratios of halides as long as they follow Vegard's empirical law[35]. The variations in the ratios of the halides slide their absorption spectrum along the visible range, e.g. for $I_{1-x}Br_x$ the wavelength varies from 800nm to 400nm as x varies from 0 to 1[36]. The A site contains organic molecules such as methylammonium (MA) or formamidinium

14

(FA) cations. The A site can be easily doped with cesium ions to enhance the carrier transportation characteristics of the component[36].
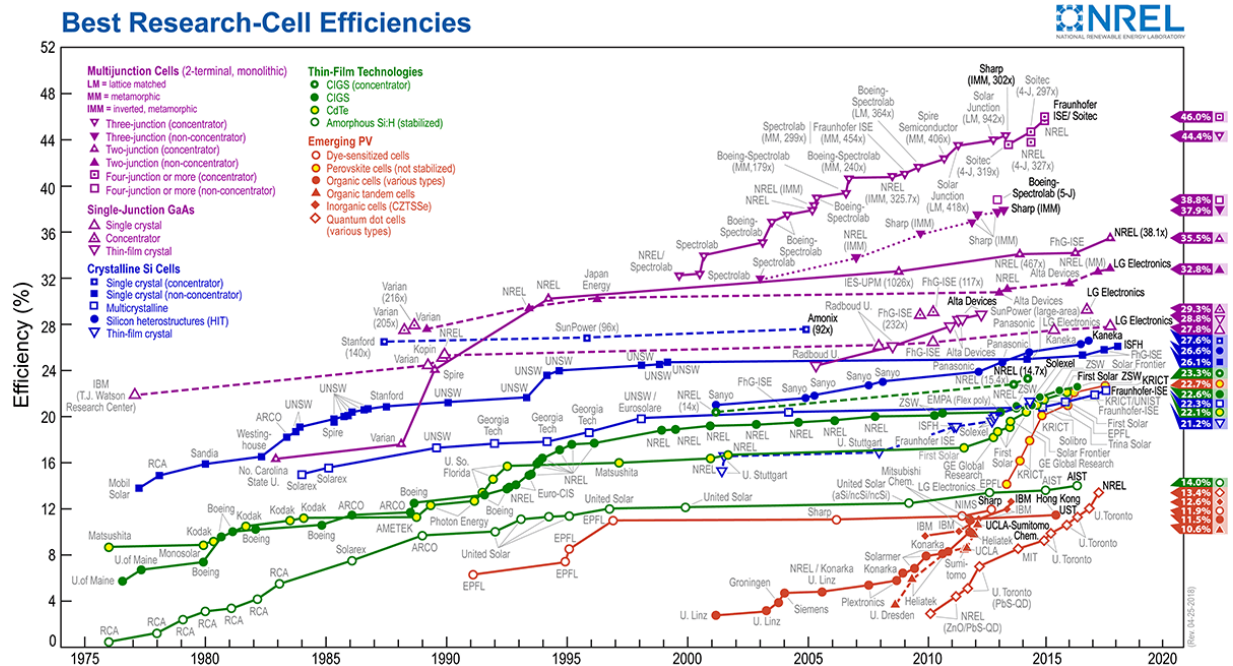
Figure 2.3. Best research cell efficiencies certified by National Renewable Energy laboratory. Copyright permission is provided in the appendix

2.5. Characterization of Image Sensors

Image sensors are members of optoelectronics family. Therefore, they share the same characterization methods with photodiodes (including solar cells), integrated optical circuit elements, photomultipliers etc. However, the figures of merit might be slightly different from one component to another. For example, open circuit voltage, short circuit current and fill factor in solar cells are the defining parameters as to whether the solar cell operates efficiently, and both its exterior and interior features are optimized or not. By contrast, dark current density and external quantum efficiency (EQE) is considered as the most important figures of merit for the image sensors. In this section, important parameters of the optoelectronic components used throughout this project and their measurement methods are described.

2.5.1. Short Circuit Current and Open Circuit Voltage

Short circuit current (I_{SC}) is the highest current level (short circuit condition) in an electrical system. Open circuit voltage (V_{OC}) is the voltage measured across the device (two terminal) when the device is disconnected. These two parameters are the focus of source optoelectronic components such as solar cells. An equivalent circuit model for a solar cell is shown in Figure 2.4(a). The ideal I-V characteristics of source optoelectronic components is given by

$$I = I_S \left(e^{qV/KT} - 1 \right) I_L \tag{1}$$

and

$$J_S = \frac{I_S}{A} = qN_C N_V \left(\frac{1}{N_A} \sqrt{\frac{D_n}{\tau_n}} + \frac{1}{N_D} \sqrt{\frac{D_P}{\tau_P}} \right) e^{E_g/KT} \tag{2}$$

where I_S is the diode saturation current, I_L is the source current built up due to the excitation of the excess charge carriers upon illumination, R_L is the load resistance (shown in Figure 2.4), A is the diode surface area, N_C is the effective density of states in the conduction band, N_V is the effective density of states in the valence band, D_n and D_p are the diffusivity for electron and hole respectively, τ_n and τ_p are the carrier lifetime for electrons and holes. E_g is the bandgap energy and K is the Boltzmann constant, T is the temperature and V is the voltage across the load. The current passing through the load equals $I = {-V}/{R}$. The current-voltage characteristics of a solar cell is shown in Figure 2.4(b). The point in which the produced current by the solar cell, equation (1), equals the load current with the same voltage is called the operating point. Adjusting the load value results in proper extraction of the power and higher efficiency solar cells. The blue

16

shaded rectangle shows the maximum power produced by the solar cell, $P = I_m \times V_m$, that can be produced by the diode.
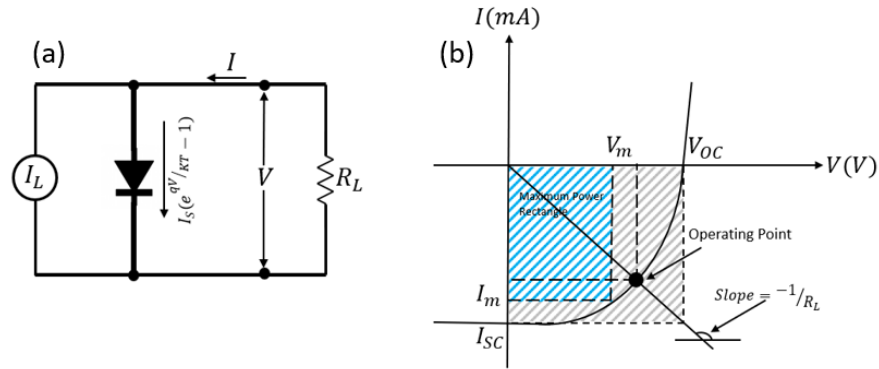
Figure 2.4. (a) Equivalent circuit model for a source optoelectronic component. (b) I-V characteristics of a light absorbing diode (solar cell)

2.5.2. Fill Factor

In imagers, the fill factor may be considered as the ratio of the active surface area to the total image pixel surface area of an image sensor. In solar cells fill factor is defined as the maximum power produced divided by the product of V_{OC} and I_{SC}[24, 37, 38]. In Figure 2.4(b), the ratio of the blue shaded area to the gray shaded area is defined as the fill factor and can be extracted from the I-V characteristics of a device.

2.5.3. Quantum Efficiency

In optoelectronics, quantum efficiency is defined as the rate of the incident photons to current efficiency (IPCE) or the conversion efficiency of photons to electrons. It may be considered as the percentage of the number of photons that produce charge carriers. Since each photon has a unique wavelength, quantum efficiency is a measure of the photoresponsivity of a device over a range of wavelengths. External Quantum Efficiency (EQE) is expressed as the ratio of the number of generated electrons to the number of incident photons, whereas Internal

17

Quantum Efficiency (IQE) is the ratio of the number of generated electrons to the absorbed photons.

$$\text{EQE} = \frac{\text{electrons/sec}}{\text{photons/sec}} = \frac{\text{current/(charge of one electron)}}{\text{(total power of photons)/(energy of one photon)}} \qquad (3)$$

$$\text{IQE} = \frac{\text{electrons/sec}}{\text{absorbed photons/sec}} = \frac{\text{EQE}}{1 - \text{Reflection}} \qquad (4)$$

2.5.4. Responsivity

Responsivity refers to the gain of an optoelectronic component. It is expressed as the ratio of the output current to the input light power in units of Amperes/Watt (A/W). Responsivity is an indicator of EQE considering the energy of each photon per charge of an electron.

$$R = \frac{J_{ph}}{L_{in}} = \frac{EQE \times e}{h\nu} \qquad (5)$$

where J_{ph} is the photocurrent density, L_{in} is the irradiance of the incident light, e is the electron charge, h is the Planck's constant and ν is the frequency of the incident photon.

2.5.5. Spectral Response (FWHM and λ_{max})

The absorption profile of an optoelectronic component over various regions of electromagnetic spectrum is a chief factor in determining their power conversion efficiency. The absorption of the photoactive layer in each component defines its application as a broadband or narrowband absorber. A Gaussian spectral response is expected from broadband silicon-based photodetectors. Due to their poor color discrimination, silicon-based photodetectors underperform in image sensing applications. A semi-Gaussian spectral response is preferred for imaging purposes as it sets the upper and lower limits closer to the maximum wavelength (λ_{max}).

Full width at Half Maximum (FWHM) for such applications should not exceed 200nm[39]. Such absorption profile results in precision color discrimination with minimum illuminant dependency.

2.5.6. Cross Talk Between Image Pixels

One of the main issues associated with the current technology of CCD and CMOS is the application of silicon in the structure of the pixels as photoactive materials and in the readout elements for microelectronic circuits as it puts a constraint on the size of the pixels [40]. The size of a pixel may vary from 10 microns to 1 micron[40]. The lower limit is determined based on an observation known as "Cross Talk". When the sizes of the image pixels are less than a micron, an undesired signal transfer occurs between the pixels. The root cause might be electrical as the effect of the leakage current in a pixel on its neighboring pixels, or optical due to light scattering and deflection[41, 42]. To reduce the cross talk, silicon may only be used for its electronics functions.

2.5.7. Dark and Noise Current

The current present in an optoelectronic component in the absence of illumination is called dark current. Dark current depends on the trap states, doping density, work function of the electrodes and charge carrier mobilities[43]. Each signal contains the dark current as well as the photocurrent. It is not practical to calculate the photocurrent accurately due to the random occurrence of shot noise and thermal fluctuations. Also, the frequency dependence of the noise level must be taken into consideration. As a result, the Noise current is defined to account these random fluctuations at a detection bandwidth of B:

$$i_{noise} = [i_{shot}^2 + i_{thermal}^2 + i_{1/f}^2 + i_{G_R}^2]^{1/2} = [2ei_dB + \frac{4kTB}{R_{sh}} + i(f,B)_{1/f}^2 + i(f,B)_{G-R}^2]^{1/2} \quad (6)$$

where k is the Boltzmann constant, T is the temperature in Kelvin, R_{sh} is the shunt resistance. The first two terms are independent of frequency and the third and fourth terms comprise the frequency dependence nature of noise.

2.5.8. Noise Equivalent Power (NEP) and Specific Detectivity (D)

The noise equivalent power is the measure of the sensitivity of an image pixel/photodiode when the signal to noise ratio is one over a bandwidth of one hertz with the unit of ($W/\sqrt{Hz}$) or ($V/\sqrt{Hz}$). The noise equivalent power can be calculated as follows:

$$NEP = \frac{i_{noise}}{R\sqrt{B}} \qquad (7)$$

The detectivity is defined as the reciprocal function of NEP and can be normalized to the square root of the surface are, A:

$$D^* = \frac{\sqrt{A}}{NEP} = \frac{R\sqrt{AB}}{i_{noise}} \longrightarrow D^* = \frac{e\lambda\sqrt{AB}.EQE}{hci_{noise}} \qquad (8)$$

specific detectivity is measured in units of $Hz^{1/2}W^{-1}$, common units known as Jones (J).

2.5.9. Dynamic Range

In optoelectronics, dynamic range refers to the ratio of the maximum to the minimum of an acquired quantity. In image sensors, the acquired quantity is the current. The minimum current level is the noise current. Since a linear response of an image sensor is required for imaging purposes, the concept of Linear Dynamic Range (LDR) is frequently used in this field. The response of an image sensor deviates from its linear format mainly due to the extension of space charges when the charge carrier concentration increases, resulting in a lower lifetime for the charge carriers with respect to their transit time[44]. Although the theoretical limit for the

20

minimum current is the measured noise level, it is known that the device response might become non-linear in lower light intensities as well[45]. The LDR is calculated using the following formula:

$$\text{LDR} = 20(10) \log \frac{I_{min}}{I_{max}} \qquad (9)$$

2.5.10. Speed of Response

In optoelectronics, the speed of response is considered as the time required for both generation and extraction of the charge carriers. In imaging applications, the speed of response might be high to enable capturing a wide range of varying levels of illumination in the environment. The operational bandwidth is defined as the frequency of the modulated input light at which the photoresponse in -3dB lower than continuous wave (CW) response. This bandwidth relies on the carrier transit time as well as the time constant of the device and is defined as follows

$$\frac{1}{f^2_{-3dB}} = \frac{1}{f_1^2} + \frac{1}{f_{RC}^2} \qquad (10)$$

where $f_t = \frac{1}{2\pi t_{transit}}$ and $f_{RC} = \frac{1}{2\pi RC}$

2.6. Photosensitive Perovskite Thin Films

Perovskite structures may be processed using methods listed below.

2.6.1. One Step Deposition

In this technique, the organic and inorganic salts are mixed in a solvent. The solution is deposited on the substrate using spin coating or dipping methods, shown in Figure 2.5(a)[46].

2.6.2. Sequential Deposition

The mixture of organic and inorganic salts in one solution reduces control over the morphology of the perovskite films. Hence, the reproducibility of the film becomes a subject of question. The sequential deposition technique is a two-step method in which the inorganic salt is first deposited and cured on the hotplate. The second step includes bringing the deposited film into contact with the organic salt dissolved in a solvent. This second step results in the nucleation of the perovskites and formation of thin films with higher reproducibility. However, one might consider the grain sizes in one step deposition more favorable, shown in Figure 2.5(b)[47, 48].

2.6.3. Solvent Engineering

Solution processable nature of the perovskite structures has boosted their popularity due to its cost-effectiveness and easy handling. In solvent engineering, the main solvent (e.g. dimethylformamide (DMF) or gamma- Butyrolactone(GBL)) is mixed with a solvent that has lower evaporation rate (e.g. dimethyl sulfoxide (DMSO)). This mixture retards the evaporation process to certain extend and gives the dissolved atoms enough time to position themselves properly in the perovskite framework while the materials are spun. Application (dripping) of a solvent such as toluene or chloroform that does not dissolve perovskite structures but is miscible with DMF, GBL and DMSO results in rapid intercalation of the solvent molecules inside the structure. Consequently, the interlayer expansion along the c axis occurs that results in more uniform structures and higher efficiencies[49].

2.6.4. Vapor-Assisted Deposition

In this method, the inorganic precursor spin-coated on the substrate is annealed in the vapor of the second precursor (organic) under N_2 flow to form the perovskite structure[50].

المنارة للاستشارات

www.manaraa.com

2.6.5. Additive-Assisted Deposition

In this deposition technique, a compatible chloride salt such as $PbCl_2$ is dissolved in 1,8-diiodooctane (DIO) and administered to provide homogenous nucleation and enhance the reproducibility of the film morphology[51].

2.6.6. Vacuum Evaporation

This process involves evaporation of organic and inorganic salt constituents of the perovskite structures under vacuum. Vacuum evaporation of the photoactive layers results in higher efficiency optoelectronic components, shown in Figure 2.5(c)[52].
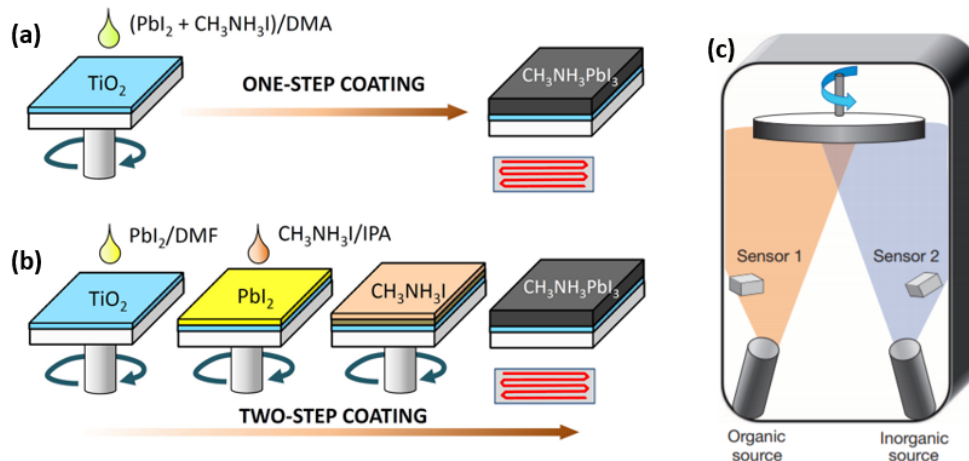
Figure 2.5. Perovskite thin films deposited using (a) one step deposition. (b) sequential deposition, reproduced from [48]under (CC BY 4.0) , figure provided under creative commons, (c) vacuum evaporation, copyright permission is provided in the appendix[52]

2.7. Charge Transport in Perovskite-Based Imagers

The photosensitive perovskite compound possesses dual ionic and electronic charge carriers[53, 54]. The presence of the ions is associated with the vacancy drift in the absorbing layers that influence the band structures under different biasing conditions, shown in Figure 2.6. This feature sets these photosensitive perovskites apart from other direct bandgap inorganic semiconductors. The charge transport mechanism of the perovskites cannot be modeled using

the well-known 1D drift-diffusion process. In fact, the study of the charge carrier transport

properties of the photosensitive perovskite compounds is extremely difficult due to the

variations in the fabrication process and crystalline structures. The charge transport properties

alter depending on the degree of crystallinity and crystal orientation of the perovskite[55, 56].

For example, the diffusion length of the charge carriers in single crystalline structures is three

orders of magnitude greater in single crystalline structures compared to the polycrystalline

ones[57].
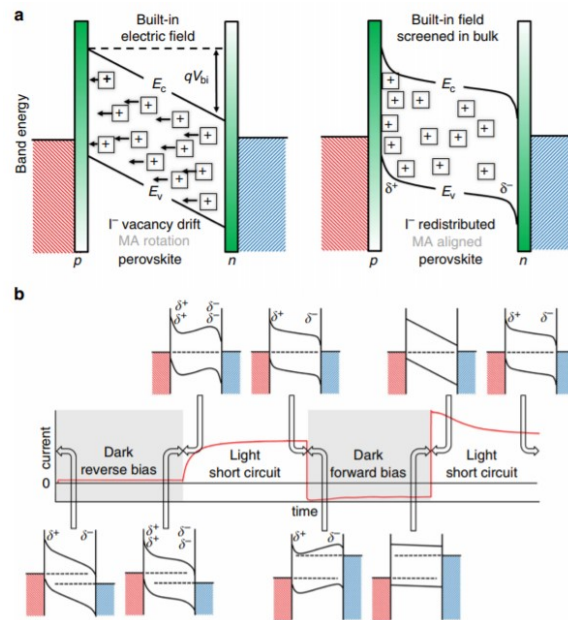
Figure 2.6. The ionic transport causes vacancy drift in the perovskite-based p-i-n device configuration which changes the band structure under different biasing conditions. (a) E_c is the conduction band, E_v is the valence band, the iodide vacancies are shown as squares carrying positive charges and V_{bi} is the built-in voltage. (b)Schematic of energy level variations during chronophotoamperometry measurements. The variations in the band structures stem from the redistribution of the iodide vacancies and interface changes under different biasing conditions, reproduced from[58] under (CC BY 4.0) .

In the energy conversion process, an absorbed photon stimulates an exciton (bound

electron and its hole). Various binding energies result in different dielectric constants in the

perovskites. For instance, the static dielectric constant for a single crystalline methylammonium

lead triiodide is $\varepsilon_0 = 25.7$ where its high frequency dielectric constant is $\varepsilon_\infty = 5.6$[59]. These values with a small tolerance are repeatable in other types of the perovskites indicating the presence of an extremely weak screening of Coulomb force in the electron-hole pair. This fact demonstrates the high possibility of charge carrier generation and extraction in these compounds. However, the presence of the trap states reduces the mobility and diffusion length values in these structures resulting in lower values of external quantum efficiency. The effect of deep or shallow defects may not be overlooked in modeling the charge carrier related parameters[60]. A schematic of the photophysical processes after photoexcitation and the loss mechanism in the perovskite structure is shown in Figure 2.7.
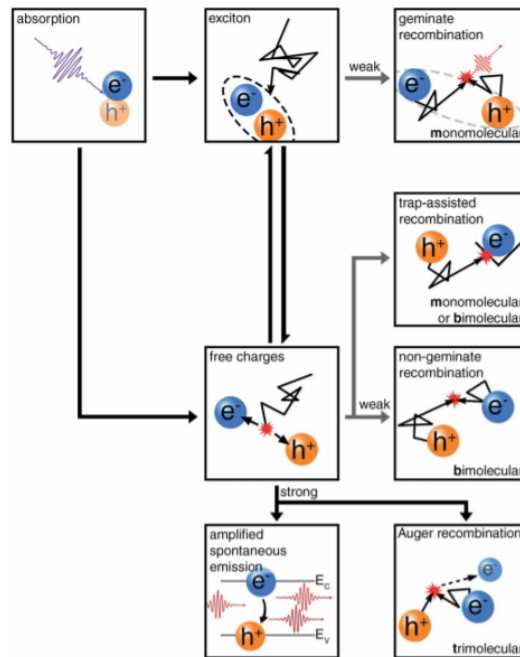
Figure 2.7. Photoexcitation results in the creation of an exciton. Due to the high dielectric constant of the perovskites, the exciton dissociates easily for charge carrier collection. The possibility of charge carrier recombination is shown in black (strong possibility) and gray (weak possibility) are shown in the schematic. Monomolecular recombination is independent of charge carrier density whereas bimolecular and Auger recombination depend on the charge carrier density. The latter surfaces under high-intensity photoexcitation. Typically, under high intensity, Auger recombination is overshadowed by spontaneous emission, reproduced from [61] under (CC BY 3.0.)

There have been several first principle studies on mobility measurements and minority carrier lifetimes. Also, experimental methods such as electrical transient technique (e.g. time of flight, CELIV), steady state technique (e.g. Hall effect and space charge limited current), time-resolved laser spectroscopy (e.g. time-resolved photoluminescence, transient absorption) have been utilized to measure the charge carrier mobilities and diffusion lengths[62]. In this regard, different measurement techniques result in different values of the inquired parameters. Charge carrier mobilities within 1-100 $cm^2V^{-1}S^{-1}$ and diffusion lengths greater than 1 micron are reported for different structures[63, 64].

2.8. Organometal Trihalide Perovskite Image Sensors

2.8.1. Vertical Structure Image Sensors

A planar heterojunction configuration consisting of an anode, a hole transporting layer, perovskite-based active layer, an ectron transporting layer, and cathode has been adopted for photodetection application due to its favorable response time and low external biasing requirement[65]. This planar configuration may establish a regular (p-i-n) or an inverted (n-i-p) structure for photodetection purposes, shown in Figure 2.8.
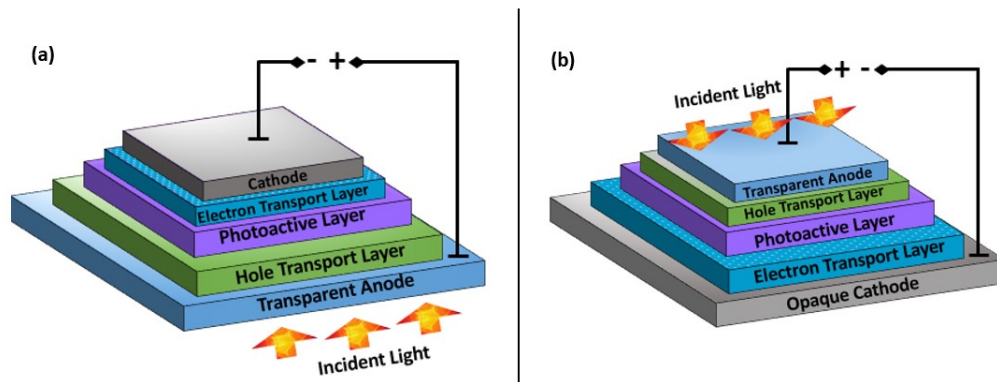
Figure 2.8. (a) Regular p-i-n configuration. (b) Inverted n-i-p configuration

26

2.8.1.1. Regular p-i-n Configuration

This configuration consists of a conducting transparent anode coated with a highly doped p-type semiconductor, a photosensitive perovskite and highly doped n-type semiconductor followed by a high work function metal contact. This configuration has been realized using a variety of soft semiconductors to sandwich the perovskite content of the active layer. The stack of the materials must be encapsulated to avoid deterioration of the perovskite structure and possibly the n-type semiconductor over time.

2.8.1.2. Inverted n-i-p Configuration

The bottom layer in this configuration is the metal contact basing a stack of a highly doped n-type semiconductor, a photosensitive perovskite layer and a highly doped p-type layer. A transparent top contact is required for charge collection purposes. The stack must be encapsulated to prevent deterioration of the sensitive materials over time. This configuration is particularly desired for integrated silicon-perovskite image sensors. The electronics of the system can be provided using the base silicon and the fill factor of the image sensor can be enhanced using the inverted perovskite pixel.

2.8.2. Lateral Structure Photodetectors

Photoconductors and phototransistors possess lateral structure configuration. Photoconductors detect the signal and produce electrical output due to the work function difference on their front and rear electrical contacts. Phototransistors detect the signals and amplifies it simultaneously. Therefore, their configuration is of great importance for image sensing applications.

2.8.2.1. Image Sensors Based on Large Size Single Crystal Perovskites

These pixels include a large size single crystal photosensitive perovskite with different front and rear contacts. Different contact materials result in a gradient in their work function. Therefore, generated charge carriers are forced to leave the crystal under reverse bias condition. According to Dong et al., the diffusion length in these single crystals might be up to 3 mm[57]. A UV photodetector fabricated on a single crystal perovskite (synthesized using inverse thermal crystallization technique) with $Au/Ti/CH_3NH_3PbCl_3/Pt$ configuration demonstrated a responsivity of 46.9 mAW^{-1} and a detectivity of 1.2×10^{10} Jones[66]. These values have proven that perovskite-based image sensors outperform conventional image sensors even in their product development stage.

2.8.2.2. One Dimensional Perovskite Image Sensors

Perovskite structure in the form of nanowires have been used in photodetection applications. The large surface to volume ratio of these structures in low dimensional image sensors resulted in a response time of ~ 0.3 ms , a detectivity of 2.5×10^{12} Jones and a responsivity as high as 1.3 AW^{-1}[67].

2.8.2.3. Two-Dimensional Perovskite Image Sensors

Optimized thicknesses of the photosensitive perovskite compounds may be employed as a channel layer in phototransistors. These structures function like two-dimensional graphene layers with superior characteristics such as light absorption bandwidth tunability, shorter response time and simple deposition methods[68].

28

2.8.2.4. Perovskite-Based Heterostructure Image Sensors

Perovskite materials can be easily hybridized with another conductor (e.g. graphene) or semiconductor (e.g. PEDOT:PSS, ZnO) materials to form a heterostructure with modified characteristics. Utilization of the hybridized materials in the configuration of an image sensor may feature desired properties such as faster response time or wider absorption range[69, 70].

2.9. Photomultiplication in Perovskite Image Sensors

The unique properties of the light absorbing perovskites might result in photomultiplication. This effect may be attributed to trap assisted charge tunneling mechanism, interface modification mechanism or ferroelectric polarization mechanism. A brief description of each of these mechanisms is listed below.

2.9.1. Trap Assisted Charge Tunneling

Defect engineering is one of the many approaches to enhance the charge carrier transportation. Trap states may function favorably if designed to serve for trapped-hole-induced electron injection[71]. Dong et al. described that the presence of trap states near the surface might result in electron injection which enhances the gain of the device under reverse bias condition[45, 71, 72].

2.9.2. Interface Barrier Modification

Several studies have indicated that the quality of the electron or hole transport layer influences the current level upon illumination[73, 74]. The compactness and thickness of these semiconducting materials must be engineered to provide a defect-free interface.

2.9.3. Ferroelectric Polarization Mechanism

Light absorbing perovskite structures have shown ferroelectric behavior in their I-V characteristics[75]. In image sensors, under reverse bias condition, the polar domains may induce charge carrier separation and reduce the recombination rate resulting in higher gain[76, 77].

2.10. Open Issues on Perovskite-Based Optoelectronic Devices

Research and development on perovskite-based optoelectronic devices have not been able to resolve some of the fundamental issues regarding the device level performance of the light absorbing perovskites. These issues are listed below.

2.10.1. Stability

Despite the outstanding properties of the light absorbing perovskites, the long-term stability of its thin films has hindered their commercialization and requires practical resolutions. The studies have shown the adverse effect of humidity, temperature, oxygen and UV light on the performance of perovskite-based optoelectronic components[78]. The device configuration and interface engineering are crucial parameters in reducing the degradation rate. For example, the presence of the mesoporous metal oxide structures alleviates the adverse effect of moisture and oxygen in the device[79]. Encapsulation of the devices may also protect the perovskite structure from exposure to the ambient[80]. In order to commercialize the highly efficient perovskite-based optoelectronic devices, long-term resolutions are required. Therefore, further research in this area is highly demanded.

2.10.2. Ion Migration

In perovskite compounds, the ion migration results in displacement of vacancies. The ion migration may be stimulated by thermal energy or local polarization in a fast (migration of iodide

vacancies/interstitials) or slow (migration of ions to build shallow states and distort the crystalline structure) mode[81]. The grain boundary passivation seems to help with the fast mode migration but the issue of the slow mode migration has not been resolved and requires further investigation[82].

2.11. Conclusions and Future Outlook

The light absorbing perovskite structures have been employed in various configurations to overcome the limitations of the current technology in optoelectronics industry. Lightweight, flexibility, low cost and light absorption bandwidth tunability of this new generation of optoelectronic components are revolutionary. Commercialization of these components would realize a highly complex set of possibilities and advance the new technologies such as machine vision, intelligent transport systems, flexible medical imaging and internet of things. Tailoring the bandwidth of the perovskites using different ratios of the halides or narrowband absorbers in their structures, using additional layers in the stack of materials to absorb undesired wavelengths have been implemented.

However, a deeper understanding of the charge carrier mechanism in perovskite structures blended with different absorbers is required for mass production of perovskite-based optoelectronic components. Interface engineering is another consideration that should be taken into account for the further development of this technology. Finally, instability of the perovskite compounds must be addressed properly as a major obstacle on the way of commercialization of these devices.

CHAPTER 3 : EXPERIMENTAL AND CHARACTERIZATION METHODS

This chapter provides a detailed description of the new generation of optoelectronic devices that were explored in this document. The expected performance characteristics of these devices, as well as the characterization techniques, are discussed.

3.1. New Generation of Optoelectronic Devices

A new generation of optoelectronic devices reflect the technology of the conventional ones and take it a step further where the flexibility and facile manufacturing come to play due to the utilization of new materials. The basic configuration of every optoelectronic device includes a photoactive layer, with a metallurgical junction to enable charge carrier extraction with two ohmic contacts on their anode and cathode electrodes. The following is a description of each optoelectronic device covered as part of the pilot test in this project to better understand the fundamentals of photodiodes and consequently image sensors.

3.1.1. Photoelectrolytic Cells

Dye-sensitized solar cells (DSSC)s emerged in late ninetieth developing a new understanding with respect to the functional materials. Up until the invention of the DSSCs, the semiconductor industry required labor intense, costly processing steps to dope a semiconductor and enhance its responsivity to optical or electrical signals. In DSSCs, metal oxides were deposited using sputtering, spin coating, spraying, doctor blading or ink jet printing methods. They were then doped through dipping them inside a solution containing organic or inorganic pigments. The

structure of DSSCs was almost identical to supercapacitors. The only difference was the employment of a photoanode instead of an anode as the working electrode. A basic configuration of a dye-sensitized solar cell and a supercapacitor, two electrochemical cells, are shown in Figure 3.1(a) and 3.1(b), respectively.

A DSSC consists of a working electrode, an electrolyte, and a counter electrode. The electrolyte must contain a redox couple. The energy harvesting process begins when the electron in a dye molecule is promoted to the excited level from the ground state through absorption of a photon. The photogenerated electron then transfers to the semiconductor conduction band and diffuses toward the back contact. The oxidized dye molecule is then reduced through oxidizing the redox mediator and regenerates its ground state. The redox couple are being oxidized in the working electrode and reduced in the counter electrode. This process continues as long as the cell receives photons to generate electric charges.

A supercapacitor, on the other hand, consists of two porous electrodes with an electrolyte. Supercapacitors are often categorized based on their charge storage mechanism or the materials of their electrodes. Porous materials such as carbon, store charges electrostatically and feature the device as an electrochemical double layer capacitor. Transition metals or conducting polymers store charges electrochemically in their structure in response to fast surface and near-surface redox reactions and feature the device as a pseudocapacitor.

Despite the rather slow development of DSSCs, their inexpensive manufacturing process has motivated many researchers. The understanding of the operational principles in DSSCs later led to an outstanding achievement in the field of optoelectronics.
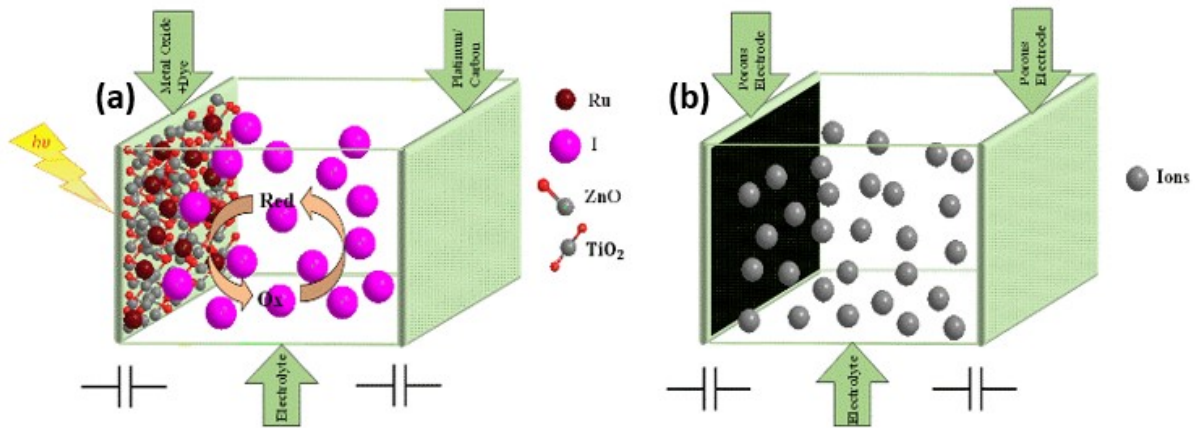
Figure 3.1. (a) A dye-sensitized solar cell, each electrode could be represented by a capacitor. (b) A supercapacitor consists of two electrodes with a double layer or pseudocapacitive behavior.

As shown in Figure 3.1(a), a DSSC device (with dye or perovskite as a sensitizer) is based on three different compartments. The first compartment includes the photo-active electrode with an electron extraction capability. The electrode has dye molecules or perovskite micro crystals as sensitizers placed on a metal oxide (MO) scaffold. The captured photons by sensitizers generate electron-hole pairs. The electrons would be extracted by the metal oxide layer. The considerations in this part of the cell would be the energy mismatches between the sensitizer and the conduction band of the MO. In a conventional DSSC, the best combination was known to be titanium oxide, TiO_2, as the metal oxide with 3.2eV bandgap energy and, N749, black dye. The synthetic dyes have been designed for various band structures and those compatible with titanium oxide are mostly ruthenium-based dyes with slightly different bandgaps from 2.1 eV above.

The second compartment is the ion transportation medium. In contrast to other electrochemical cells such as supercapacitors, DSSCs' charge transportation is accomplished using redox couples. The redox couples with high mobility, compatible electrochemical potential, and high kinetic rate are desired to achieve high photocurrent and high efficiency in a DSSC. A

34

typical electrolyte contains a redox couple dissolved in an organic solvent such as iodide triiodide dissolved in acetonitrile. The third compartment is the counter electrode. Platinum or carbon-based electrodes are mostly used for the counter electrode. The operational mechanism of DSSCs and the charge transfer direction at each interface along with carrier lifetime is shown in Figure 3.2.
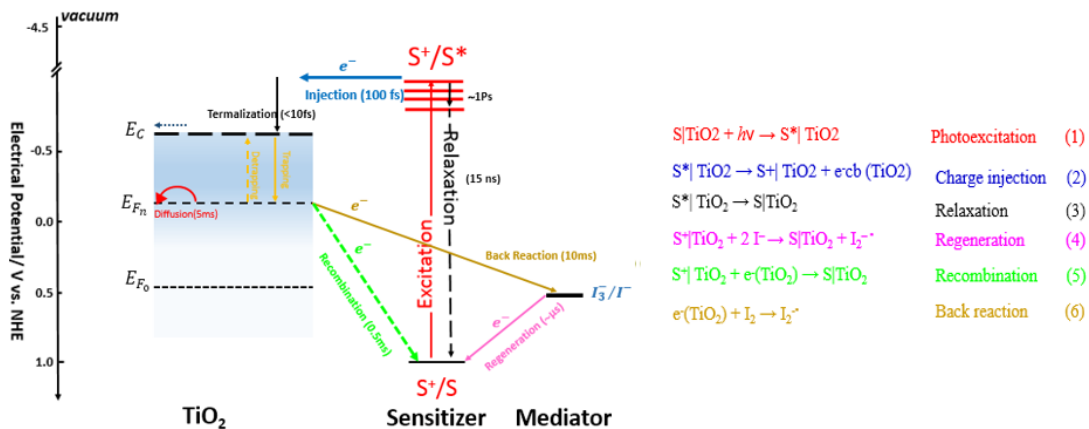
Figure 3.2. Operational mechanism of a Dye-Sensitized Solar Cell and the equations in each interface

One of the highest efficiency reported for a DSSC is 11.9%[83]. In order to enhance the efficiency of this generation of solar cells, the semiconductor in use must be transparent and the redox couples must display minimum photosensitivity. Also, the synthetic dyes must possess proper work functions with respect to the metal oxide to reduce the loss in the dye-metal oxide interface. These synthetic dyes are fairly versatile; however, their low absorption coefficient and narrow absorption bands are limiting factors in a DSSC to reach higher efficiencies. Yet, substitution of the dye molecules with perovskite material overcome this issue. Kojima et al. reported the first DSSC with an organometal halide perovskites in 2008 [5].

3.1.2. Photoelectrolytic Cells Layout

The photoelectrolytic cells were realized in a cuvette with the working electrode connected to the negative terminal and the counter electrode connected to the positive terminal of a potentiostat. The cells were then placed in a dark box in direct exposure to 1 sun. The equivalent circuit models for the photoelectrolytic cells are shown in Figure 3.3.
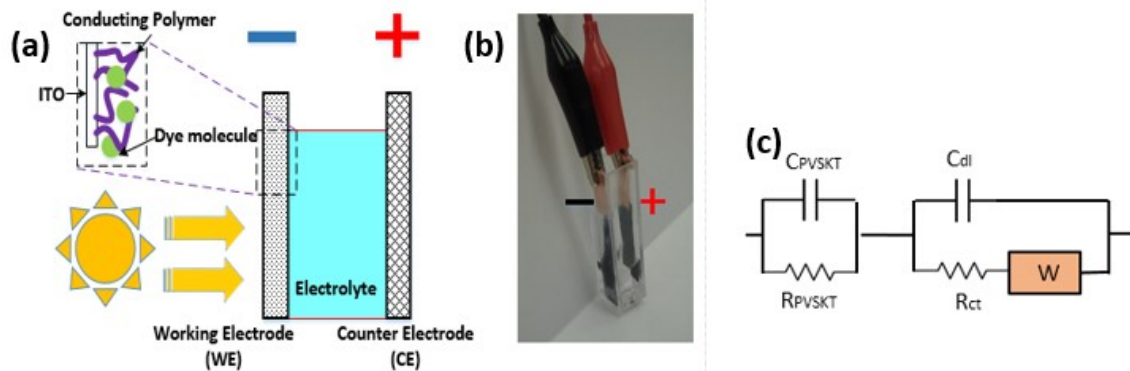
Figure 3.3. (a) Schematic of a DSSC with a hybrid working electrode. (b) device configuration under test, (c) equivalent circuit model for a DSSC[84]

3.1.3. Photodetectors

Semiconductor industry seeks alternatives to the current state of the art technology of CCD and CMOS devices. Organic contents have been proven to be the most practical substitutes or complements to the current practice. The intriguing characteristics of organic electronics may bring a wide range of applications to existence that currently seems beyond the realms of possibility. As stated earlier, a slab of semiconductor with two ohmic contacts on its front and rear ends construct a photoconductor[24]. In order to conduct photogenerated electrons and holes in a specific direction, a p-n junction must be present (solar cells as an energy source). A reversed biased p-n junction is required to read the energy of the photons (photodetectors). The charge transport mechanism in organic materials varies fundamentally from inorganic ones. Therefore, the exciton binding dissociation must take place using several layers of materials with

المنارة للاستشارات
www.manaraa.com

varying HOMO and LUMO levels. A stack of materials must be built up in the architecture of the new generation of the photodetectors to enhance their responsivity.

The most common built-up architecture starts with a high work function transparent substrate. This first layer can be a highly doped transparent metal oxide such as indium doped tin oxide coated on a glass substrate. A hole transporting material such as poly(3,4-ethylenedioxythiophene) polystyrene sulfonate or PEDOT:PSS forms the second layer. A photoactive layer consisting of perovskite compounds and synthetic dyes is sandwiched between the hold transporting layer (second layer) and an electron transporting layer, low work function cathode, such as [6,6]-Phenyl C71 butyric acid methyl ester or PCBM. Another stacking concept concerning inverted photovoltaics may be realized by exchanging the functionality of the electrodes and building up the structure on an opaque substrate such as silicon. The desired vertical phase segregation in this modified concept results in improved carrier collection[85]. The last step in the fabrication of each photodetector must be the encapsulation process regardless of the stacking concept in use[86]. The architecture of two stacking concepts are shown in Figure 3.4.
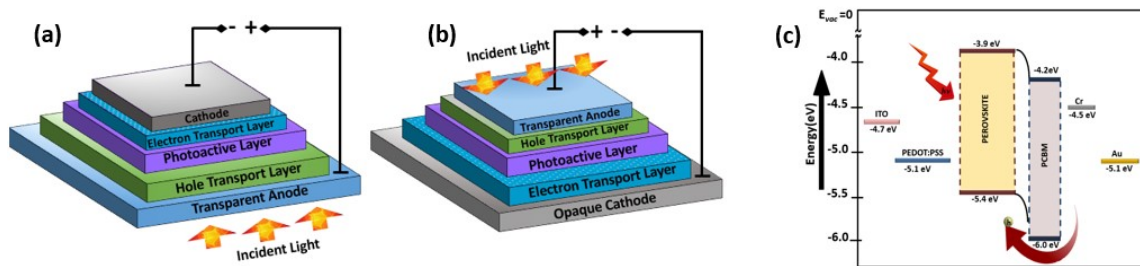
Figure 3.4. (a) Regular p-i-n photodiode, (b) inverted n-i-p photodiode, (c) band structure of the stacked materials

3.1.4. Photodiode Layout

The stack of materials sandwiched between the anode and cathode define the active area. An active layer in a homojunction photodetector structure is divided into three different regions. The first region has the highest absorption coefficient α and is close to the surface. The governing equation in this region is Beer-Lambert law. Carriers generated in this region most likely recombine before collection. This region is termed as Beer-Lambert region. Depending on the thickness of the active layer, the second region with low absorption coefficient α experiences cavity effect. In the cavity region, there exist a volume generation of carriers that are most likely collected. The collection of carriers in the cavity region contributes the most to external quantum efficiency of the device. The FWHM in the response of the device can be manipulated by changing the onsets defining the cavity region.

Tuning the ratios of the halide constituents of the perovskite provide the lower limit (short wavelength) in the cavity region of the homojunction. However, the design of a narrowband photodetector requires another absorbent to set the upper limit (longer wavelength). The third region, in the active layer, has no absorption and does not contribute to the charge collection. Figure 3.5(a) shows a schematic of the absorption coefficient versus wavelength across the width of the active region. A great deal of care must be taken in the selection of the absorbent molecules; proper energy level alignment is required to prevent a reduction in charge transfer rate and photoresponsivity. A profound understanding of the role of absorbent molecules progresses the current imaging systems towards more advanced and low-cost productions; developing higher pixel densities, acutance and color constancy. In this work, the bandwidth of the photodetector is tuned/optimized using various ratios of lead salts

38

and a particular synthetic absorbent (to IR-blind the device). To develop a versatile recipe for selective sensing on the spectrum, the effect of the molecular structure of the absorbents is placed under scrutiny. Figure 3.5(b) shows the architecture of the photodetector fabricated in this work.
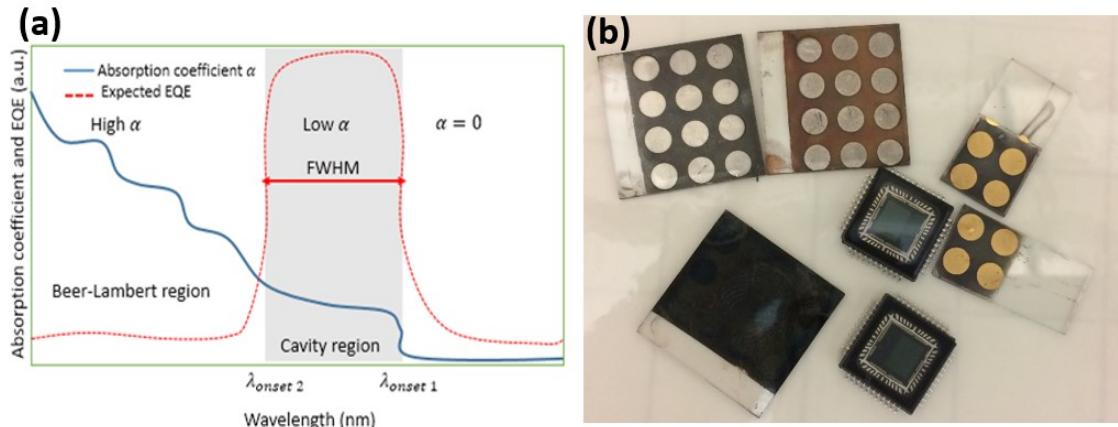
Figure 3.5. (a) Light absorption and expected quantum efficiency versus wavelength for narrowband image sensors. (b) fabricated image sensors in the lab with various ratios of halides and macromolecules (two commercial image sensors are included in the image for reference)

3.2. Materials for Perovskite-Based Photodetectors

This section includes the materials used in the fabrication of the optoelectronic components used in this dissertation.

3.2.1. Metal Oxides

3.2.1.1. Zinc Oxide

Zinc oxide is a transparent, wide bandgap semiconductor (Eg~3.3eV) with high electron mobility[87]. This inorganic compound possesses piezoelectric characteristics and its nanostructures are widely used in the fabrication of DSSCs and field emission devices[88]. In this project, the conventional hydrothermal method was used to synthesize zinc oxide nanowires for DSSCs. A seeding solution of 10 mM of zinc acetate in ethanol was spin coated on the active area

39

www.manaraa.com

of Fluorine-doped Tin Oxide (FTO) coated glass substrate at 1500 rpm for 45 s. The sample was then annealed at 150 °C on a hot plate for 2 min. The seeding deposition process was repeated 10 times. The prepared substrate was placed face down in a bath of growth solution containing 25 mM of each, zinc nitrate hexahydrate, and hexamethylenetetramine, in DI water for 2 h. The growth bath setup had a constant temperature at 90 °C and the growth solution was stirred at 250 rpm. After the growth, the active area was rinsed with DI water and ethanol. A scanning electron microscopy image of the zinc oxide nanowires is shown in Figure 3.6.
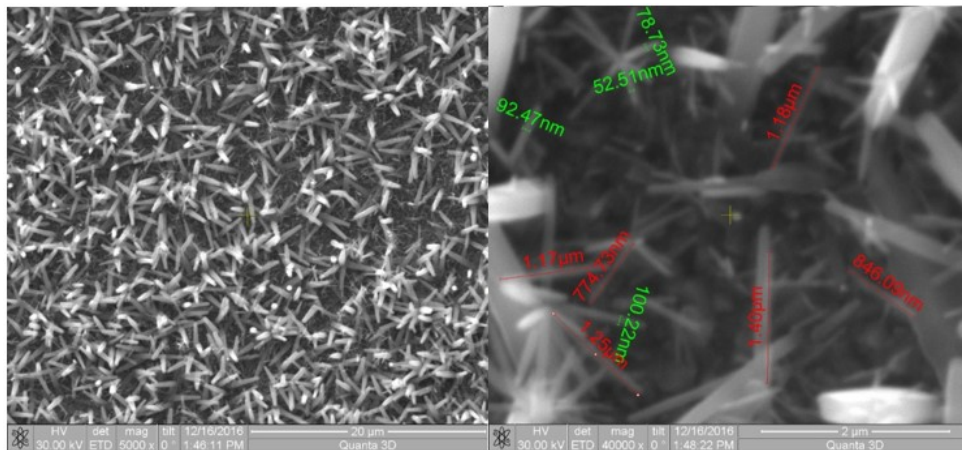
Figure 3.6. Scanning electron microscopy image of ZnO nanostructures

3.2.1.2. Titanium Dioxide

Titanium dioxide (TiO_2) is a wide bandgap semiconductor ($E_g \sim 3.05 eV$ in rutile structure). Its nanostructures possess a transparent color and a mesoporous texture which makes them suitable candidates as scaffolds in DSSCs[89]. In this work, a thin film of TiO_2 was doctor-bladed on an FTO substrate and sintered up to 500°C with a rate of 5°/min. The substrate was kept at 500°C for 30 minutes. The temperature was then ramped down to 80°C with a rate of 5°/min. The sintered TiO_2 substrates were then treated with 55 mM $TiCl_4$ at 90°C for 30 min and rinsed with DI water and ethanol.

40

3.2.1.3. Tin Dioxide

Tin dioxide (SnO_2) is a wide bandgap semiconductor ($E_g \sim 3.6eV$ in rutile structure). Its suitable work function, transparent color, and simple deposition methods are the driving forces behind the further development of this compound in the field of photovoltaics. In this work, two different deposition methods were employed to form a layer of SnO_2 with a thickness of 100nm. The first method is based on the spin coating of a solution containing 0.05M of $SnCl_4$ 5H2O (stirred for 30min at room temperature) on an ITO coated substrate at 3000rpm for 30s with a 200rpm/s ramp down to zero. The spinning was then followed by pre-drying at 100°C for 10 minutes and heat treatment at 180°C for an hour[46]. The second method includes using an SnO_2 sputtering target to sputter. An SEM image of SnO_2 coated ITO glass substrates is shown in Figure 3.7.
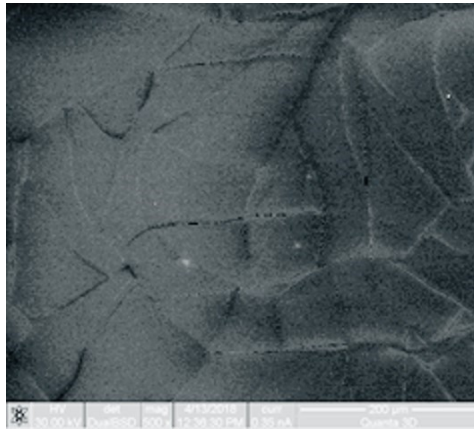
Figure 3.7. Scanning electron microscopy image of SnO_2 coated ITO glass substrates

3.2.2. Conductive Polymers

Polymers in nature present high resistivity to electrical conductivity unless they possess unsaturated double bond(s) in their structures. Depending on the number of charge carriers, due to the presence of the double bonds, and their configurations, these compounds might function similar to semiconductors or even conductors. The main advantage of these compounds is their

41

processability through dispersion. Some of these compounds display several oxidation states which makes them suitable candidates for energy harvesting and storage purposes, e.g. MEMS devices and supercapacitors[90]. Different doping levels result in a wide range of electrical conductivity in these compounds while maintaining their flexibility and thermal stability. Conducting polymers are one of the building blocks of the new generation of photovoltaics. The conducting compounds used in this project are described in the following sections.

3.2.2.1. Polyaniline

Polyaniline (PANI) is a conducting polymer with two distinct structures: Pernigraniline (PNB) and Leucoemeraldine (LEU). In the PNB form, the doped polymer has a conjugated structure along the molecule. Therefore, the polymer is a good conductor in this state. In presence of an acid, the polymer can be reduced to the LEU form. The absence of the conjugated structure in LEU makes the polymer to be more insulating[84]. Due to the long structure of a polymer, many protons (H^+) and electrons (e^-) are required for converting a PNB molecule to a LEU one. Hence it is possible to partially reduce a PNB. The oxidation state in which PANI is partially reduced is called Emeraldine (EB). The conductivity of the polymer in EM mode is higher than that in the LEU mode but it is less than PNB mode.

The ability to load the polymer with many electrons in the transition process from PNB to LEU makes PANI a good candidate for supercapacitors[91, 92]. This mechanism of charge storage in a supercapacitor with the change in the oxidation state of the polymer is known as a pseudo-capacitive effect. Since the polymer is stable in all the oxidation states (shown in Figure 3.8), the stored charges are more stable than the stored charge in a double layer capacitor. Besides, the

low conductivity of the polymer in its reduced state is expected to present lower leakage current and longer charge storage time in the devised photovoltaic device.
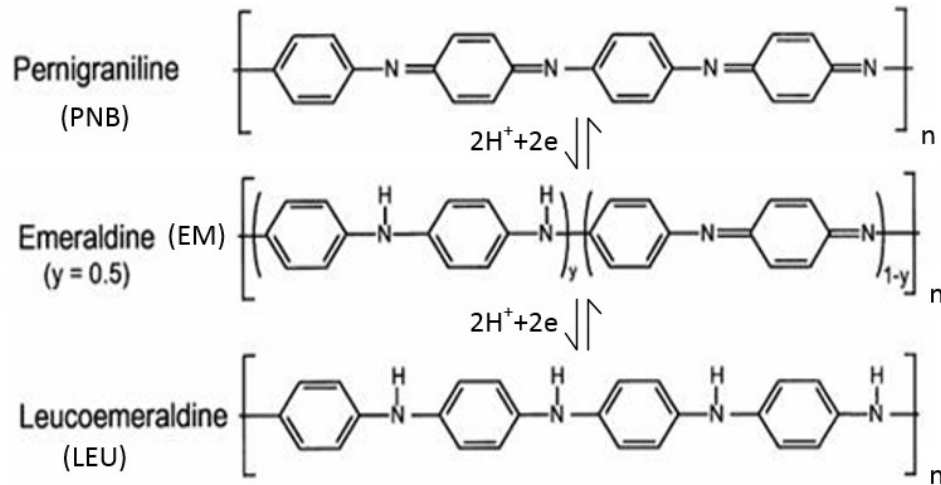
Figure 3.8. Polyaniline structure in its different oxidation states. The copyright permission in included in the appendix[93]

3.2.2.2. Poly(3,4-EthyleneDiOxyThiophene) PolyStyrene Sulfonate (PEDOT:PSS)

Poly(3,4-ethylenedioxythiophene) polystyrene sulfonate known as PEDOT:PSS consists of two ionomers. The polystyrene sulfonate or PSS carries negative charges and the poly(3,4-ethylenedioxythiophene) or PEDOT carries positive charges. Its conductivity can be enhanced by doping the compound using ethylene glycol, dimethyl sulfoxide (DMSO) or other chemicals with similar formulae[94, 95]. It has been proven that doping of this compound results in the removal of more electrons from the PEDOT π-conjugated orbitals[96]. The transparent color of this organic semiconductor along with its superior ductility make them indispensable parts in fabrication of the flexible organic electronics[97]. Figure 3.9 shows the molecular structure of this compound and its HOMO and LUMO levels[98].
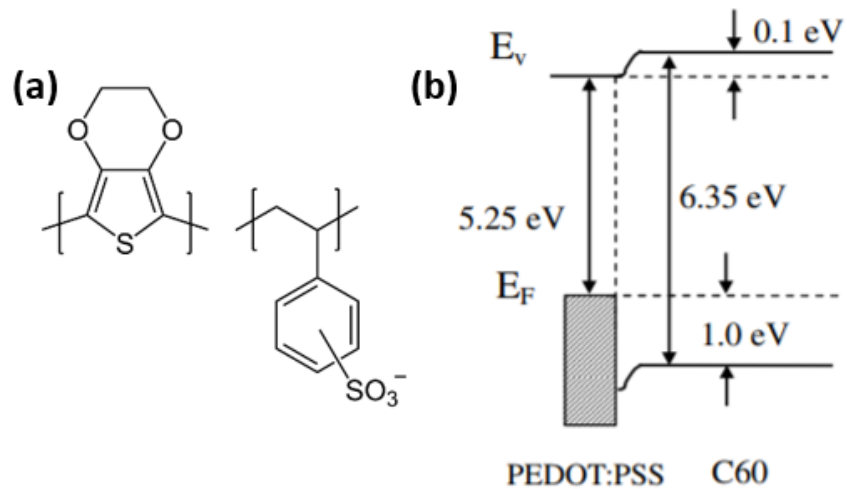
Figure 3.9. (a) Molecular structure of PEDOT:PSS, (b) Energy band structure of PEDOT in contact with C60. The copyright permission is included in the appendix[98]

3.2.2.3. [6,6]-Phenyl C71 Butyric Acid Methyl Ester (PCBM)

PCBM is a common fullerene derivative functionalized to accept electrons[99]. Structures of PCBM have shown high stability, an electron mobility of 10^{-1} and hole mobility of 10^{-5} -10^{-4} cm^2/Vs[100]. This compound is widely used in solution processable architectures as an n-type semiconductor[101]. The orbital energy HOMO for this material is 6eV and the LUMO level is 3.9eV. The molecular structure of this compound is shown in Figure 3.10.
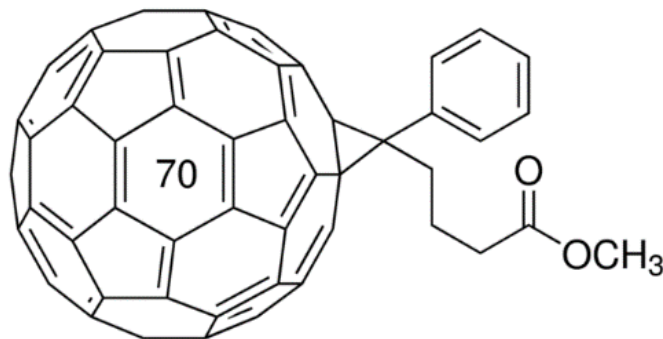
Figure 3.10. Molecular structure of PCBM

3.2.3. Macromolecules

3.2.3.1. Methylene Blue

Methylene blue is considered as a chloride salt. It is soluble in water and organic solvents. It forms dimers in concentrations below 0.01M and might aggregate in higher concentrations[102]. Methylene blue displays a two-electron reduction. Its reduced form is called leuco and appears as a colorless strong base that becomes heavily colored upon re-oxidation, the reaction is reversible[103]. The absorption spectrum of this dye is shown in Figure 3.11. The absorption varies based on the concentration and the probability of the presence of the dimers.
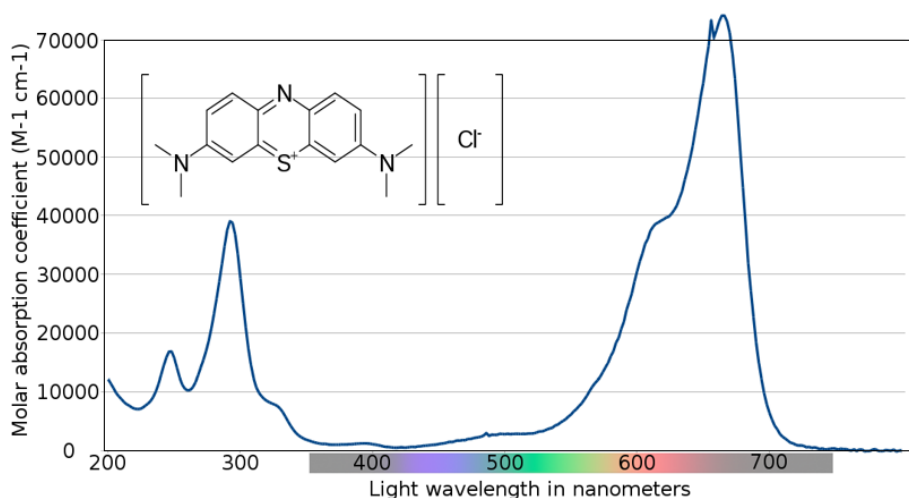
Figure 3.11. Absorption spectrum of methylene blue. The inset is a 2D-structure of dichloropane methylene blue. Reproduced under (CC BY-SA 3.0)

3.2.3.2. Rhodamine B

The photophysical properties of Rhodamine B such as long absorption and emission wavelengths, large extinction coefficient, stability and high fluorescent quantum yield makes this compound an interesting choice in organic thin film manufacturing[104]. The absorption spectrum of this compound surfaces between 500-650nm with a low energy peak at 2.22eV and

www.manaraa.com

a high energy shoulder at 2.38eV. The peak is attributed to the first $\pi - \pi$ transition and displays the characteristics of an excitation peak[105]. Figure 3.12 shows the molecular structure of this compound and its absorption spectrum.
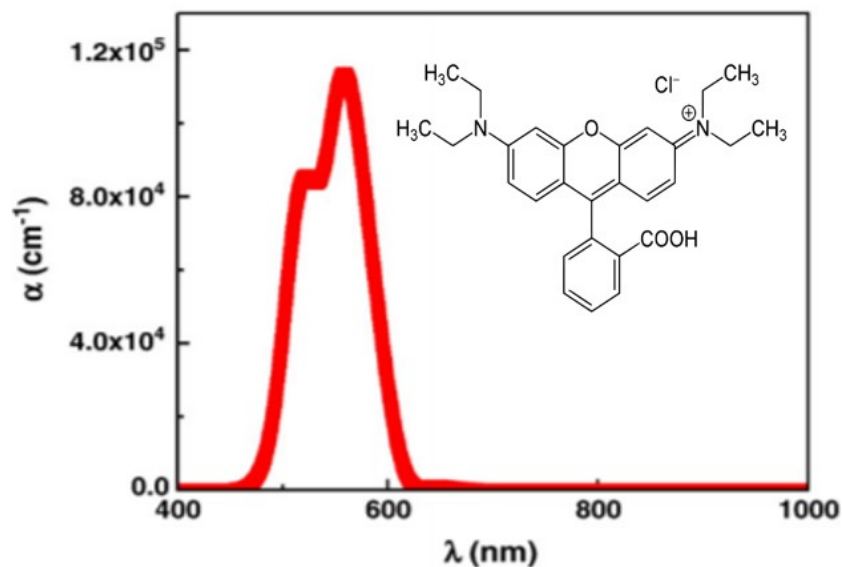
Figure 3.12. Absorption spectrum of rhodamine B. The inset shows the molecule structure of rhodamine B. The copyright permission is included in the appendix[104]

3.2.3.3. Polyethylenimine Etoxylated (PEIE)

Polyethylenimine ethoxylated (PEIE) and branched polyethyleneimine (PEI) are polymers with repeating units of the amine group and two carbon aliphatic CH_2CH_2 spacer. Hight contents of amine group (primary, secondary and ternary) alter the PH level in aqueous and methoxyethanol solutions resulting in lowering the work functions. Due to this capability, PEIE and PEI have been used for modifying the work function of metals and metal oxides in organic electronics[106]. Figure 3.13 shows the molecular structure of PEIE.
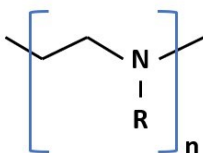
Figure 3.13. Molecular structure of PEIE, R could be replaced by $CH_2 CH_2 NR_2$, H or $CH_2 CH_2 OH$

46

3.2.4. Solvents

One of the great advantages of the new generation of optoelectronic devices is their solution processable fabrication techniques. The study of the effect of the solvents in thin film formation during the drying process has led to a new branch in organic electronics called solvent engineering[49]. Also, knowledge on the solute and solvent is critical in the fabrication of low loss, highly stable organic electronic devices. Various solvents were favorable for different steps of this project. For example, dimethyl sulfoxide reduces the evaporation rate. So, introducing a fraction of it in a solution made out of dimethylfomamide lingers the evaporation and give the perovskite structure more time to crystallize. A list of the solvents used in this work with their basic properties is provided in Table 3.1.

Table 3.1. List of solvents used in this work for fabrication of optoelectronic components

Solvent	Chemical Formula	Density (g.mol^{-1})	Boiling Point	UV-vis (λ_{max}, nm)	Refractive Index
Propanol (IPA)	C_3H_8O	0.786	82.6	210	1.3776
Dimethylformamide (DMF)	C_3H_7NO	0.948	152-154	270	1.4305
Dimethyl Sulfoxide (DMSO)	C_2H_6OS	1.1004	189	275	1.479
Toluene	C_7H_8	0.87	111	207	1.497
Gamma-Butyrolactone (GBL)	$C_4H_6O_2$	1.1286	204	215	1.435

3.2.5. Perovskites

The first perovskite compound was discovered in the eighteenth century and was a calcium titanium oxide mineral composed of calcium titanate ($CaTiO_3$)[107]. The crystalline structure of calcium titanate, ABX_3, was later considered as the most practical framework for functional materials[34]. Recently, synthetic perovskites also known as semiconducting pigments

have gained popularity in the field of photovoltaics due to their high efficiency and inexpensive

fabrication methods. In photovoltaic applications, the A site of the crystal is occupied by organic

compounds namely methylammonium or formamidinium. Dopants such as cesium in the crystal

would find their place next to the organic molecules. The B site is mainly occupied by a heavy

metal such as lead. Due to the adverse effect of lead on health and environment, alternatives

such as tin have been under consideration [108, 109]. The x site of the structure can be occupied

by halide ions. Perovskite materials display different absorption wavelengths depending on the

ratios of the halides or the concentration of the dopants. The absorption wavelength of different

ratios of the halides with and without a dopant (Cs) is shown in Figure 3.14[36].
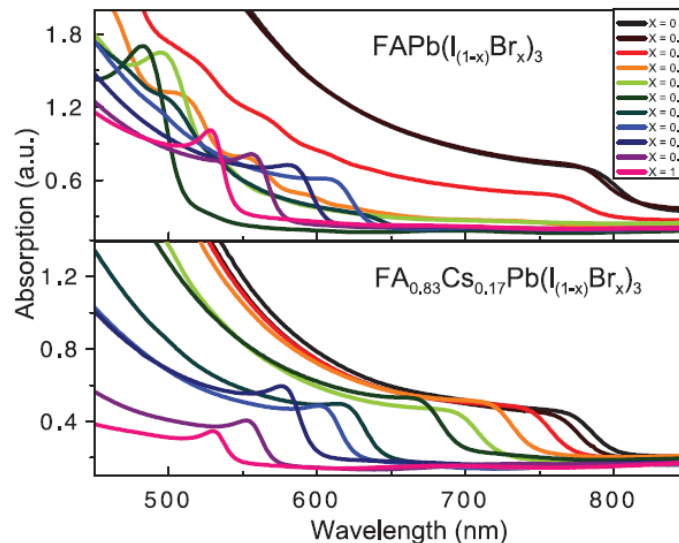
Figure 3.14. UV-Vis absorption spectra of light absorbing perovskites consisting of various ratios of halides without (top) and with (bottom) cesium as dopant. The copyright permission is included in the appendix[36]

3.3. Electrical Contacts

Photovoltaics require a transparent contact with light transmission coefficient of 1. The

contacts must possess low sheet resistance and surface roughness. The work function of the

anode and cathode should be selected based on the work function of the photoactive materials

and charge carrier transportation layers. In source photovoltaics such as solar cells, the work functions of the stacked materials must be matched to reduce the resistance and time constant. In this case of photodetectors, the mismatch in the work functions does not become significant due to the presence of the reversed bias. However, the reversed bias might result in band bending of the charge carrier transporting layers and consequently Fowler-Nordheim tunneling. This effect increases the dark current and must be prevented[110]. An anode material with a high work function is required to avoid tunneling effect and charge carrier transportation from the anode to the polymers. Table 3.2 contains the work functions and sheet resistances of the materials utilized as contacts in this dissertation.

Table 3.2. List of metal contacts utilized in this work and their electrical properties.

Material	Copper (Cu)	Gold (Au)	Aluminum (Al)	Indium Tin Oxide (ITO)	Fluorine-doped Indium Tin Oxide (FTO)
Work Function	4.70	5.10	4.08	4.40	5.00
Resistivity (Ω.m)	1.68×10^{-8}	2.44×10^{-8}	2.82×10^{-8}	1.5×10^{-7}	8×10^{-7}

3.4. Fabrication of Perovskite-Based Image Sensors

Commercial Indium Tin Oxide (ITO) coated glass substrates (15Ω sqr^{-1}) were cleaned through a sequential sonication in Decon liquid detergent, deionized water, acetone and methanol each for 30 minutes. The ITO substrates then were dried using nitrogen flow. Image sensors were fabricated using cleaned commercial ITO glass substrates. PEDOT:PSS was spin-coated on ITO at 1,000 rpm for 10s and 3,000 rpm for 30s. The film was annealed at 100°C for 20 minutes. Following a one-step deposition method, perovskite solutions were spin coated at 2,000rpm for 45s and annealed at 100°C for 40 minutes. A layer of PCBM in toluene (10mg/ml) was then spin coated at 2,000 rpm for 45s and cured at 100°C for 20 minutes. The fabrication

process was carried out in a nitrogen-filled glovebox with $O_2<30$ ppm and $H_2O<1$ ppm. In order to deposit a 20 nm of chromium and 200 nm of gold contact on the stack of materials and avoid chemical etching, a shadow mask was employed in a sputtering process. The schematic of the device configuration is shown in Figure 3.15.
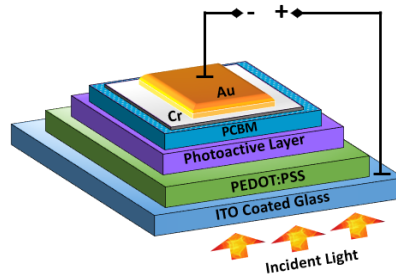
Figure 3.15. Regular p-i-n configuration consisting of the layers utilized in this study

3.5. Experimental Setup

Figures of merit for optoelectronic components are introduced in great length in chapter 2. In order to characterize the image sensors and measure their figures of merit, customized experimental setup was designed. The absorption spectrum of the imagers, the noise level, the magnitude and phase of the detected signals by the photodetectors were measured using the setup shown in Figure 3.16.
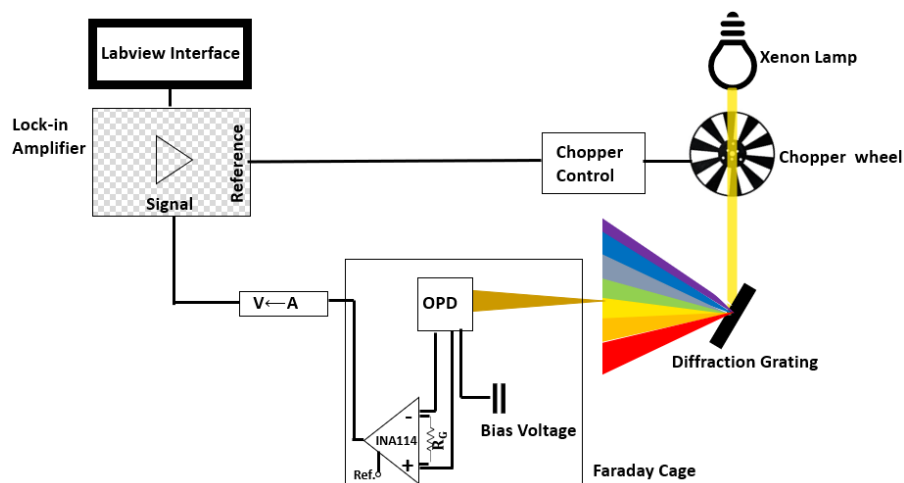
Figure 3.16. The custom-made spectral response setup for characterization of the image sensors

50

The I-V characterization was performed using a semiconductor analyzer, HP4145B. The equivalent circuit model of an image sensor is introduced in Figure 3.17.
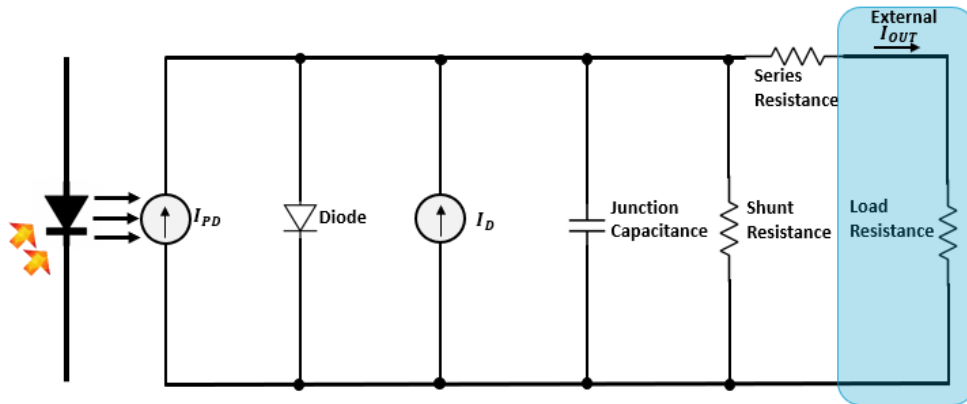
Figure 3.17. Equivalent circuit model for an image sensor. Each pixel may be modeled based on a diode with parasitic capacitance and resistances associated with it. The output current is a sum of the photodiode current and the dark current

I_{PD} represents the number of generated charge carriers upon illumination and before recombination. An ideal photodiode requires a shunt resistance of ∞ and a series resistance of zero. The value of each of the components may be measured from the dark and light I-V characteristics of each pixel. Figure 3.18 is an illustration of the extracted information from semilogarithmic I-V plots.
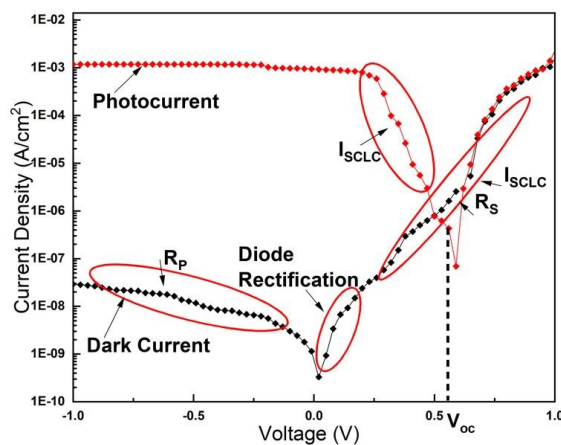
Figure 3.18. I-V plots of an image pixel with an inverted n-i-p configuration in dark and under illumination. R_p is the shunt resistance, R_s is the series resistance, I_{SCLC} is called space charge limited current

The low charge carrier mobility in organic semiconductors results in accumulation of charges and creation of counter electric field. This effect reduces the overall current throughput. This current is called space charge limited current and may be calculated using Mott-Gurney equation[111]:

$$I_{SCLC} = \frac{9\varepsilon\mu V_a^2}{8L^3} \qquad (1)$$

where ε is the dielectric constant, μ is the mobility, V_a is the voltage applied across the stack of material and L is the thickness of the stack of the materials. This equation may only be valid for films with no trap states with an exception of shallow traps with trapping time shorter than the charge carrier transit time[112]. Reverse bias condition exacerbates the undesired charge accumulation and consequently impedes photocurrent generation. I_{SLCS} may surface in forward bias region where the current slop increases, V^m with $m \geq 2$. Higher forward biases eliminate the trap states and the slope of the current transitions from $V^{m \geq 2}$ to V^2[112].

3.6. Thickness and Morphology

The thickness of each film and the roughness of the surface was measured using Dektak 150 surface profiler. In this profiler, a high precision stage is programmed to move the sample beneath the diamond-tipped stylus with a pre-determined scan length, speed and stylus force. These measurements are crucial in determining the performance of the optoelectronic components. The roughness of the surface is directly related to the interface of the layers determining the efficiency of the charge carrier transportation.

The thickness of the layers must be selected based on the diffusion length of the charge carriers and their mobility which are intertwined with the quality of the deposited thin film. In fabrication of the image sensors, the thickness of the films determines the shunt resistance of

52

the device. It is a common practice to increase the thickness to achieve higher shunt resistance, this approach is beneficial in reducing the dark current[113, 114]. Yet, lower dark current may be associated with lower quantum efficiency, as thicker films may increase the rate of recombination and suffer from the space charge effects[115].

Scanning Electron Microscope (SEM) images were taken using Focused Ion Dual Beam Quanta 200 3D. The SEM images provide better visualization of the grain sizes and boundaries, the possible cracks on the surface and the interface between the layered structure. In this work, the effect of temperature and time on the perovskite thin films was studied based on their SEM images.

X-Ray Diffraction (XRD) characterization was performed on the perovskite thin films using Panalytical X'Pert Pro MRD. XRD patterns indicate the formation of the perovskites and their crystal orientation and phase. In the case of tuned bandwidth perovskite thin films for image sensors, the XRD patterns clearly illustrate the effect of incorporation of macromolecules on the crystallite size, crystal phase, and orientation. Also, the effect of additives such as chloride on crystallization of the perovskites may be investigated based on the XRD patterns.

Room temperature photoluminescence was used to identify the absorption edge (band gap) of perovskites thin films of different chemical compositions. To further study the intrinsic defects, low-temperature photoluminescence (PL) emission was collected, in the range of 35-140K. The PL excitation source was Coherent's Fiber Optic laser at 640 nm. An InGaAs photodetector was used with a built-in preamplifier and cooling system (for noise reduction). Signal detection was optimized using, Standard Research Corporation's Low-Noise Amplifier (model SR560), along with a chopper (EG&G model 197) and a lock-in amplifier (EG&G 5209).

SPEX 500M monochromator with a 600 groove/mm grating was used. The temperature was controlled using a closed loop Helium cryo-system, which included: CTI-Cryogenics refrigerator using a cold finger from Helix Technology Corporation (model 22), a custom-built cryo head (fused silica windows) and CTI-Cryogenics model SC compressor. A silicon diode with Lakeshore 805A temperature controller was used for temperature sensing and control. At select temperatures, the photoexcitation intensity measurement ranged from 80mW down to 10mW.

CHAPTER 4 : RESULTS AND DISCUSSION

In this chapter, the techniques described in chapter 3 were implemented to measure the characteristics of each optoelectronic component. The first section of this chapter includes the results regarding resolutions to the instability of the light absorbing perovskites. The second section contains the results of a detailed study on the device level charge carrier transportation mechanism, in solution processable perovskites, to enhance the color discrimination and constancy in the image sensors. Since the light absorbing perovskite structures display dual electronic and ionic conducting properties, various device configurations were considered to highlight each transportation agent, ion or electron. To study ion transportation, the configuration of a photoelectrolytic cell was employed[116][1]. For carriers with higher mobilities, regular solid-state p-i-n and inverted n-i-p configurations were utilized. The results of each study conclude this chapter.

4.1. Stability of the Perovskite

The application of organometal halide perovskite materials as sensitizers in preference to synthetic dyes, described in 2009, has accelerated development of the new generation of photovoltaic devices[117]. Perovskite solar cells (PSCs) have offered superior power conversion efficiency compared to other low-cost solar cells (i.e., thin films and dye-sensitized solar cells)[118, 119]. A broad spectrum of research on the operational mechanism and fabrication

---

[1] The study was published in the Journal of Applied Electrochemistry

methods of perovskite-based optoelectronic components has been conducted to continuously elevate their efficiency and eliminate their instability and toxicity[120-122]. The mobilized ions and their reaction to the external stimuli are considered as the source of instability in the perovskites[123]. The structure of a PSC resembles a dye-sensitized solar cell. Since dye-sensitized solar cells consist of liquid electrolytes, PSCs may also be fabricated using liquid electrolytes. This could be beneficial as liquid electrolytes offer faster ionic transportation compared to the solid-state ones. Therefore, the study of the photosensitive perovskite structures in the format of a solar cell, with a liquid electrolyte, accentuates the role of ionic transportation in the performance of the device and its instability.

Among the hybrid organic-inorganic perovskite materials (ABX₃), application of $CH_3NH_3PbI_3$ (A = CH_3NH_3, B = Pb, X= I) in photovoltaics has established the most promising results[124]. In order to form reproducible polycrystalline structures of perovskite thin films, the sequential two-step deposition method was adopted[47]. In this method, a layer of PbI_2 dissolved in a solvent (e.g. dimethylformamide, DMF) was first deposited on a metal oxide nanostructure. The film was cured on a hotplate to become uniformly dark yellow. A solution of CH_3NH_3I (methylammonium iodide, MAI) in isopropanol then was deposited on the PbI_2 layer to form the perovskite crystalline structure. An instantaneous color change from dark yellow to black was observed once MAI solution came into contact with the PbI_2 layer. This color change indicated the formation of the crystalline perovskites. The second deposition step was followed by a heat treatment to eliminate the moisture and improve the surface morphology.

The chemical reaction in perovskite formation process is shown below:

$$PbI_2(\text{solid}) + CH_3NH_3I(\text{liquid}) \rightarrow CH_3NH_3PbI_3(\text{solid}) \tag{1}$$

56
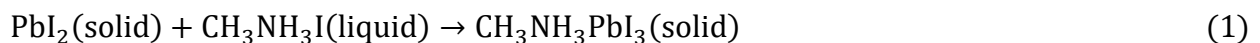
4.1.1. Stability Test in Liquid Medium

One of the root causes of the degradation in light absorbing perovskites is the hygroscopic nature of their constituent, methylammonium cation[125]. To study the properties of $CH_3NH_3PbI_3$ in a liquid medium, the perovskite films were tested in different organic solvents, including propylene carbonate and isopropanol. The film was not stable in a nonaqueous-based electrolyte, likely due to the moisture in the solvent. The degradation of the film to its constitutive precursors, CH_3NH_3I and PbI_2, was visible as the film color changed from black to dark yellow indicating the presence of PbI_2. The resolution to this problem manifested itself via administration of methylammonium iodide molecules dissolved in isopropanol as the electrolyte medium. We noticed a degraded perovskite film can be restored by exposing the damaged structure to the MAI-based electrolyte. The restoration process became evident through the color change of the film from dark yellow to black, again. Although a similar approach has been applied for fabricating a device by Xu et al., the stability and functionality of the perovskite film in the electrolyte were discussed in a limited scope[126]. The electrochemical characteristics of the fabricated perovskite-based solar cell with the customized electrolyte prove the stability of the film. Followings are the characterization results of the perovskite films deposited on two different mesoporous scaffolds, zinc oxide (ZnO) and titanium oxide (TiO_2) and studied during their dynamic restoration.

4.1.1.1. Electrode Fabrication

Fluorine-doped tin oxide (FTO) substrates (sheet resistance of 4 Ω/□) sized to 1 cm × 4 cm underwent several cleaning steps: soap, solvent, and mild acid cleaning with a deionized water rinse after each step [34]. The fabrication process of the electrodes is shown schematically in

Figure 4.1. For the ZnO nanowire (NW) growth, each FTO substrate was designed to have a 1 cm × 1 cm active area, and the rest of the surface was covered using Kapton tape. The conventional hydrothermal method was adopted for NWs growth[127]. The seeding solution (10 mM of zinc acetate in ethanol) was spin coated on the active area of the FTO at 1500 rpm for 45 s. The sample was then annealed at 150°C on a hot plate for 2 min. The seeding deposition process was repeated 10 times. The prepared substrate was placed face down in a bath of growth solution containing 25 mM of each, zinc nitrate hexahydrate, and hexamethylenetetramine, in DI water for 2 h. The growth bath setup had a constant temperature of 90°C and the growth solution was stirred at 250 rpm. After the growth, the active area was rinsed with DI water and ethanol.

For TiO_2 coating, the active area was sized to 0.5 cm × 1 cm. A layer of TiO_2 was doctor-bladed and sintered up to 500°C with the rate of 5°C/min and ramped down to 80°C with the rate of 5°C/min[128]. The sintered TiO_2 substrates were then treated with 55 mM $TiCl_4$ at 90°C for 30 min and rinsed with DI water and ethanol. The substrates were subsequently ready for the sequential perovskite deposition. A 1M concentrated PbI_2 in DMF was spin coated at 3000 rpm for 20 s on the fabricated ZnO and TiO_2 electrodes. After the deposition of PbI_2, the samples were cured on a hotplate at 90°C for 10 min. The next step was to drop casting a 0.05 M concentrated MAI in isopropanol on the substrates and curing the electrodes on a hotplate at 90°C for 10 min[129]. Four FTO electrodes with different coatings were prepared for the experiments. The coatings were ZnO NW, ZnO NW-perovskite, TiO_2, and TiO_2-perovskite. The fabricated electrodes were used as photoanodes in the electrochemical cells with an MAI-based electrolyte containing 0.05 M concentration of each $LiClO_4$ and MAI in isopropanol.
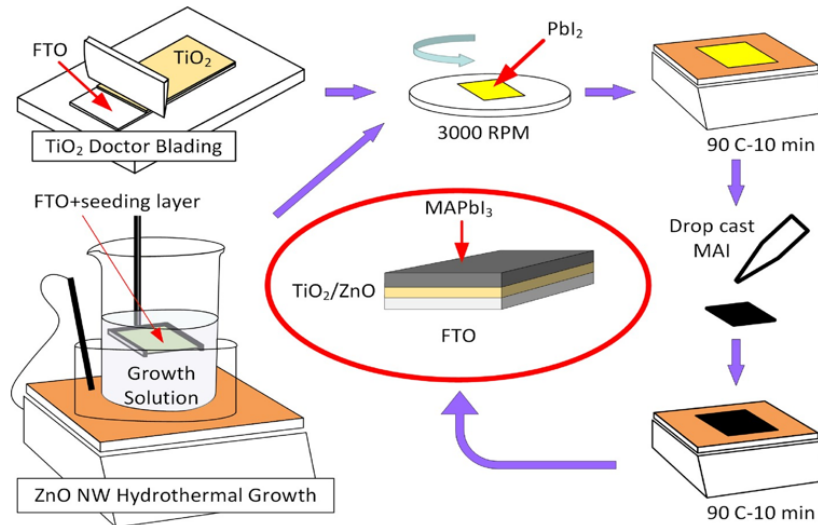
Figure 4.1. Electrode fabrication procedure using doctor blading technique for TiO$_2$ deposition and hydrothermal method for ZnO growth. The FTO substrate coated with TiO$_2$/ZnO then underwent a sequential two-step deposition procedure: spin coating of PbI$_2$ at 3000 rpm and drop casting of MAI, each step was followed by an annealing at 90°C for 10 min. The fabricated electrodes are shown as three-layered structures. The copyright permission is included in the appendix[116]

4.1.1.2. Energy Band Diagram

The energy band diagram of the electrodes with two different metal oxide scaffolds is shown in Figure 4.2[130]. Despite the fairly similar energy band gap between TiO$_2$ and ZnO, the cascaded energy levels in the electrode with TiO$_2$ mesoporous structure might be the reason for a more efficient charge transfer. While the presented results confirm the stability and functionality of the perovskite layer in the electrolyte, a more in-depth study is required to optimize the charge circulation in a perovskite-based electrochemical cell. In particular, the effect of charge mediators in the electrolyte has to be studied to design a cell with a higher photocurrent.
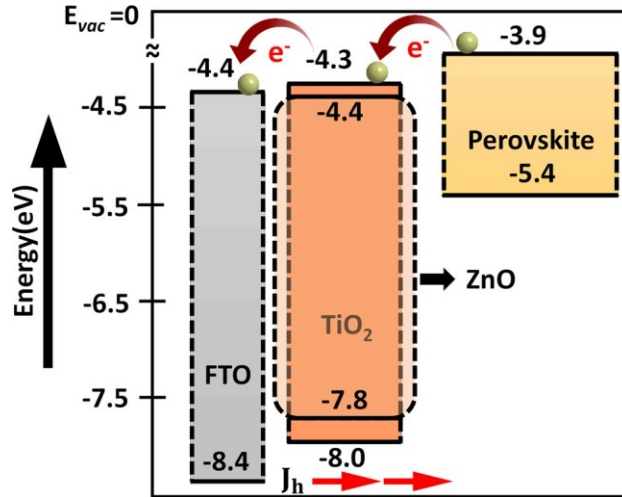
Figure 4.2. Energy level diagram of an electrode with two different metal oxide mesoporous scaffolds. The energy levels are referenced to vacuum level. The copyright permission is included in the appendix[116].

4.1.1.3. X-Ray Diffraction Characterization

In order to confirm the stability of the perovskite layer in the MAI-based electrolyte, X-ray diffraction pattern of the perovskite layer was acquired before and after the electrode was exposed to the electrolyte for the period of the experiment. The crystalline structure of the materials was then analyzed, and the peaks were indexed. The results are shown in Figure 4.3 (a) and (b). Different phases of perovskite structure were not labeled in the figures to prevent possible complications.
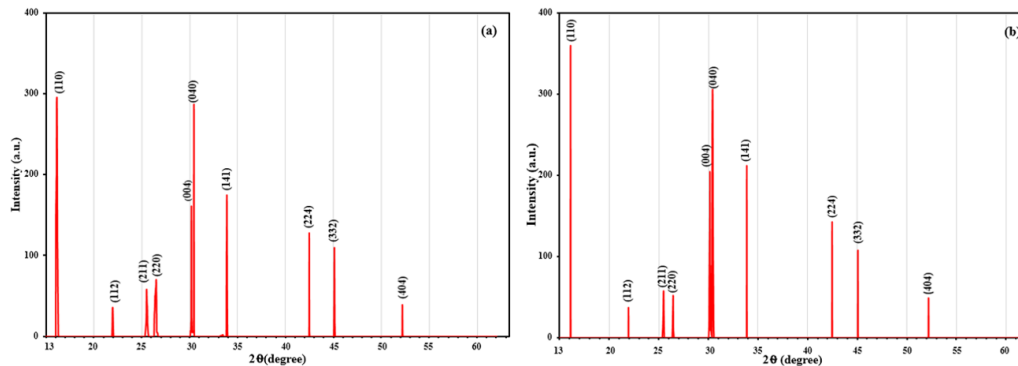
Figure 4.3. XRD patterns of the TiO_2–perovskite crystalline structure before (a) and after (b) being exposed to the electrolyte. The copyright permission is included in the appendix[116]

These XRD results are supported by data reported in similar studies[131-134]. The XRD pattern of the perovskite structure, after its exposure to the electrolyte, demonstrated almost no degradation. In fact, the higher intensity of the peak for (110) and slight reduction of the peak for (220) after the insertion of the electrode into the electrolyte suggest the constructive effect of the electrolyte on the crystalline structure to its main orientation at (110). The rest of the peaks were almost the same before and after exposing the film to the electrolyte.

4.1.1.4. Electrochemical Study

To study the photochemical reactivity of perovskite materials, each of the fabricated electrodes was tested in a three-probe cell, in the dark and under simulated solar radiation. First, the electrodes were studied in a cyclic voltammetry (CV) experiment, in which the voltage of the working electrode was scanned back and forth multiple times between −0.8 and +0.8 V (versus the reference electrode) with a constant scan rate of 50 mV s^{-1}. The CV results for each of four samples, in dark and light conditions, are shown in Figure 4.4. As shown in Figure 4.4(a), there is no evidence of reaction between the ZnO NWs and the electrolyte. Also, no difference was observed between dark and light responses explaining the absence of the photosensitive material. The rectifying behavior in the I-V curve may be attributed to the existence of an energy barrier at the ZnO-electrolyte interface. The response of the electrode with TiO$_2$ mesoporous structure was also rectifying, Figure 4.4(c). However, unlike ZnO NWs, the redox peak representing the reaction between the electrode and the electrolyte was well pronounced in the case of the TiO$_2$ mesoporous structure. Nevertheless, little difference was observed when the sample was tested in dark and light conditions.

As expected, the samples with the perovskite layer presented the photovoltaic behavior by introducing nonzero currents at zero bias under illumination, Figure 4.4 (b) and (d). Also, the footprint of the double layer was evident from the hysteresis. The observed redox peaks may be attributed to the oxidation of the iodide molecules from I^- to I^0 [135]. Since the same peak was detected in Figure 4.4 (c), the redox peak was likely due to a reaction from the ions inside the electrolyte and not the perovskite. It should be noted, the sample with the TiO_2-perovskite, Figure 4.4 (c), presented such a high photocurrent that the redox peak was barely visible in the CV result for the illuminated condition.
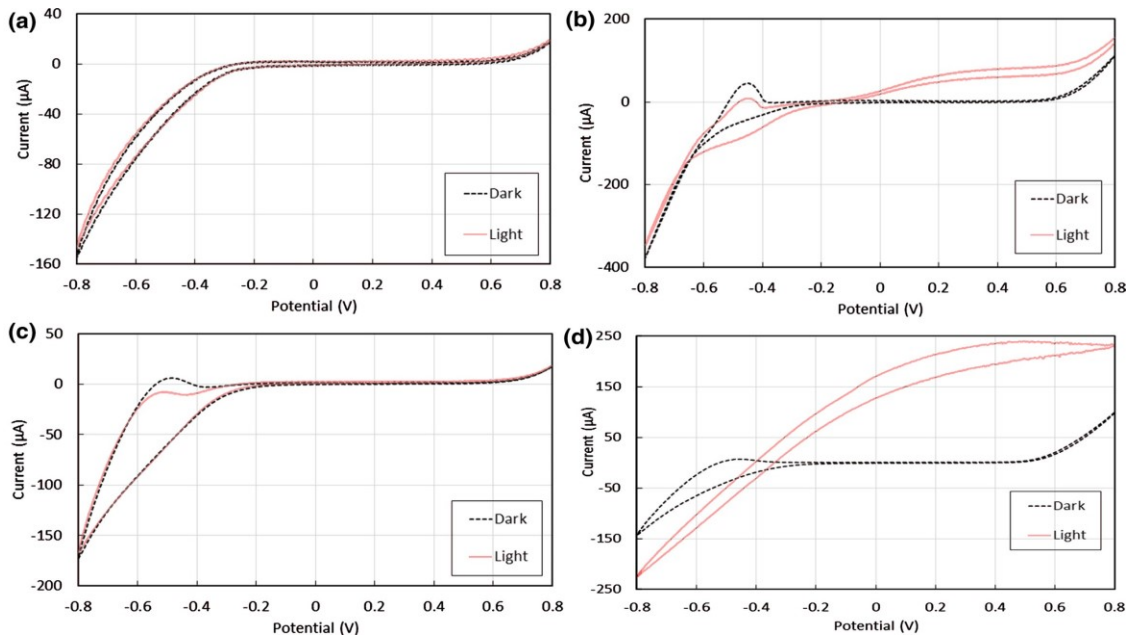
Figure 4.4. CV results under the dark and light conditions in four different samples: (a) ZnO NWs without perovskite; (b) ZnO NWs with perovskite; (c) TiO_2 without perovskite; (d) TiO_2 with perovskite. The copyright permission is included in the appendix[116]

To study the photocurrent, the samples with the perovskite layer were biased at 0 V versus open circuit voltage in the dark. The current was monitored when the samples were exposed to pulses of light. The photocurrent results are presented in Figure 4.5 (a). The up arrows show the onset of illumination and the down arrows demonstrate the light cessation. The peak

photocurrent in the electrode with TiO$_2$ mesoporous scaffold was 237 µA cm^{-2}. The open circuit voltages of the electrodes with coated perovskite materials are also shown in Figure 4.5 (b). The voltages were measured versus Ag/AgCl reference electrode. The ΔV between the dark and light conditions was 0.401 and 0.135 V in the TiO$_2$-perovskite and ZnO-perovskite electrodes, respectively. Both the photocurrent and open circuit voltage plots clearly indicated the premier functionality of the perovskite materials on TiO$_2$ compared to ZnO. The gradual change of voltage on illumination and the sudden drop of voltage in the transition from light to dark, in both electrodes, suggested the charge transfer rate at the perovskite–electrolyte interface was very different under the dark and light conditions. To explore the differences, the impedance of both electrodes was measured under the dark and light conditions.
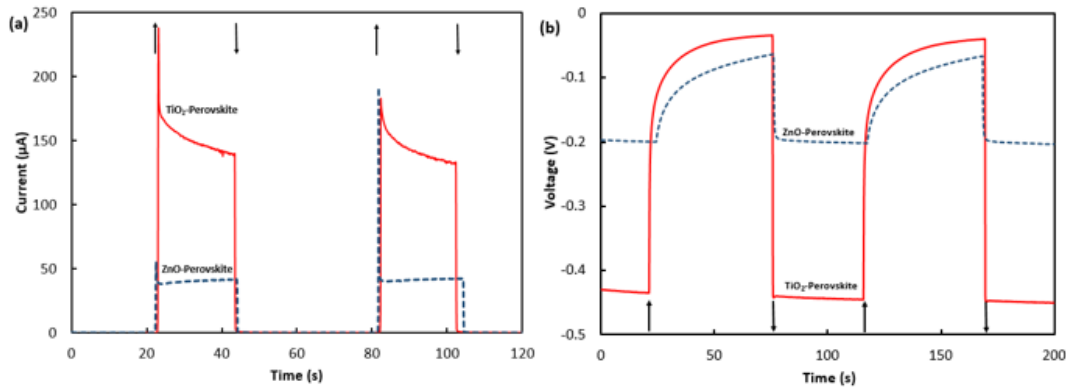
Figure 4.5. (a) Photocurrent in the cells with TiO$_2$-perovskite and ZnO-perovskite working electrodes. (b) Open circuit voltage in the cells with TiO$_2$-Perovskite and ZnO-Perovskite working electrodes. Arrows up and down show the transitions for turning on and off the light source, respectively. The copyright permission is included in the appendix[116]

The experimental electrochemical impedance spectroscopy (EIS) measurements were performed on the cells within the range of 50 mHz–100 KHz. The results of Bode plots for ZnO-perovskite and TiO$_2$-perovskite samples in the dark and light are shown in Figure 4.6. For frequencies higher than 100 Hz, the differences between dark and light conditions in both

samples were negligible. However, significant changes were observed at low frequencies when the samples were under illumination.
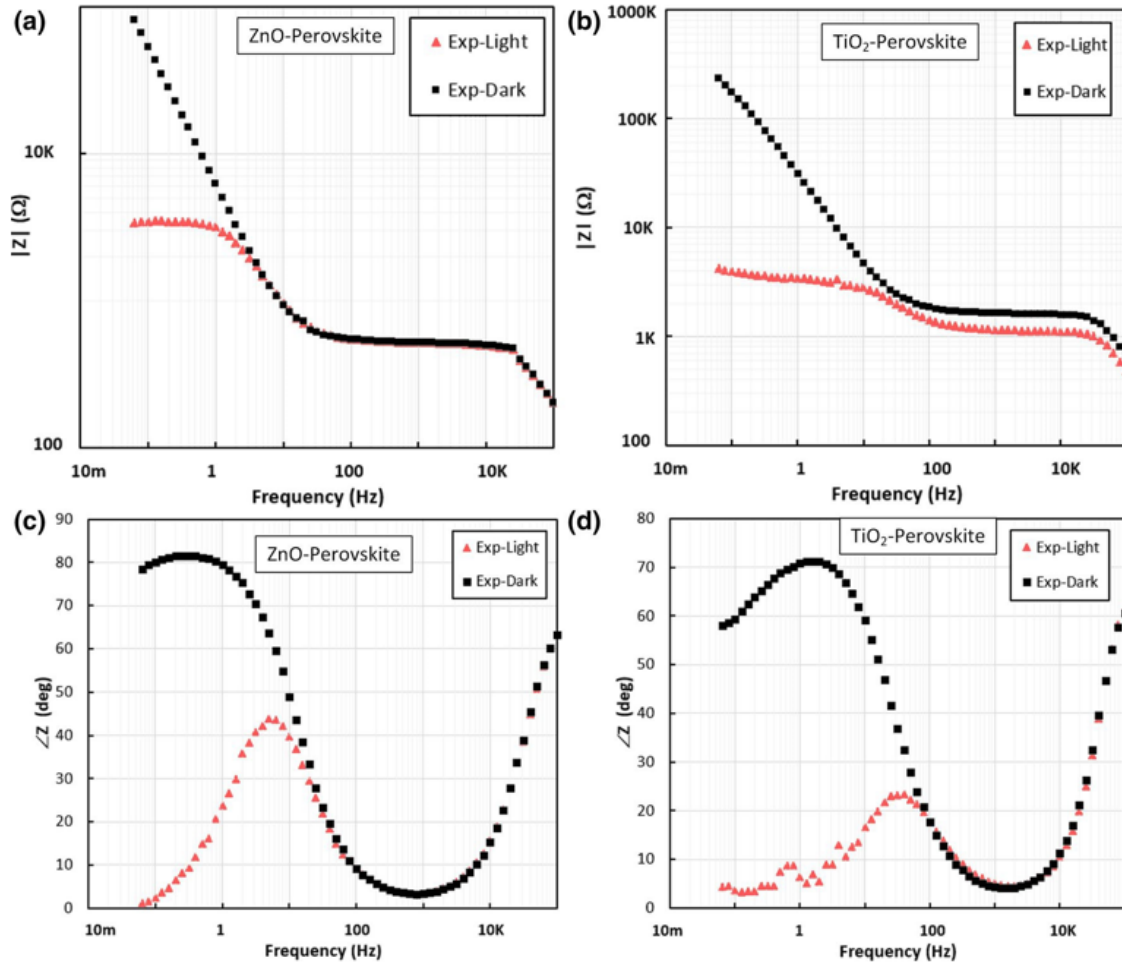
Figure 4.6. Bode plots representation of the EIS results for the ZnO-perovskite and TiO$_2$-perovskite electrodes under the dark and light conditions. (a) The magnitude and (c) the phase results for the ZnO-perovskite electrode; (b) the magnitude and (d) the phase results for the TiO$_2$-perovskite electrode. The copyright permission is included in the appendix[116]

Considering the phase and magnitude data at low frequencies, the samples presented greater capacitive behavior and higher impedances in the dark. After illumination, the sample with the TiO$_2$ back contact showed an impedance drop at 63 mHz, almost two orders of magnitude. The drop of the impedance for the illuminated ZnO sample was also significant (~23 times), but substantially less than the change of the TiO$_2$ sample. The phase data showed the

low-frequency impedance for the illuminated samples was more resistive than capacitive. Nevertheless, the dark and light results implied impedances with more than one time constant in both samples.

A two-stage equivalent circuit model was proposed due to the semiconducting structure of the perovskite and the electrode-electrolyte interface, inset in Figure 4.7(a). The first stage of the model included a capacitance, C_{PVSKT}, for the depleted region in the semiconductor and a parallel resistor, R_{PVSKT}, for the charge transfer through the perovskite layer. At the electrode-electrolyte interface, we expected a double-layer capacitor, C_{dl}, and a charge transfer resistance, R_{ct}. Additionally, the linear curve with a 45 degree angle in the Nyquist plot, especially for the dark experiments, Figure 4.7 (a) and (c), suggested a Warburg impedance element (W). The Warburg impedance is an indication of the effect of ion diffusion[136].

The proposed model was confirmed on the basis of a well-matched equivalent electrical circuit simulated by ZSim and the values for the components were extracted and tabulated in Table 4.1. As shown in Figure 4.7, the simulation results for the extracted component values corresponded to the experimental results for both samples in dark and light. In both ZnO and TiO$_2$-based electrodes, the values of R_{ct} and W varied highly between dark and light (Table 4.1). Increasing the conductance of W by three orders of magnitude, under illumination, suggested that the photoexcited reaction at the electrode-electrolyte interface was likely more kinetic-limited than diffusion limited, whereas the small value of W in the dark could imply the dominance of the diffusion limited mechanism.
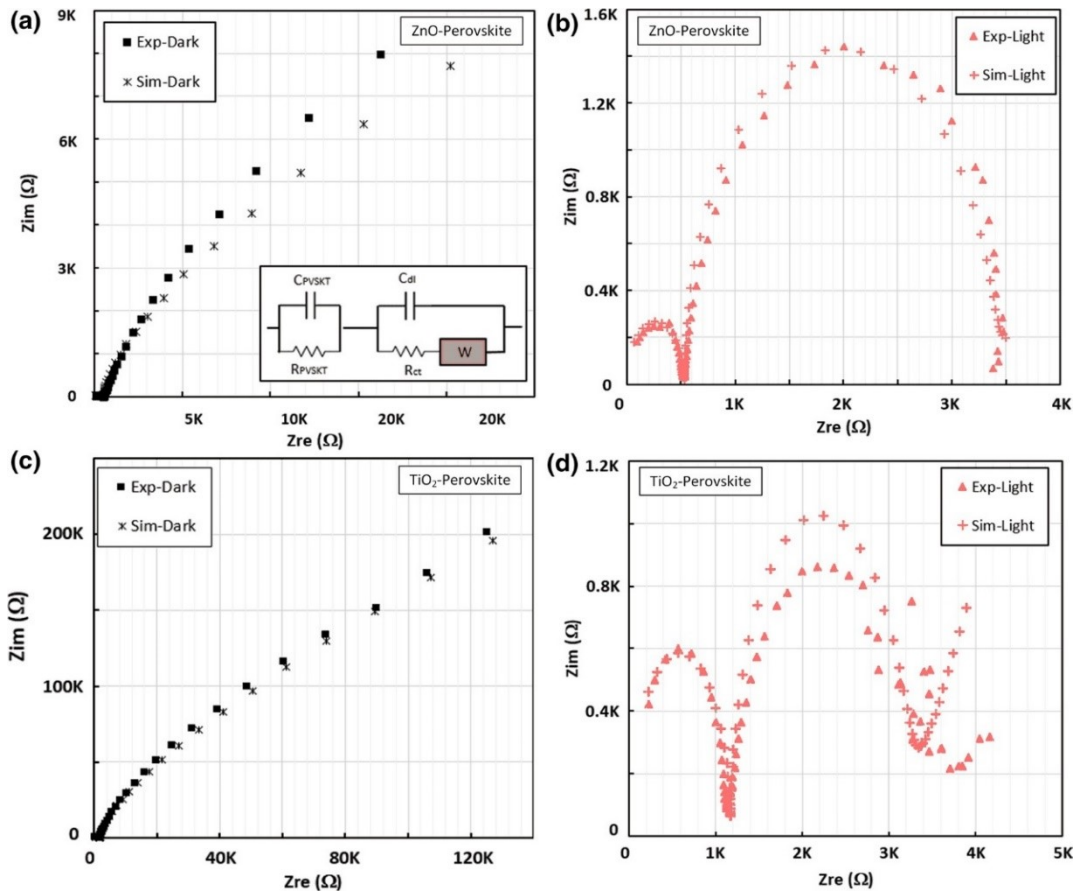
Figure 4.7. Nyquist plots of the ZnO-perovskite electrode in the (a) dark and (b) light; and the TiO$_2$-perovskite electrode in (c) dark and (d) light. The simulation results for the proposed model are presented in all four plots. (Inset in (a): The proposed equivalent circuit model). The copyright permission is included in the appendix[116]

In both samples, the electrochemical interface was between the perovskite and the

electrolyte. The results accentuated the role of the electron transport layer (i.e. ZnO and TiO$_2$).

The large difference between the C$_{dl}$ values.

Table 4.1. Simulated values for the components in the proposed equivalent electrical circuit model. The copyright permission is included in the appendix[116]

Description	R$_{PVSKT}$ (Ω)	C$_{PVSKT}$ (nF)	C$_{DL}$ (μF)	R$_{ct}$ (Ω)	W
ZnO-Perovskite (Dark)	533.3	7.670	22.94	71.64	6.99E−06
ZnO-Perovskite (Light)	530.5	7.692	24.06	2844	9.51E−03
TiO$_2$-Perovskite (Dark)	1687	2.022	3.28	16.63	5.23E−06
TiO$_2$-Perovskite (Light)	1169	2.781	3.61	2012	1.56E−03

66

Table 4.1 suggested the effective surface area of the perovskite, exposed to the electrolyte, was about 7 (22.94 µF/3.28 µF) times larger in the sample with ZnO back contact than in the TiO$_2$ based electrode, while the apparent area was only twice larger. This indicated the morphology of the perovskite layer could be affected by the structure of the underlying layer (i.e. ZnO NWs and TiO$_2$ mesoporous structure). Despite the large junction area in the ZnO sample, the photocurrent was at least three times larger in the TiO$_2$ sample than the ZnO-perovskite electrode, Figure 4.5(a). This indicates a higher charge transfer rate from perovskite to TiO$_2$ than perovskite to ZnO.

4.1.2. Stability Test by Defect Engineering[2]

Previously developed approaches for conventional semiconductors based on established heuristics such as Vegrad's and Varshini's laws have been adopted to shed a light on the fundamentals of the new generation of semiconductors[35, 137]. Implementation of these laws resulted in an understanding of the effect of various ratios of halides, X site, in the performance of perovskite-based optoelectronics[138]. Profound studies on the substitution of the metal site of the photosensitive perovskite from lead to tin have also been conducted[139, 140]. However, the complexity of the A site of these organometal halides has led to little understanding of their effect on the lattice structure and device performance. Generally, in solid state compounds, the crystal structure is a function of the relative atomic sizes, volume per valence electron, Brillouin zone edges of each constituent, and electrochemical differences between them[141]. Also, the presence of intrinsic defects changes the dynamics of the lattice structure[142]. The latter motivated us to add excess organic molecules to the precursor solution of the perovskite to

---

[2] This study is under review in the Journal of Organic Electronics

create intrinsic defects. We then studied the resulting deviations from the norm due to the presence of the defects. Our study highlighted the role of the organic molecules in the degradation process of the perovskite structure in both the materials and at the device level.

Among all the photosensitive perovskite structures, MAI:PbI$_2$, where MAI stands for methylammonium iodide (A site) with the chemical formula of CH$_3$NH$_3$I, has demonstrated the highest power conversion efficiencies in optoelectronic applications[143]. This effect is attributed to the relatively small electron affinity of the iodine constituents[144]. Therefore, the structure of MAI:PbI$_2$ is significant and the focus in this study. Aristidou et al. considered fast oxygen diffusion and iodide defects to be the cause of photodegradation in the perovskite structure[145]. However, the degradation in the perovskite structures might not be limited to oxygen diffusion or iodide defect migration, and further investigation is required. For this study, Schottky and Frenkel defects were introduced to the crystalline lattice using selected concentrations of MAI[142, 146]. In ionic solution, Schottky defects consist of equivalent number of positive and negative vacancies formed due to the lack of molecules such as CH$_3$NH$_3$I and PbI$_2$ in the lattice. These defects are benign and do not demonstrate characteristics of the trap states. Alternatively, Frenkel defects include equal number of vacancies and interstitials of ions such as CH$_3$NH$_3^+$, I$^-$ or Pb^{2+}. The vacancies are propelled by the gradient of electric charges towards the interstitials[147]. These defects are to be considered as dopants[147]. The trap sites are only formed where the concentration of MAI is insufficient to form stable, non-distorted [PbI$_6$(CH$_3$NH$_3$)$_n$]$_m$ clusters[148, 149].

4.1.2.1. Perovskite Film Fabrication

Commercial Indium Tin Oxide (ITO) coated glass substrates (15Ω sqr^{-1}) were cleaned through a sequential sonication in Decon liquid detergent, deionized water, acetone and methanol each for 30 minutes. The ITO substrates then were dried using nitrogen flow. Various ratios of MAI and PbI_2 were dissolved in DMF and sonicated for 30 minutes, see Table 4.2. Three different stoichiometric ratios were selected to ensure complete reaction between the precursors. Other ratios were selected to create excess reactant in the solution. As a result, Ratios A, C and E are the most frequently used photoactive perovskite structures. [143, 150]. Ratios B and D have never been considered for optoelectronic applications. This selection perfectly aligned with our approach of considering excess MAI as defect forming molecules in the structure. A one-step deposition of perovskite solution on bare ITO substrate was adopted[151]. Perovskite solutions were spin-coated on bare ITO at 1,000 rpm for 20 s and at 2,500 rpm for 40 s. For the purpose of this study, all the prepared films were annealed at 100°C to limit the effect of temperature on phase transition and crystallization[132, 152, 153]. The film preparation was carried out in a nitrogen-filled glovebox with O_2<30 ppm and H_2O<1 ppm. The resulting film had a thickness of 500 nm with varying average roughness of less than 100 nm for each Ratio.

Table 4.2. Ratios under test with various MAI to PbI_2 concentrations. The copyright permission is included in the appendix[154]

Ratio A	Ratio B	Ratio C	Ratio D	Ratio E
$1MAI:1PbI_2$	$2MAI:1PbI_2$	$3MAI:1PbI_2$	$1MAI:2PbI_2$	$3MAI:1PbCl_2$

Photodetectors were fabricated using cleaned commercial ITO glass substrates. PEDOT:PSS was spin-coated on ITO at 1,000 rpm for 10s and 3,000 rpm for 30s. The film was annealed at 100°C for 20 minutes. Following a one-step deposition method, perovskite solutions were spin coated at 2,000rpm for 45s and annealed at 100°C for 40 minutes. A layer of PCBM in

toluene (10mg/ml) was then spin coated at 2,000 rpm for 45s and cured at 100°C for 20 minutes. The fabrication process was carried out in a nitrogen-filled glovebox with $O_2<30$ ppm and $H_2O<1$ ppm. In order to deposit a 500 nm thick aluminum contact on the stack of materials and avoid chemical etching, a shadow mask was employed in a sputtering process. The schematic of the device configuration is shown in Figure 4.8.
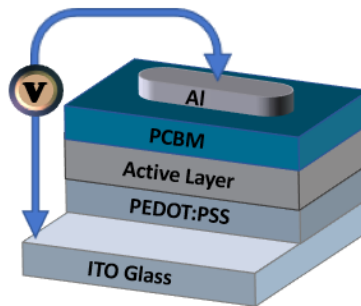

Figure 4.8. Schematic of the configuration of the photodetectors. The copyright permission is included in the appendix[154]

4.1.2.2. Photoluminescence Analysis

Room temperature photoluminescence (PL) was used to identify the emission wavelength of the varying Ratios. PL spectra were collected using an InGaAs photodetector with a built-in preamplifier and cooling system (for noise reduction). Signal detection was optimized using Standard Research Corporation's Low-Noise Amplifier (model SR560), along with a chopper (EG&G model 197) and a lock-in amplifier (EG&G 5209). SPEX 500M monochromator with a 600 groove/mm grating was used. The PL excitation source was Coherent's Fiber Optic laser at 640 nm. PL is a noninvasive technique used to probe the defect states of a semiconductor through the capture of radiative recombination transitions. Hence, the PL intensity is expected to be influenced by electronic defects[155]. In addition to defect states, the perovskite crystal is important, as the crystallite size, structure, and symmetry influence the material properties[150, 156]. High-quality films are those with fewer electronic defects, correlating with a reduced

70

number of sub-bandgap trap states. As shown in Figure 4.9, the PL intensity was substantially higher for Ratio A than for the other three Ratios. Also, Full Width at Half Maximum (FWHM) was narrower in Ratio A compared with other Ratios indicating stronger electron-phonon coupling in this Ratio[157]. Weaker electron-phonon coupling translates directly to lower charge carrier mobility[158]. We were not able to obtain the luminescence of Ratio E in the room temperature. To isolate the thermal influence on defect states, PL results were collected and reported at 30K for only Ratio E.
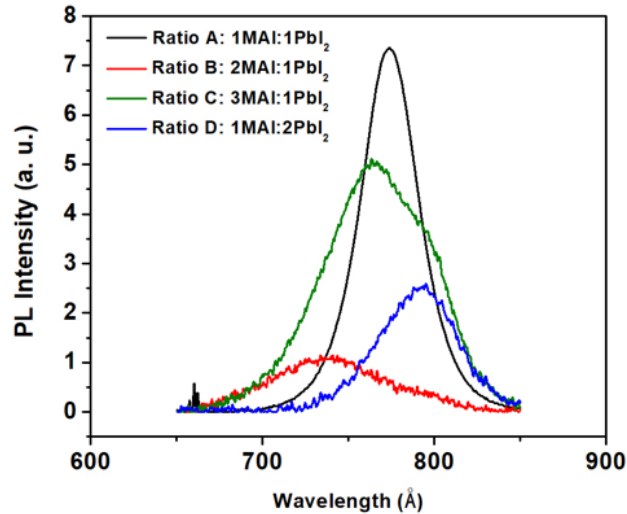

Figure 4.9. Room temperature photoluminescence spectra of different perovskite Ratios with excitation intensity at 80mW/cm^2. Ratio A and C are the most frequently used combinations for optoelectronic applications. Elemental defects such as MA vacancies might be the source of defect density in Ratios B and D. The copyright permission is included in the appendix[116]

In Figure 4.10 (b), the PL intensity versus excitation intensity is provided for all Ratios. The photoexcitation intensity measurement ranged from 80mW to 10mW. PL intensities for Ratios A through D were collected at room temperature while the PL for Ratio E was obtained at 30K.
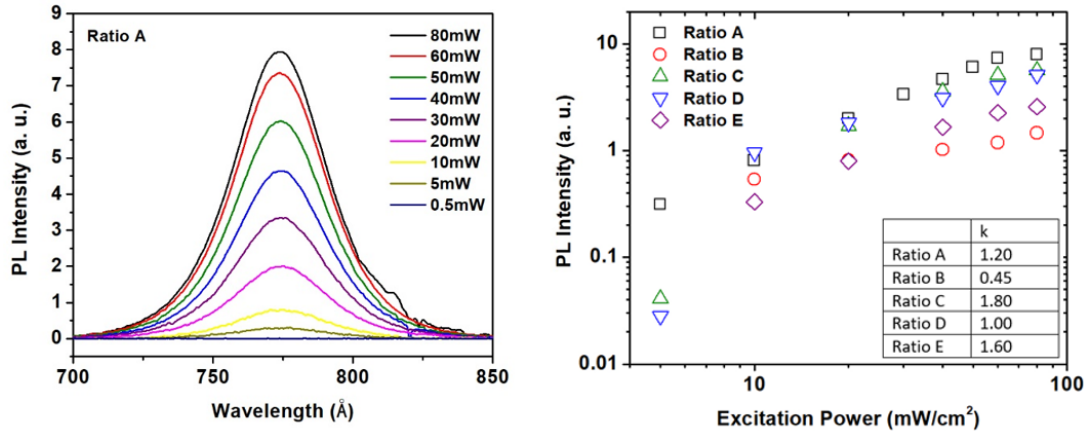
Figure 4.10. (a) Intensity dependence of MAI:PbI$_2$ film performed at room temperature; (b) Relationship between the photoluminescence intensity (I) versus excitation power (L), governed by $I \sim L^k$, where k values are shown in the inset. The copyright permission is included in the appendix[154]

Considering the PL peak positions presented in Table 4.3, the mixed halide precursor at Ratio A (773 nm) displays a 35nm red shift to Ratio B (738nm), a 10nm red shift to Ratio C (763 nm) and a 20nm blue shift to Ratio D (793 nm). In addition, the mixed halide precursor of Ratio E (560 nm) displayed a large blue shift compared to all the other Ratios, at low temperature.

Table 4.3. Wavelength of different Ratios. The copyright permission is included in the appendix[154]

	Wavelength (nm)
Ratio A	773
Ratio B	738
Ratio C	763
Ratio D	793
Ratio E	560

4.1.2.3. X-Ray Diffraction Analysis

XRD patterns from the perovskite structures indicated coexistence of cubic, tetragonal and orthogonal phases in each film. All the patterns were comprised of diffractions from (020), (110), (004), (220) and (224) in orthorhombic and tetragonal phases, see Table 4.4 and Figure 4.11. A sequence of diffraction planes was repeated in the first three Ratios. The only difference

in this sequential pattern was the appearance of (112) in Ratio B and (112) and (202) of tetragonal

phase in Ratio C. This observation is attributed to the increasing concentration of polar

methylammonium and iodide ions in the first three Ratios. Methylammonium ions with a C_{3v}

symmetry introduce disorder in cubic and tetragonal phases as their atomic positions cannot be

fixed in the unit cell of the structure[132, 153, 159].

Table 4.4. Peak heights for lattice planes of all the ratios. Superscript numbers show the lattice structure: Orthorhombic (1), tetragonal (2) and cubic (3), The copyright permission is included in the appendix[154]

	(020)[1]	(110)[2]	(112)[2]	(202)[2]	(004)[2]	(220)[2]	(211)[3]	(213)[1]	(224)[2]
Ratio A	6.07	14.90			12.89	16.45			0.20
Ratio B	10.12	43.34	0.92		19.43	44.52			0.53
Ratio C	5.03	15.64	1.39	0.18	13.65	17.69			0.51
Ratio D	0.61	0.75			0.11	0.83	0.08	0.27	0.31
Ratio E	40.60	42.86			17.31	13.97		5.68	0.69

In the case of tetragonal phase, the disorder is merely attributed to carbon and nitrogen

atoms. The iodide ions possess fixed atomic positions in tetragonal phase[160]. A smooth

transformation from tetragonal to cubic phase was observed in Ratios D, as shown by the peak

in the XRD plot in Figure 4.11. Coexisting tetragonal-orthorhombic phases indicated order-

disorder transition of methylammonium ions in the lead-iodide framework via hydrogen

bonds[161, 162]. This observation in Ratio E supports the long known effect of chloride ions on

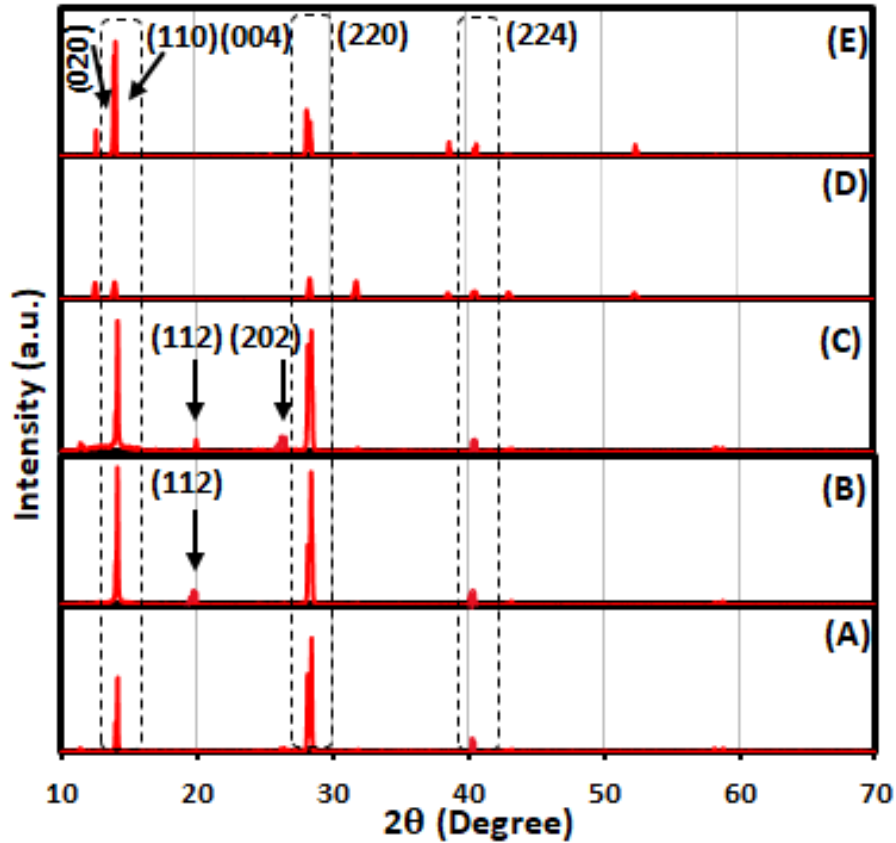ordering the unit cell structure reported by Luo et al[163].

Figure 4.11. XRD Patterns of all the Ratios. Common planes are shown on the plots. The copyright permission is included in the appendix[154]

The crystallite sizes were determined from FWHM values of the XRD peaks. The crystallite sizes were in sub-micron scale and comparable along various directions for all the Ratios except Ratio D. The FWHM of each peak in Ratio D was wider, indicative of the formation of nanostructures in the film. Ratio D registered a maximum of 64nm crystallite size in [220] direction and a minimum of 9.7nm in [022] direction. The higher concentration of lead iodide in Ratio D only reduced the crystallite size due to the additional effective charge in the hybrid resulting in tetragonal-orthorhombic phases[164]. Given the same thickness of each film, the peaks were more pronounced and intensified as the ratio of organohalide increased, see Figure 4.11. This might indicate higher degrees of crystallization in Ratios B, C and E, which translates directly to lower decomposition rate[165].

74

4.1.2.4. Scanning Electron Microscopy Analysis

It is known that perovskite deposition on a mesoporous template, such as PEDOT:PSS, facilitates the charge carrier transportation and minimizes the pinholes by condensing the film[166]. However, in this study the focus was on the variations in the morphology of different Ratios. Therefore, we eliminated the template and deposited the films on bare ITO. As shown in Figure 4.12, the morphology of the thin films varies from Ratio A to E. Hence, the grain sizes and domain structures differ for each Ratio. These effects are particularly important in applications based on ferroelectricity and piezoelectricity of perovskites[167, 168]. The grain size impacts the dielectric coefficient and remnant polarization as well as the coercive force[169, 170]. Ratio A displayed a uniform morphology with minimum pinholes and surface roughness, while Ratio B showed fibrous structures and porous texture. This feature of Ratio A results in highly reliable junctions in optoelectronic devices [171, 172].
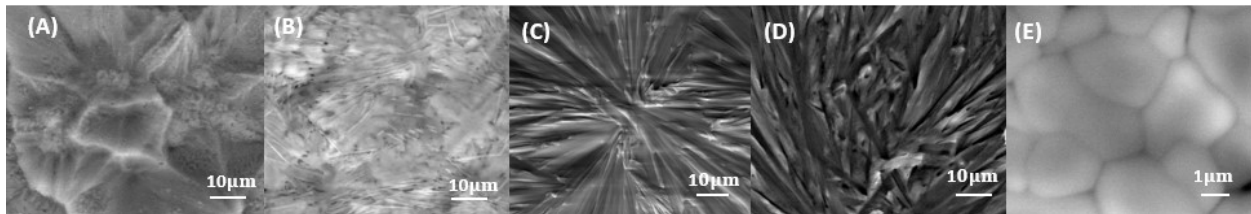

Figure 4.12. Scanning Electron Microscopy of the morphology of Ratios A-E on ITO glass with no mesoporous scaffold. The copyright permission is included in the appendix[154]

Ratio C formed palmate shaped microstructures with high surface area, suggesting higher light absorption compared with Ratio B. Also, the chemistry of the perovskite solution provides a bilateral reaction between methylamine and hydrogen iodide producing methylammonium iodide. The concentration in Ratio C might only form Schottky defects. Schottky defects are not considered as trap states[142] Therefore, their presence in the material does not affect the degradation rate.[123]. Two parts of lead iodide in Ratio D resulted in the roughest surface

75

among all Ratios. Although the surface was formed on submicron needle structures, the decomposition rate was extremely high, as there may have not been adequate methylammonium iodide constituents in the solid form to maintain the perovskite structure. The replacement of lead salt in Ratio E resulted in the formation of smaller grain sizes. The color of the film appeared metallic gray, noticeably different than the other four Ratios explored.

4.1.2.5. Electronic Properties

For the purpose of this study, we have presented the device performance in dark and under illumination. The dark current measurements address the effect of defect density in device level. The dark current level is primarily attributed to the mobility of the charge carriers, trap-assisted recombination, doping density of the semiconductor and work function of the electrodes[43]. Given the devices are identical except for their active layer, the changes in dark current level convey variations based on the functionality of the perovskite photosensitive layers and their physical structures. The dark current density at zero applied potential in the photodetectors is tabulated in Figure 4.13. Device D had the highest dark current density, 10^{-8} Acm^{-2} with a low shunt resistance [173]. This level of dark current and shunt resistance in Ratio D introduces reliability issues in the device level. Device D showcased the highest photocurrent among other devices. However, its open circuit voltage was zero. The ideality factor greater than one also indicates that in all of these active layers, the recombination current is dominant. Considering that higher thickness in these bulk materials results in higher shunt resistance, low values of dark current and high shunt resistances are attributed to the optimized thicknesses of the photosensitive materials[174].

www.manaraa.com

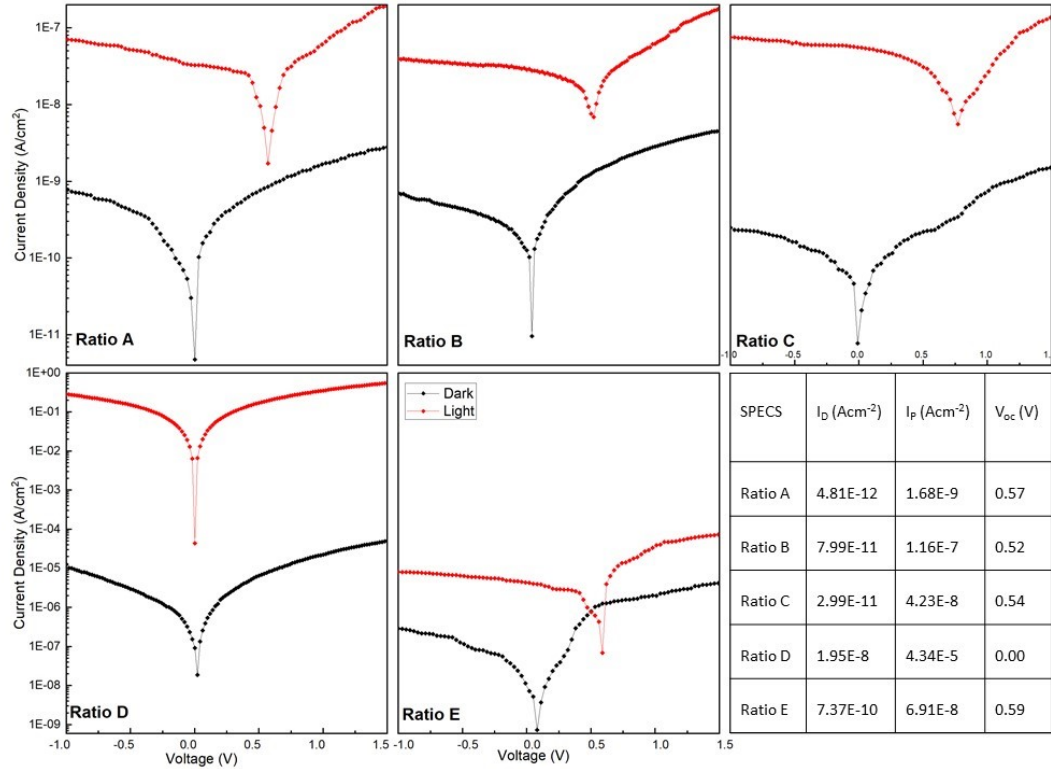| SPECS	I_D (Acm^{-2})	I_P (Acm^{-2})	V_{oc} (V)
Ratio A	4.81E-12	1.68E-9	0.57
Ratio B	7.99E-11	1.16E-7	0.52
Ratio C	2.99E-11	4.23E-8	0.54
Ratio D	1.95E-8	4.34E-5	0.00
Ratio E	7.37E-10	6.91E-8	0.59

Figure 4.13. Representative dark current density-voltage (J-V) curves for the photodetectors with different active layers. The copyright permission is included in the appendix[154]

The disordered nature of solution processing deposition has made the study of the defects in organo-metal halides quite challenging. The discrepancies between the values for defect densities obtained by the first principle studies of density functional theory (DFT) and those obtained experimentally are a requirement for further scrutiny. Defects may be invisible to various techniques due to their positions in the lattice or the charge distribution around them. The defects may also be influenced by the probing signal, as it might cause them to change orientation or equilibrium distribution. Nie et al. discussed the effect of light packets on altering the dynamics of the trap states in these perovskites and suggested a self-healing mechanism[175]. Here, the results of our study were fairly aligned with the first principle findings on these perovskite structures.

It has been shown that perovskite structures display a first-order transition from orthorhombic to tetragonal phase around 165K[152]. In fact, this transition places the cation molecule in a fully disordered configuration. The cation would no longer possess anti-ferroelectric properties to increase exciton recombination rate. At higher temperatures, around 352K, a second-order transition occurs from tetragonal to cubic phase. Pure cubic phase has an O_h symmetry. Thus, the MA cations with C_{3v} symmetry would pose random orientations in a $(PbI3^-)_n$ network. As seen in our XRD results, orthorhombic, tetragonal and cubic phases coexist in the Ratios prepared at a constant temperature, 373K. The Schottky defects in organo-metal halides are mostly referred to as MA^+, Pb^{2+} and I^- instead of MAI and PbI_2[147]. Therefore, the vacancies derived from both Schottky and Frenkel defects can be studied all in one.

Considering all the aforementioned possibilities, a constant trend appeared to explain the effect of excess MAI molecules in the structure of our perovskite materials. Through PL analysis, the spectra for Ratio A was regarded to have the least sub bandgap transitions indicated by its narrow emission band. Assuming Ratio A as the base concentration, the adverse influence of the intrinsic defects was captured in the emission spectra of the other Ratios. Furthermore, the luminescence intensity of the emission band is proportional to L^K, where L is the excitation power and k is an exponent between 0 and 2, presented in Figure 4-10(b). The radiative transition are identified as exciton-like when $1<k<2$ and free-to-bound and donor-acceptor pair transition when $k<1$ [176]. The fairly linear slope of Ratio A demonstrated the exciton like behavior of the material suggesting minimum trap states in the compound.

The different concentrations of disordered organic cations may change the crystallite size and the presence of additional iodide ions may distort the unit cell orientation[162]. The higher

concentration of lead iodide in Ratio D may have caused the lower PL intensity compared with Ratio A. This observation correlated well with XRD results, where Ratio D possessed the smallest crystallite size among other Ratios. A comparison between Ratios B and C showed the change in the functionality of the material based on the concentration of the disordered defects. Although the level of induced intrinsic defects in Ratio B was lower than Ratios C and E, the dominant non-radiative transitions in it produced the lowest PL intensity of all. This observation in Ratio B may be a result of higher defect density in the structure. Another support is the unique k value of <1 for Ratio B, showing a transition related to a defect state and not a free exciton.

The presence of chloride ions in Ratio E changed the lattice structure to the extent that this compound was considered a wide bandgap semiconductor. The absence of room temperature PL in Ratio E may be a result of the change in lattice orientation. Disordered organic compounds give higher photoluminescence than crystalline ones[177, 178]. The incorporation of chloride ions orders the orientation of the unit cell and reduces the effects of induced intrinsic defects. Furthermore, the SEM image of Ratio E illustrated the effect of chloride ions in higher degrees of crystallization as supported by its XRD results[165]. Based on the acquired electrical properties, A and C photosensitive layers had the best performance with arguably very low dark current. Ratio B had a reasonably low dark current density but a wide PL band, indicative of weaker electron-phonon coupling. The level of intrinsic defects in Ratio D resulted in high dark current in the photodetectors. Although photodetectors based on Ratio E established higher dark current density compared with A and C, their application might be different due to the lower absorption wavelength.

Again, these observations were well aligned with the findings of the first principle DFT conducted by other groups[142, 179]. In the event that the concentration of the disordered MAI molecules surrounded by eight PbI_2 octahedrons is not sufficient to form the ideal clusters of $[PbI_6(CH_3NH_3)_n]^m$, the MAI molecules act as trap states[153, 180]. This was the case in Ratio B resulting in the lowest PL intensity, even though it had a high degree of crystallization. Also, adequate concentrations of MAI in Ratios C and E were sufficient to form the clusters. Excess halide ions in these two Ratios may have further acted as dopants, which may be the reasoning for adopting these two structures as the photosensitive layers in addition to the typically used Ratio A[142, 150]. In fact, higher degrees of crystallization in Ratios C and E may reduce the degradation rate in these perovskites.

4.2. Effect of Thickness on the Performance of the Perovskite Image Sensors

In the stacked architecture of the image sensors, the thickness of each layer plays a significant role in the gain of the component. In conventional semiconductors, the Beer-Lambert law describes the attenuation process of the light passing through a light-sensitive matter. However, this law requires correction factors to account for the internal optical electric field distributions inside the organic compounds[181]. Here, the effect of thickness of the light absorbing perovskite layer on the performance of the device was studied. The test devices possessed the same structures with the thickness of the perovskite layer as their only difference. In the first device, the photoactive layer was deposited using spin coating method yielding an active layer with the thickness of 300nm. In the second device, a one-micron thick photoactive layer was produced using dipping method. The current-voltage characteristics of two of the devices is shown in Figure 4.14.
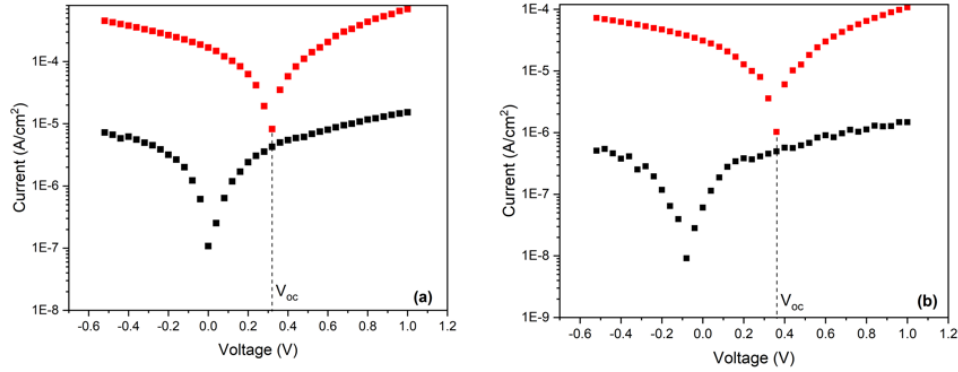
Figure 4.14. I-V characteristics of the devices with (a) thin layer of perovskite (b) thick layer of perovskite in dark (black) and under illumination (red) with a light intensity of 5mWcm^{-2}.

As seen in Figure 4.14, the dark current level decreased by an order of magnitude in the device with a thicker photo-absorbing layer. The photocurrent level is also reduced. This may be attributed to the most likely higher concentration of the defect states in the thicker layer of the perovskite[182]. The open circuit voltage of the device had a slight rise, but the short circuit drop kept the fill factor almost the same in both devices. The mobility of the charge carriers and their diffusion lengths set an upper limit on the thickness of the light absorbing materials. Also, the extension of the depletion width at the interface of the light absorbing materials with the electron and hole transportation layers sets a lower limit on the thickness of the perovskite layer. Although the mobility of the charge carriers in the perovskites is fairly high, an optimized thickness value would include considerations with respect to the modest mobilities of the carriers, 10^{-5} to 10^{-3} cm^2/Vs, in the adjacent layers to the perovskites[183]. The operation of the image sensors in reverse bias mode reduces the effect of poor mobility. However, reverse biasing results in higher dark current levels[184]. A common approach to lower the dark current level is to thicken the photosensitive layer. This approach results in higher shunt resistance but compromises the external quantum efficiency of the device.

4.3. Electron Flow Rectification

In order to enhance rectification characteristics of the image sensors and reduce the recombination rate, the differential of the energy levels between the photosensitive thin film and its adjacent layers were adjusted. This was realized through the substitution of the A site of the perovskite structures. Application of three different cations in the A site of the perovskite has resulted in photovoltaic effects. The first cation is methylammonium which produces high-efficiency perovskite structures with a band gap of 1.5-1.6 eV[185]. As discussed in the stability section of this chapter, methylammonium introduces disorder in the crystalline structure resulting in thermally unstable perovskites.

The presence of methylammonium in the structure leads to the halide segregation instability especially when used in an equimolar ratio with the halides[186]. The second cation is formamidinium which is known for producing thermally and structurally balanced light absorbing perovskites with a band gap of 1.47eV[187]. Long term stability of the formamidinium based perovskites may be guaranteed if the A site is occupied by a combination of formamidinium and cesium (third cation)[36]. In order to optimize the rectifying characteristics of the image sensors methylammonium was substituted by a combination of formamidinium and cesium. The cesium doped perovskite structure established higher shunt resistance. Its superior rectifying marks are shown in Figure 4.15.
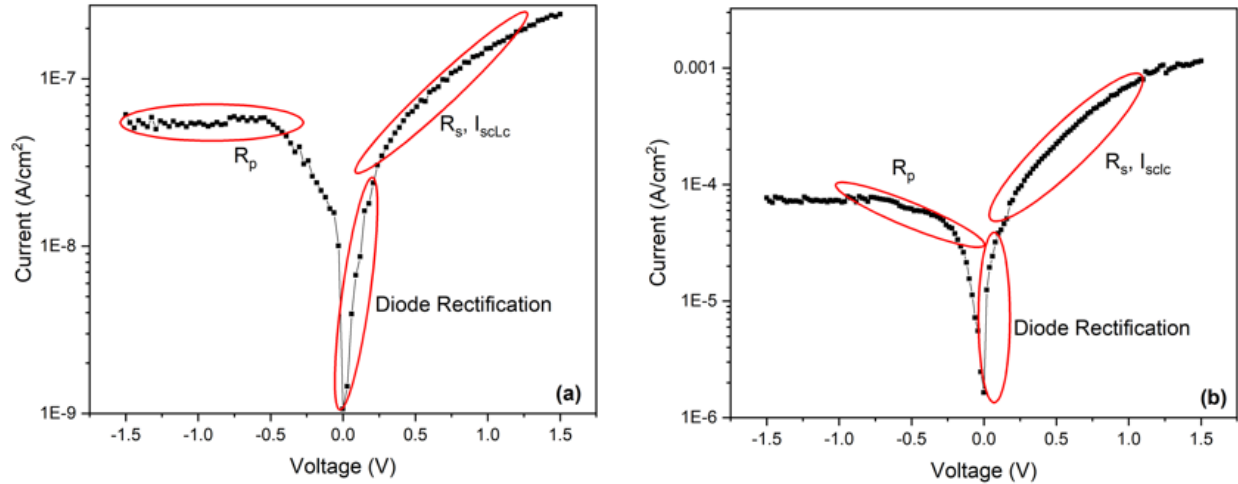
Figure 4.15. I-V characteristics of (a) MAPbI$_3$ and (b)FA$_{0.8}$Cs$_{0.2}$PbI$_3$. The slope of the rectifying section changes from 4.23 to 6.94.

Substitution of methylammonium with a combination of formamidinium and cesium resulted in enhanced rectification. Also, series resistance increased resulting in higher dark current level. This tradeoff is affordable as the yellow phase in the second device was no longer an issue and the devices were more stable over the time.

4.4. Charge Carrier Transportation

4.4.1. Effect of Hole Transporting Layer in Reducing the Recombination Rate

Dark current level is one of the most important characteristics of each image sensor[188]. The dark current level unfolds information regarding the quality of the image sensors, the charge carrier recombination rate and the noise level especially in light-starved application without using active cooling systems[189]. Among different layers of the stacked architecture of a perovskite image sensor, the characteristics of the hole transporting layer, PEDOT:PSS, requires further scrutiny due to the unconventional rules governing its charge transport mechanism. To better understand the role of the hole transporting layer, a buffer layer was employed between the transparent anode and the hole transporting layer. A 1000 Å of tin oxide, SnO$_2$, was sputtered on

83

the indium doped tin oxide, ITO, covered glass substrate. The dark current measurements of three different image sensors with and without this buffer layer is shown in Figure 4.16.
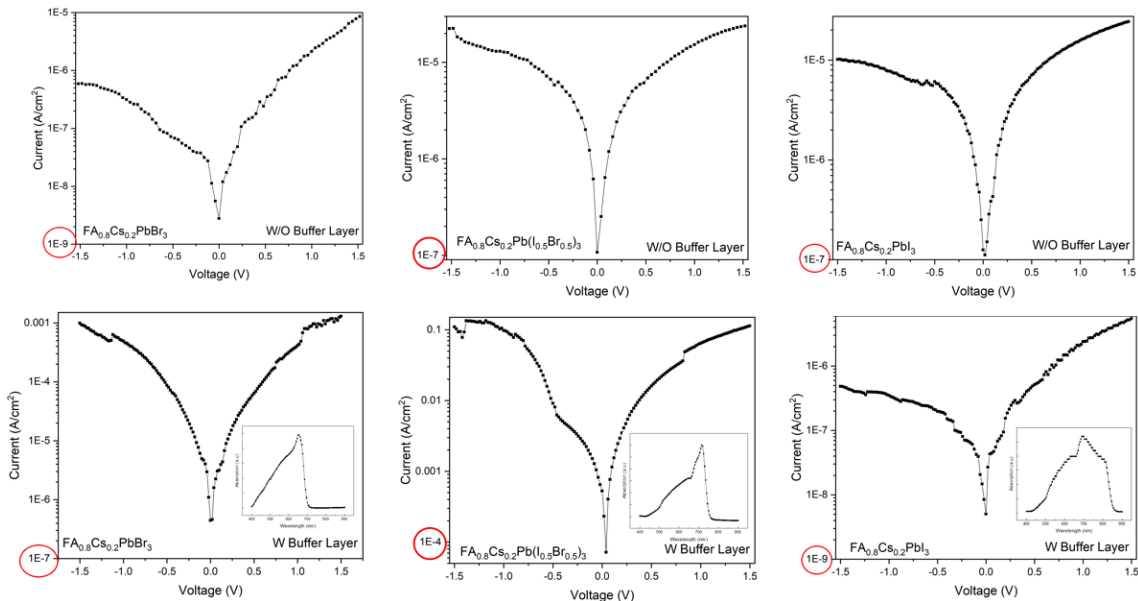
Figure 4.16. Dark current measurements of three different image sensors without and with a buffer layer in their structure.

The diode rectification was compromised in the bromide and bromide/iodide-based image sensors as their leakage current was higher in the presence of the buffer layer. The bromide-based (first column from the left) image sensor displayed the lowest level of dark current without the buffer layer. The bromide/iodide-based image sensor (middle column) showed the highest level of dark current and the iodide-based image sensor (right column) demonstrated improved performance in the presence of the buffer layer. This observation emphasizes the importance of the energy level engineering and the quality of the photoactive layer in the performance of the device.

Although the mobility of the charge carriers in a conducting polymer such as PEDOT:PSS is modest, it does not influence the dark current level drastically. All the image sensors without the buffer layer showcased an arguably low dark current. The presence of the buffer layer

www.manaraa.com

seemed beneficial in the case of the iodide-based image sensors as it may have reduced the leakage current present due to the naturally highly porous structure of iodide-based perovskite layer. It may be worth noting that the surface morphology roughens as the concentration of the iodide in the perovskite precursors increases. Another consideration, in this case, is the generated photocurrents upon illumination. The photocurrent level (not shown on Figure 4.16) is at least two orders of magnitude higher than the dark current in devices without the buffer layer. Whereas the presence of the buffer layer reduces the photocurrent level to only an order of magnitude higher than the dark current level in the devices operating with the buffer layer embedded in their structure. The photocurrent level highlights the minimum adverse effect of the conducting polymer in charge transportation mechanism of these image sensors.

4.4.2. Effect of the Electron Transporting Layer on the Performance of the Image Sensors

The regular concept of the image sensors requires an electron transporting layer, an n-type semiconductor, as its cathode. A fullerene derivative semiconductor such as PCBM may be used to propel the electrons and dissociate the generated exciton inside the light absorbing layer. This layer must be protected against moisture and oxygen. So, a protective layer such as PMMA may be applied on top of the PCBM layer. There are only a few solvents that may dissolve PCBM and serve as an orthogonal solvent for PMMA. Among the organic solvents, acetone dissolves PMMA and is highly volatile. Several devices were fabricated using PCBM (dissolved in toluene) as the electron transporting layer and PMMA (dissolved in acetone) as the protective layer with aluminum contacts. The devices were extremely noisy and improper for image sensing applications.

Devices without the protective layer were not as noisy but demonstrated poor rectifying characteristics even with highly conductive back contacts such as chromium and gold. These devices were degraded in less than a month. Application of a layer of PMMA dissolved in toluene directly on the light absorbing thin film and utilization of highly conductive contacts namely chromium and gold produced higher rectifying characteristics and shunt resistance as shown in Figure 4.17.
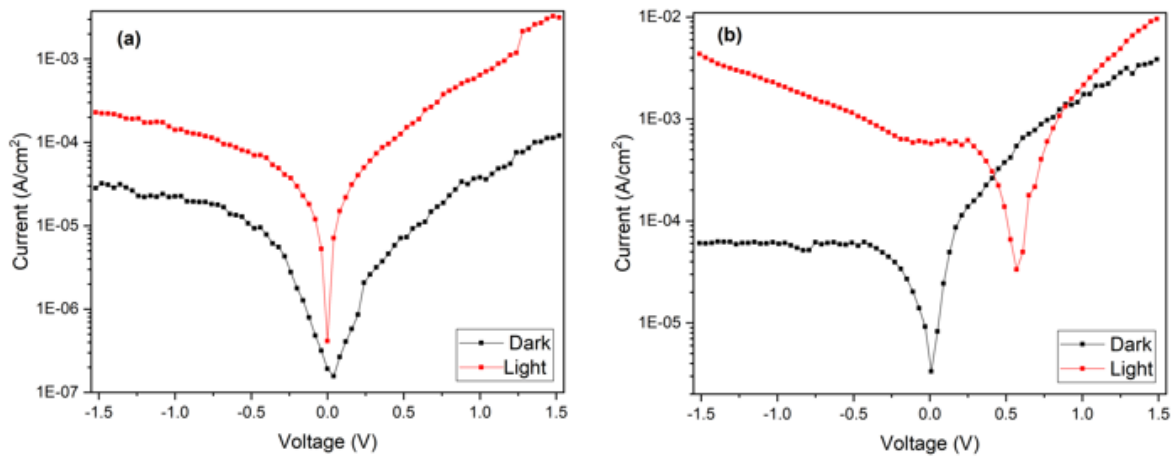
Figure 4.17. IV characteristics of image sensors in dark and light; (a) PCBM on $FA_{0.8}Cs_{0.2}PbBr_3$ and (b) PMMA on $FA_{0.8}Cs_{0.2}PbBr_3$ with Cr/Au as the back contacts, the light intensity of 5mWcm^{-2}.

As shown in the Figure above, the open circuit voltage in the device with PCBM is zero whereas the device with only PMMA on the light absorbing layer shows a 0.57 V in open circuit condition. Also, the photocurrent level in the second device is two orders of magnitude higher than the dark current density. The short-circuit current density in this device is 0.6mA/cm^2 indicating of a highly efficient active area operation. Given PMMA possesses a band gap of 5.6 eV, its energy structure fits right between the conduction bands of perovskite and chromium[190].

86

4.5. Effect of the Additives in Optoelectrical Properties of the Image Sensors

There are several ways to change the characteristics of a semiconductor material or improve them to desired values. Chloride treatment has been proven effective in the cadmium telluride based solar cells. Since chloride has established modifying effects on the performance of light absorbing compound and is also a halide, its effect on the perovskite structures was studied. The chloride atoms were added to the perovskite compound following Vegard's law. The I-V characteristics of the perovskite-based image sensors without and with chloride atoms in their structures is shown in Figure 4.18.
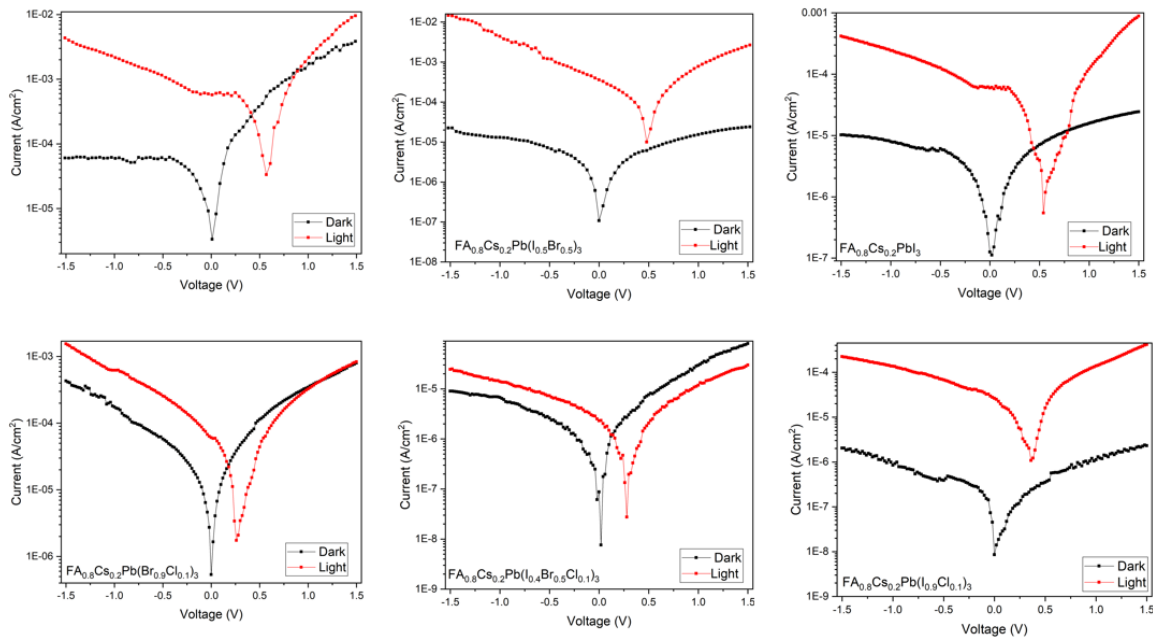
Figure 4.18. I-V Characteristics of image sensors without (top row) and with (bottom row) chloride atoms. The light intensity of 5mWcm^{-2}.

The presence of the chloride atoms reduced the dark current density of the device. It also increased the shunt resistance of the device. The photocurrent density of the devices with chloride in their structure was lower compared with the devices without chloride. This observation correlates with our previous results from the photoluminescence response of the

devices with chloride atoms in their structures. It appears chloride atoms enhance the crystallinity of the perovskite compound (observed in the SEM images reported in Figure 4.12).

Based on several studies, the luminescence response of the highly crystalline structures is lower than those with lower crystallinity[177, 178]. This may be translated to lower absorption rate as well. Lower absorption rate explains the photocurrent level in the plots in the bottom row of Figure 4.18. As concluded in the crystallinity study in this chapter, perovskite structures with only iodide ions are highly porous. Hence, the effect of chloride ions in enhancing the crystallinity of the structure improves the overall response of the iodide-based perovskites in dark and under illumination. This may be the reason behind lower dark current, higher photocurrent and improved rectifying behavior in the devices based on iodide and chloride.

4.6. Color Discrimination in the Image Sensors via Charge Collection Narrowing Mechanism

Light absorption in the perovskite structures is mainly determined based on the absorption characteristics of the active halide elements in it. Different ratios of the halides in the structure alter its absorption pattern across the visible spectrum. Hence, the responsivity of the image sensors changes for different ratios of the halides. The photocurrent level of the image sensors fabricated based on different ratios of bromide and iodide following $MAPb(I_{(1-x)}Br_x)_3$ is shown in Figure 4.19.
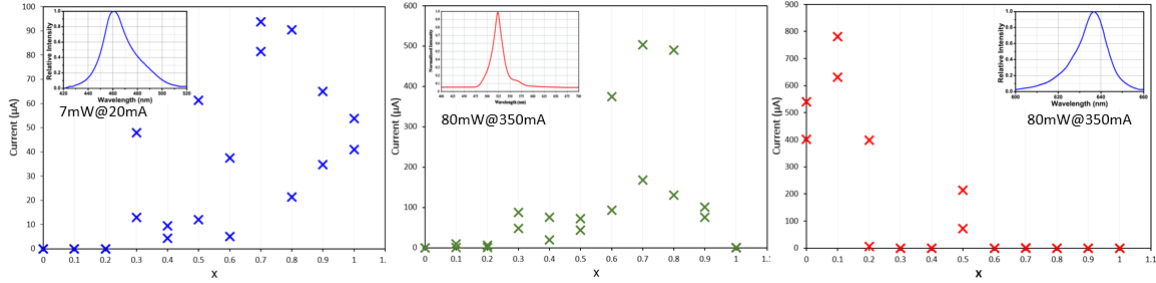
Figure 4.19. Responsivity of the image sensors fabricated based on $MAPb(I_{(1-x)}Br_x)_3$ for varying x values. The inset of each plot includes the absorption spectrum of the diodes used as the light source

The absorption spectrum of three different ratios of the halides in three different image sensors in shown in Figure 4.20. The responsivity of the image sensors displays a blue shift from 800nm for iodide constituents to 650nm for bromide constituents.
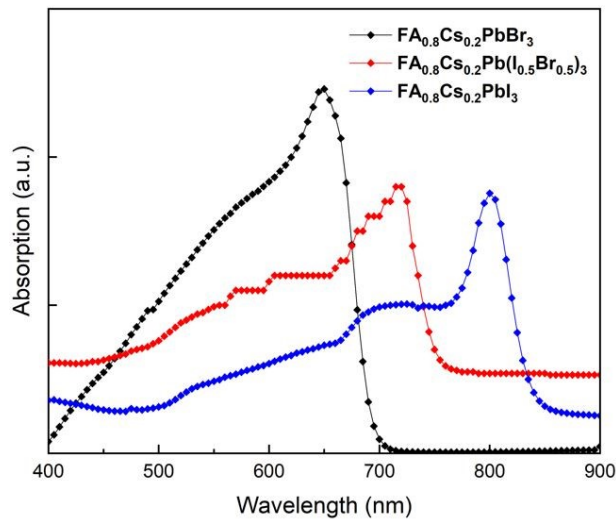
Figure 4.20. Absorption spectrum of the image sensors changes through the visible range as the ratio of the halide varies from 1 to 0.5 and then 0 for each bromide and iodide.

The above Figure shows the tunability over the lower absorption limit in an image sensor through varying halide constituents. For an image sensor to deliver the required color discrimination, an upper absorption limit is required. This requirement may be realized using macromolecules such as synthetic dyes with sharp absorption spectra. The presence of the

89

macromolecules in the perovskite blinds the structure over certain range of frequencies and narrows the bandwidth. The absorption spectrum of the compound of the perovskites and macromolecules were inquired. The collected data was similar to what have been reported in the literature. In this dissertation, methylene blue was examined for the first time for charge collection narrowing purposes. Methylene blue may be considered as a chloride salt. Hence, application of methylene blue serves two purposes, charge collection narrowing and crystallinity enhancement. The effect of additive material in the case of methylene blue was examined and the results indicated the constructive impact of this compound on the crystallinity of the structure. The absorption spectra of three different compounds with and without methylene blue is shown in Figure 4.21.
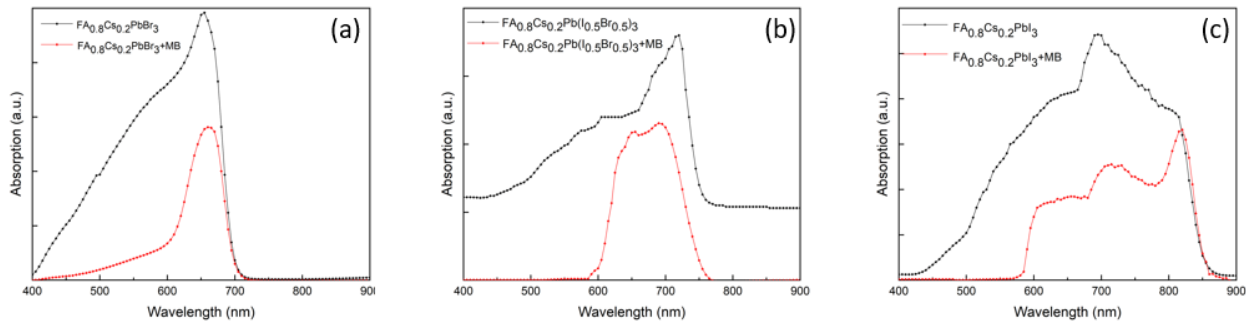
Figure 4.21. Absorption spectrum of image sensors fabricated based on three different perovskite compounds without and with methylene blue (a) bromide-based perovskite structure (b) bromide-iodide based perovskite structure (c) iodide-based perovskite structure

The macromolecules within the perovskite structure form thick bulk (~700nm) heterojunctions. The modest charge transport properties in these thick junctions result in loss in surface photocarrier generation. In fact, the presence of these bulk heterojunctions changes the internal quantum efficiency of the devices and only volume generated photocarriers may be extracted. As seen in the figure above, the spectral response of the devices with methylene blue possess narrow bandwidth and are almost flattened. The spectral response of the devices can be

easily tuned through increasing the concentration of the macromolecules and constructing more junctions. The external quantum efficiency of three different halide ratios without and with methylene blue is shown in Figure 4.22.
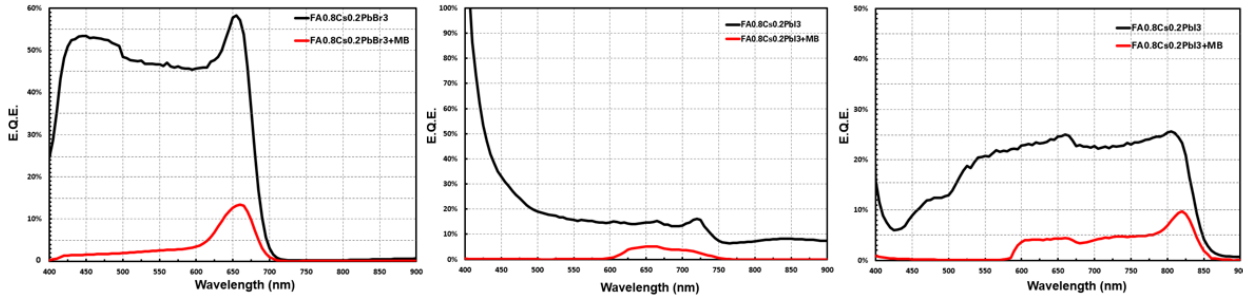
Figure 4.22. External quantum efficiency of the image sensors with different compositions in their active layers (a) bromide-based perovskite (b) bromide-iodide-based perovskite (c) iodide-based perovskites (-3.3V)

The spectral response and consequently the quantum efficiency of the devices vary upon variation in the halide ratios. Although the concentration of the macromolecule was kept constant, the heterojunction thickness varied for each film. This may be due to the crystalline structure of each perovskite compound. Some compounds form higher density and lower porosity structures. The junction in those compounds may be thicker than the junction in compounds with lower density. Thicker junctions result in the extraction of volume generated photocarriers, whereas thin junctions result in extraction of both surface and volume generated photocarriers[191]. Given the bromide structure possess higher quality, the junction thickness in this compound is higher. This justifies the narrow FWHM in the bromide-based perovskite which grows as the ratio of the bromide decreases.

The responses of the image sensors indicate the effectiveness of methylene blue in discriminating red color across the visible range. The FWHM of the absorption spectrum may be tuned only by increasing the concentration of methylene blue in the structure. It should be noted

91

that the halide constituents are the chief parameters in manipulating the internal quantum efficiency. The external quantum efficiency of the image sensors decreases to a considerable degree due to the color discrimination-based detection of the image sensors. To the best of our knowledge, the highest external quantum efficiency for image sensors operating on charge collection narrowing is no more than 15%[191]. The charge collection narrowing in our study resulted in image sensors delivering 10% quantum efficiency in average under -3.3V reverse bias. The responsivity of the image sensors with an average quantum efficiency of 10% is 0.047 (A/W) under a 5mWcm^{-2} irradiance in 0 bias condition. Similar values have been reported for narrowband detectors photodetectors[114, 192]. Considering the noise current to be in picoampere level, the detectivity of the devices are in the order of 10^{11} Jones which is considerably higher than the commercial photodetectors dominating the current detector market.

The photoresponse of the image sensors were measured upon illumination by varying light intensities. The image sensors established a linear dynamic range of over five orders of magnitude under different biasing conditions, conventionally expressed as LDR=100dB. Figure 4.23 shows the linear dynamic range of an image sensor with bromide as its halide and methylene blue in its photoactive layer structure. The deviations from the norm surfaced in higher light intensities. This may be an indication of the presence of bimolecular recombination, a secondary recombination (non-geminate) mechanism in the Beer-Lambert regime[44, 193]. The results indicate the effectiveness of methylene blue in discriminating the color around 650nm with a FWHM of 100nm.
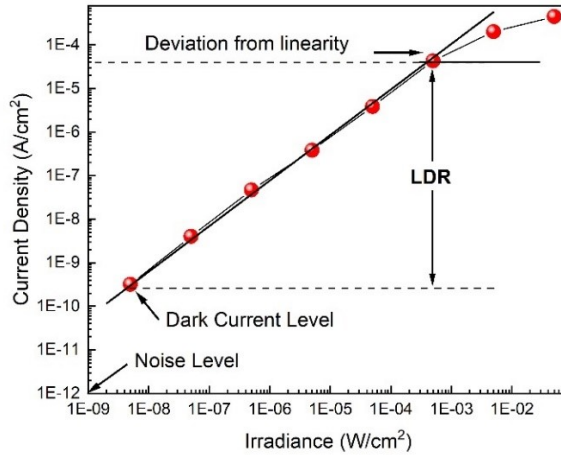
Figure 4.23. Linear Dynamic Range measured at -1V biasing condition for a bromide-based image sensor with methylene blue, the fiber optic light source is a Schott KL 1500.

4.7. Vertically Integrated Hybrid Image Sensors

The electric signals produced by each image sensor must be collected and processed through an application specific integrated circuit and a microprocessor. Integration of a regular concept image sensor with its required circuitry results in a considerable loss in interconnects and may be easily avoided in an inverted concept of the image sensors. This concern led to the realization of the inverted concept of the image sensors in this dissertation. The opaque substrate was a p-type silicon doped with phosphorous (0.74Ω-cm) with 200nm of thermally grown silicon dioxide (to avoid hydrophobicity). The substrate was patterned with 200nm of gold. A layer of PCBM was then deposited on the substrate[3]. The perovskite was spin coated on the layer of PCBM and sandwiched by a layer of PEDOT:PSS, the stack was then encapsulated by a layer of PMMA to avoid ambient exposure. The external quantum efficiency response of the devices with an inverted architecture without and with methylene blue is shown in Figure 4.24.

---

[3] PCBM should be dissolved in chlorobenzene not toluene to avoid hydrophobicity
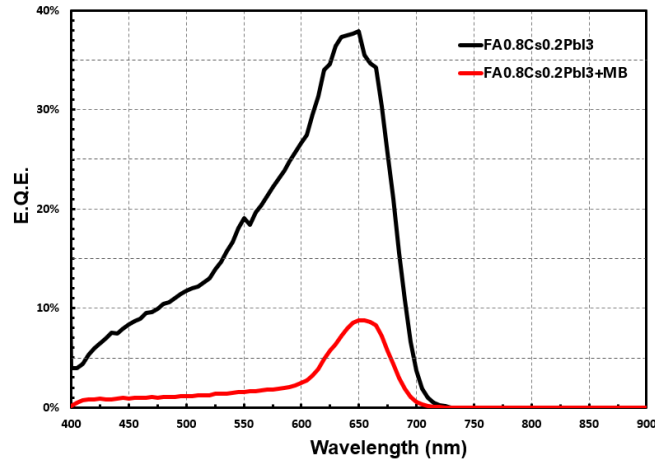
Figure 4.24. External quantum efficiency of hybrid image sensors without methylene blue and with it at 1V biasing.

The narrow peak in the quantum efficiency implies the presence of thick junctions in the stack of materials. The macromolecule sets an upper limit for the bandwidth resulting in color discrimination around 650nm with a FWHM of less than 100nm. The I-V characteristics of the device with and without methylene blue in the perovskite layer is shown in Figure 4.25.
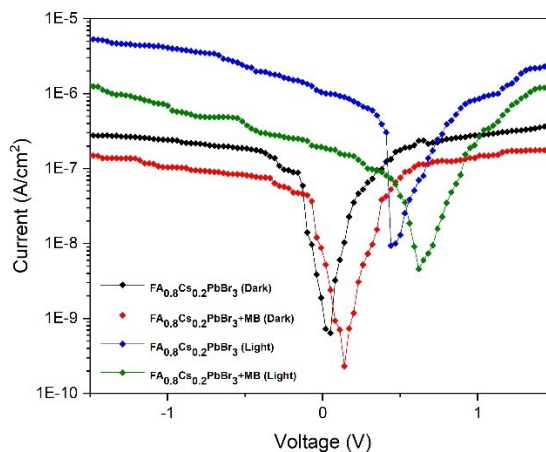
Figure 4.25. I-V characteristics of the vertically integrated perovskite-silicon image sensors without and with methylene blue in their structure. The light source has an intensity of 5mW/cm^2.

The minimum current level for biasing within open circuit voltage to V=1V may be calculated based on exp(qV/nKT) function, Shockley equation for inorganic diodes, where q is the

magnitude of electronic charge, V is the voltage, n is the quality factor, K is Boltzmann constant and T is the temperature. Due to the modest mobility of the charge carriers in organic layers, biasing condition beyond V=1V results in space charge limited current[194]. The dominant space charge limited current bends the current slope downward. Considering V^m with m$\geq$ 2 as the slope indicator, V^4 fits the slope of the current curve the best[195, 196]. In an inverted concept, m=4 implies the existence of the trap states or field dependent mobility of the charge carriers. This may be attributed to the functionality of the oxide in generating interface states which results in accumulation of the charge carriers and change in the electric field[197, 198]. The overall current gain is lower in the inverted concept of the image sensors. The presence of the macromolecule, methylene blue, suppresses the photocurrent even further, which may suggest an underlying space charge limited current condition in charge collection narrowing mechanism.

The linear dynamic range in inverted architecture with the macromolecule is almost 3 orders of magnitude, conventionally stated as 60dB. The reason for the drop in LDR value might not only be the bimolecular recombination, but also the differently formed perovskite microstructure on a silicon dioxide template coated with PCBM. The LDR plot for the image sensor with methylene blue is shown in Figure 4.26.

Tuning the bandwidth of the image sensors results in a responsivity drop from 190 to 24 (mA/W) under a 5mWcm^{-2} irradiance in 0 bias condition. These values still establish a detectivity in the range of 10^{11} Jones which is much higher than the current operating photodiodes in the market[31]. The specific detectivity improves when the system is biased. The reason might be attributed to the trapped photogenerated holes accumulated at the interface of the perovskite

and metal contact. These trapped charge carriers might reduce the height of Schottky barrier and enhance the thermionic current[199].
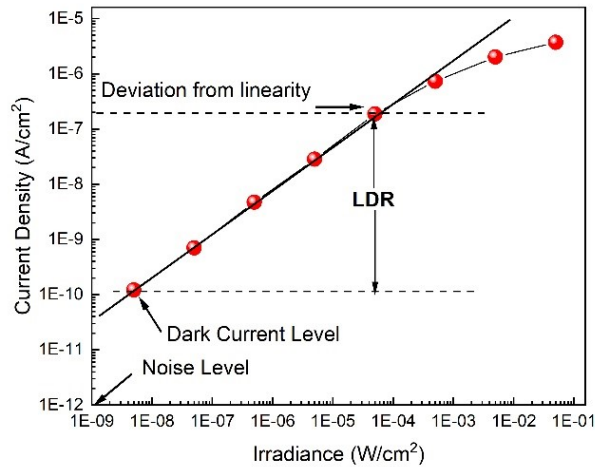
Figure 4.26. Linear Dynamic Range measured at 1V biasing condition for a bromide-based hybrid image sensor with methylene blue, the fiber optic light source is a Schott KL 1500.

The specific detectivity may improve upon downscaling the pixel size to form compact perovskite structures. The high detectivity and facile fabrication process of these image sensors makes them promising candidates for the emerging sensing applications[200].

CHAPTER 5 : CONCLUSION

5.1. Summary

The objective of this dissertation was to design and fabricate vertically integrated hybrid perovskite-silicon image sensor, operating under a specialized charge collection mechanism to detect photons with specific wavelengths. In order to overcome the challenges of the realization process of this objective, several approaches were developed and utilized. First, the principles of the operating mechanism in most of the optoelectronic devices were examined. This included the study of the dye-sensitized solar cells and photosensors as electrochemical units or solid-state devices[84, 201-203]. These studies further clarified the functionality of the light-sensitive structures and organic materials in the architecture of the optoelectronic devices and their performance metrics.

Second, the instability of the perovskite (ABX$_3$) as the most promising solution processable light-absorbing semiconductors was addressed for the purpose of this dissertation[116, 154]. The study was primarily conducted on a dye-sensitized solar cell with perovskite as its light absorbing content. A dynamic restoration of the perovskite structure seemed to resolve the instability of the unit. The study was then expanded to an all-solid-state photodiode and focused on defect engineering of the perovskite to reduce the degradation rate. The results of these studies highlighted the determining role of the counter ion (A site), methylammonium, in the stability of the perovskite-based electronic components. Therefore, a

97

robust combination of counter ions, formamidinium and cesium, was selected to enhance the stability of the perovskite structures.

Third, the X site of the perovskite was hybridized using different ratios of the halides following Vegard's law. These variations altered the sensitivity of the perovskite to different wavelengths across the visible range. The thickness of the light absorbing layer was then optimized. The halide ratios and thicknesses were adjusted to result in extraction of photogenerated charge carriers in both Beer-Lambert and cavity regions. Consequently, the absorption spectra of these perovskite structures were wide with a lower limit (frequency) dictated by the ratio of the halides.

Fourth, a chloride salt called methylene blue was employed in the perovskite structure as a macromolecule. Methylene blue formed optically and electrically thick junctions in the light absorbing layer. High optical density and long charge carrier transit time were the main characteristics of these heterojunctions. These thick heterojunctions only enabled extraction of the charge carriers formed in the cavity region as photogenerated charge carriers in the Beer-Lambert region were most likely recombined before reaching the electron extracting layer. This charge collection narrowing strategy placed the second constraint (upper limit) on the absorption spectrum. Therefore, the lower and upper limits were set through variation of the halide ratio and the utilization of the macromolecule, respectively. Also, there was a trade-off between the external quantum efficiency and full width at half maximum of the absorption spectrum of these narrowband imagers.

Fifth, the bottom-absorbing perovskite-based image sensors were transformed to top-absorbing structures to be vertically integrated with silicon substrates for the state of the art

applications. The inverted concept was achieved by deposition of the cathode on a highly doped silicon. The electron extracting layer, PCBM, was spin coated on top of the cathode. The perovskite layer was then deposited on PCBM layer and sandwiched by a layer of PEDOT:PSS. The performance metrics of the final structure based on only perovskite was remarkably improved in terms of quantum efficiency and consequently responsivity and specific detectivity compared with conventional silicon-based CMOS image sensors.

5.2. Conclusions

An inverted concept of the perovskite-based image sensor was vertically integrated with a highly doped silicon substrate. Even in the proof of concept state of this image sensor, the hybrid component offered performance metrics comparable with the regular concept, bottom absorbing perovskite structure. The photosensitive layer was engineered to confine its absorption spectrum to a full width at half maximum of bellow 100nm. This feature eliminates the requirements of optical accessories such as color filters in the architecture of the image sensors. The specific detectivity of these hybrid imagers is three orders of magnitude greater than the image sensors based on silicon. Practically, the vertical integration of the perovskite structure with silicon increases the fill factor to above the current fill factor of the CMOS imagers which is almost 30%. Theoretically, this fill factor may increase up to 100%. This feature eliminates the requirement of the microlens arrays to concentrate the light on the active area of each pixel. Also, it may reduce the possibility of the cross talk between the pixels to zero. Integration of such inverted concept of the perovskite image sensors with a regular CMOS technology would offer better image sensing quality, and reduce the cost associated with the manufacturing processes in the current imaging technology.

99

5.3. Limitation

Similar to other technology, there may be drawbacks associated with the vertically integrated hybrid perovskite-silicon imagers operating on charge collection narrowing mechanism. Technically, each hybrid pixel may be engineered to detect 100 nm across the visible range with a considerable quantum efficiency. A 2D array of these hybrid pixels might be able to cover the entire visible range and produce accurate color images with minimum color constancy. However, the solution processable nature of the perovskites may introduce complexity to the deposition process as there should be wide pitches between the pixels to avoid material leakage from one pixel to another. This requirement increases the dead area on the chip and may reduce the fill factor.

The current encapsulating layers used in perovskite-based image sensors tend to lose quality and become blurry over the time. This issue reduces the performance of the device considerably and must be fixed. Also, the degradation of the protective layer may expose the perovskite structure to ambient and reduce their lifetime.

5.4. Recommendations for Future Work

Solution processing technique offers a wide range of possibilities in the imaging technology. However, the deposition method of these structures may be reconsidered to enhance the reproducibility of the structures. Evaporation of the precursors have already been examined. Yet, this method may not be suitable for mass production of these image sensors. Single crystalline perovskite structures have displayed outstanding characteristics such as remarkably long diffusion lengths and charge carrier lifetimes. These single crystals are ferroelectric structures and may be deposited on regular CMOS technologies through highly

controlled application of the electric field or manipulation of their piezoelectric property. This approach may steer away from the direction of the optoelectronic technology to an entirely perovskite-based operation.

The incorporation of the macromolecules with the perovskite precursors may be examined by applying a different concentration of the macromolecule on the top of the perovskite and therefore creating color filters with a monolayer thickness on the imaging system. This may be realized using an orthogonal solvent to avoid any possible change in the structure of the perovskite.

REFERENCES

1. Lashof, D.A. and D.R. Ahuja, *Relative contributions of greenhouse gas emissions to global warming.* Nature, 1990. **344**(6266): p. 529.

2. Yaghi, O.M., et al., *Reticular synthesis and the design of new materials.* Nature, 2003. **423**(6941): p. 705.

3. Miller, O.D., E. Yablonovitch, and S.R. Kurtz, *Strong internal and external luminescence as solar cells approach the Shockley–Queisser limit.* IEEE Journal of Photovoltaics, 2012. **2**(3): p. 303-311.

4. Sutter-Fella, C.M., et al., *High photoluminescence quantum yield in band gap tunable bromide containing mixed halide perovskites.* Nano letters, 2015. **16**(1): p. 800-806.

5. Green, M.A., et al., *Solar cell efficiency tables (Version 45).* Progress in photovoltaics: research and applications, 2015. **23**(1): p. 1-9.

6. Seok, S.I., M. Grätzel, and N.G. Park, *Methodologies toward Highly Efficient Perovskite Solar Cells.* Small, 2018: p. 1704177.

7. Ono, L.K., et al., *Perovskite Solar Cells Towards Commercialization.* ACS Energy Letters, 2017. **2**(8): p. 1749-1751.

8. Grätzel, M., *The light and shade of perovskite solar cells.* Nature materials, 2014. **13**(9): p. 838-842.

9. Geske, T., et al., *Deterministic Nucleation for Halide Perovskite Thin Films with Large and Uniform Grains.* Advanced Functional Materials, 2017. **27**(40).

10. Bi, D., et al., *Polymer-templated nucleation and crystal growth of perovskite films for solar cells with efficiency greater than 21%.* Nature Energy, 2016. **1**: p. 16142.

11. Eperon, G.E., et al., *Morphological control for high performance, solution-processed planar heterojunction perovskite solar cells.* Advanced Functional Materials, 2014. **24**(1): p. 151-157.

12. Xiao, M., et al., *A fast deposition-crystallization procedure for highly efficient lead iodide perovskite thin-film solar cells.* Angewandte Chemie, 2014. **126**(37): p. 10056-10061.

13. Zhao, D., et al., *4-Terminal All-Perovskite Tandem Solar Cells Achieving Power Conversion Efficiencies Exceeding 23%.* ACS Energy Letters, 2018.

14. Green, M.A., A. Ho-Baillie, and H.J. Snaith, *The emergence of perovskite solar cells.* Nature Photonics, 2014. **8**(7): p. 506-514.

15. Fthenakis, V. and K. Zweibel. *CdTe PV: Real and perceived EHS risks.* in *Prepared for the NCPV and Solar Program Review Meeting.* 2003.

16. Babayigit, A., et al., *Toxicity of organometal halide perovskite solar cells.* Nature materials, 2016. **15**(3): p. 247-251.

17. Liu, Y., et al., *High Efficiency Tandem Thin-Perovskite/Polymer Solar Cells with a Graded Recombination Layer.* ACS applied materials & interfaces, 2016. **8**(11): p. 7070-7076.

18. Arafat Mahmud, M., et al., *Enhanced stability of low temperature processed perovskite solar cells via augmented polaronic intensity of hole transporting layer.* physica status solidi (RRL)-Rapid Research Letters, 2016. **10**(12): p. 882-889.

19. Richter, S., *The art of the daguerreotype*. 1989: Viking Press.

20. Peres, M.R., *The focal encyclopedia of photography*. 2013: Taylor & Francis.

21. Boyle, W. and G. Smith, *Buried channel charge coupled devices*. 1974, Google Patents.

22. Fossum, E.R. *Active pixel sensors: Are CCDs dinosaurs?* in *Charge-Coupled Devices and Solid State Optical Sensors III*. 1993. International Society for Optics and Photonics.

23. Fossum, E.R. and R. Nixon, *CMOS active pixel sensor type imaging system on a chip*. 1998, Google Patents.

24. Sze, S.M., *Semiconductor devices: physics and technology*. 2008: John Wiley & Sons.

25. Paurazas, S.B., et al., *Comparison of diagnostic accuracy of digital imaging by using CCD and CMOS-APS sensors with E-speed film in the detection of periapical bony lesions.* Oral Surgery, Oral Medicine, Oral Pathology and Oral Radiology, 2000. **89**(3): p. 356-362.

26. Ohta, J., *Smart CMOS image sensors and applications*. 2007: CRC press.

27. Lukac, R., *Single-sensor imaging in consumer digital cameras: a survey of recent advances and future directions.* Journal of Real-Time Image Processing, 2006. **1**(1): p. 45-52.

28. Parker, S.P., *McGraw-Hill concise encyclopedia of science & technology*. 1984: McGraw-Hill.

29. Bharath, A.A. and M. Petrou, *Next generation artificial vision systems: Reverse engineering the human visual system*. 2008: Artech House.

30. Sharma, G. and R. Bala, *Digital color imaging handbook*. 2002: CRC press.

31. Jansen-van Vuuren, R.D., et al., *Organic photodiodes: the future of full color detection and image sensing.* Advanced Materials, 2016. **28**(24): p. 4766-4802.

32. Alharbi, F.H. and S. Kais, *Theoretical limits of photovoltaics efficiency and possible improvements by intuitive approaches learned from photosynthesis and quantum coherence.* Renewable and Sustainable Energy Reviews, 2015. **43**: p. 1073-1089.

33. Fan, J., B. Jia, and M. Gu, *Perovskite-based low-cost and high-efficiency hybrid halide solar cells.* Photonics Research, 2014. **2**(5): p. 111-120.

34. Saparov, B. and D.B. Mitzi, *Organic–inorganic perovskites: structural versatility for functional materials design.* Chemical reviews, 2016. **116**(7): p. 4558-4596.

35. Denton, A.R. and N.W. Ashcroft, *Vegard's law.* Physical review A, 1991. **43**(6): p. 3161.

36. McMeekin, D.P., et al., *A mixed-cation lead mixed-halide perovskite absorber for tandem solar cells.* Science, 2016. **351**(6269): p. 151-155.

37. Fossum, E.R., *CMOS image sensors: Electronic camera-on-a-chip.* IEEE transactions on electron devices, 1997. **44**(10): p. 1689-1698.

38. Baierl, D., et al., *A hybrid CMOS-imager with a solution-processable polymer as photoactive layer.* Nature communications, 2012. **3**: p. 1175.

39. Jansen van Vuuren, R., et al., *Determining the absorption tolerance of single chromophore photodiodes for machine vision.* Applied Physics Letters, 2010. **96**(25): p. 123.

40. El-Desouki, M., et al., *CMOS image sensors for high speed applications.* Sensors, 2009. **9**(1): p. 430-444.

41. Mayr, T., et al., *A simple method to reduce optical cross-talk effects in chemical imaging with planar optodes.* Limnology and Oceanography: Methods, 2012. **10**(2): p. 101-109.

42. Wang, C.-C. and C.G. Sodini. *A crosstalk study on CMOS active pixel sensor arrays for color imager applications*. in *Proc. 2001 International Image Sensors Workshop*. 2001.

43. Wetzelaer, G., et al., *Origin of the dark-current ideality factor in polymer: fullerene bulk heterojunction solar cells.* Applied physics letters, 2011. **99**(15): p. 153506.

44. Stolterfoht, M., et al., *Photocarrier drift distance in organic solar cells and photodetectors.* Scientific reports, 2015. **5**: p. 9949.

45. Guo, F., et al., *A nanocomposite ultraviolet photodetector based on interfacial trap-controlled charge injection.* Nature nanotechnology, 2012. **7**(12): p. 798.

46. Anaraki, E.H., et al., *Highly efficient and stable planar perovskite solar cells by solution-processed tin oxide.* Energy & Environmental Science, 2016. **9**(10): p. 3128-3134.

47. Burschka, J., et al., *Sequential deposition as a route to high-performance perovskite-sensitized solar cells.* Nature, 2013. **499**(7458): p. 316.

48. Im, J.-H., H.-S. Kim, and N.-G. Park, *Morphology-photovoltaic property correlation in perovskite solar cells: One-step versus two-step deposition of CH3NH3PbI3.* Apl Materials, 2014. **2**(8): p. 081510.

49. Jeon, N.J., et al., *Solvent engineering for high-performance inorganic–organic hybrid perovskite solar cells.* Nature materials, 2014. **13**(9): p. 897.

50. Chen, Q., et al., *Planar heterojunction perovskite solar cells via vapor-assisted solution process.* Journal of the American Chemical Society, 2013. **136**(2): p. 622-625.

51. Liang, P.W., et al., *Additive enhanced crystallization of solution-processed perovskite for highly efficient planar-heterojunction solar cells.* Advanced materials, 2014. **26**(22): p. 3748-3754.

52. Liu, M., M.B. Johnston, and H.J. Snaith, *Efficient planar heterojunction perovskite solar cells by vapour deposition.* Nature, 2013. **501**(7467): p. 395.

53. Lin, Q., et al., *Electro-optics of perovskite solar cells.* Nature Photonics, 2015. **9**(2): p. 106.

54. Li, D., et al., *Electronic and ionic transport dynamics in organolead halide perovskites.* ACS nano, 2016. **10**(7): p. 6933-6941.

55. Cho, N., et al., *Pure crystal orientation and anisotropic charge transport in large-area hybrid perovskite films.* Nature communications, 2016. **7**: p. 13407.

56. Zhao, T., et al., *Intrinsic and extrinsic charge transport in CH 3 NH 3 PbI 3 perovskites predicted from first-principles.* Scientific reports, 2016. **6**: p. 19968.

57. Dong, Q., et al., *Electron-hole diffusion lengths> 175 µm in solution-grown CH3NH3PbI3 single crystals.* Science, 2015. **347**(6225): p. 967-970.

58. Eames, C., et al., *Ionic transport in hybrid lead iodide perovskite solar cells.* Nature communications, 2015. **6**: p. 7497.

59. Yang, Z., et al., *Unraveling the Exciton Binding Energy and the Dielectric Constant in Single-Crystal Methylammonium Lead Triiodide Perovskite.* The journal of physical chemistry letters, 2017. **8**(8): p. 1851-1855.

60. Wu, X., et al., *Trap states in lead iodide perovskites.* Journal of the American Chemical Society, 2015. **137**(5): p. 2089-2096.

61. Sum, T.C. and N. Mathews, *Advancements in perovskite solar cells: photophysics behind the photovoltaics.* Energy & Environmental Science, 2014. **7**(8): p. 2518-2534.

62. Peng, J., et al., *Insights into charge carrier dynamics in organo-metal halide perovskites: from neat films to solar cells.* Chemical Society Reviews, 2017. **46**(19): p. 5714-5729.

63. Valverde-Chávez, D.A., et al., *Intrinsic femtosecond charge generation dynamics in single crystal CH 3 NH 3 PbI 3.* Energy & Environmental Science, 2015. **8**(12): p. 3700-3707.

64. Milot, R.L., et al., *Temperature-dependent charge-carrier dynamics in CH3NH3PbI3 perovskite thin films.* Advanced Functional Materials, 2015. **25**(39): p. 6218-6227.

65. Xiao, Z., et al., *Efficient, high yield perovskite photovoltaic devices grown by interdiffusion of solution-processed precursor stacking layers.* Energy & Environmental Science, 2014. **7**(8): p. 2619-2623.

66. Maculan, G., et al., *CH3NH3PbCl3 single crystals: inverse temperature crystallization and visible-blind UV-photodetector.* The journal of physical chemistry letters, 2015. **6**(19): p. 3781-3786.

67. Deng, H., et al., *Growth, patterning and alignment of organolead iodide perovskite nanowires for optoelectronic devices.* Nanoscale, 2015. **7**(9): p. 4163-4170.

68. Li, F., et al., *Ambipolar solution-processed hybrid perovskite phototransistors.* Nature communications, 2015. **6**: p. 8238.

69. Chang, P.-H., et al., *Ultrahigh Responsivity and Detectivity Graphene–Perovskite Hybrid Phototransistors by Sequential Vapor Deposition.* Scientific Reports, 2017. **7**: p. 46281.

70. Huang, M., et al., *Broadband Black-Phosphorus Photodetectors with High Responsivity.* Advanced Materials, 2016. **28**(18): p. 3481-3485.

71. Dong, R., et al., *High-Gain and Low-Driving-Voltage Photodetectors Based on Organolead Triiodide Perovskites.* Advanced materials, 2015. **27**(11): p. 1912-1918.

72. Shen, L., et al., *Improving the sensitivity of a near-infrared nanocomposite photodetector by enhancing trap induced hole injection.* Applied Physics Letters, 2015. **106**(2): p. 3_1.

73. Dou, L., et al., *Solution-processed hybrid perovskite photodetectors with high detectivity.* Nature communications, 2014. **5**: p. 5404.

74. Moehl, T., et al., *Strong photocurrent amplification in perovskite solar cells with a porous TiO2 blocking layer under reverse bias.* The journal of physical chemistry letters, 2014. **5**(21): p. 3931-3936.

75. Kutes, Y., et al., *Direct observation of ferroelectric domains in solution-processed CH3NH3PbI3 perovskite thin films.* The journal of physical chemistry letters, 2014. **5**(19): p. 3335-3339.

76. Sewvandi, G.A., et al., *Antiferroelectric-to-ferroelectric switching in CH 3 NH 3 PbI 3 perovskite and its potential role in effective charge separation in perovskite solar cells.* Physical Review Applied, 2016. **6**(2): p. 024007.

77. Sherkar, T.S. and L.J.A. Koster, *Can ferroelectric polarization explain the high performance of hybrid halide perovskite solar cells?* Physical Chemistry Chemical Physics, 2016. **18**(1): p. 331-338.

78. Slavney, A.H., et al., *Chemical approaches to addressing the instability and toxicity of lead–halide perovskite absorbers.* Inorganic chemistry, 2016. **56**(1): p. 46-55.

79. You, J., et al., *Improved air stability of perovskite solar cells via solution-processed metal oxide transport layers.* Nature nanotechnology, 2016. **11**(1): p. 75.

80. Matteocci, F., et al., *Encapsulation for long-term stability enhancement of perovskite solar cells.* Nano Energy, 2016. **30**: p. 162-172.

81. Azpiroz, J.M., et al., *Defect migration in methylammonium lead iodide and its role in perovskite solar cell operation.* Energy & Environmental Science, 2015. **8**(7): p. 2118-2127.

82. Shao, Y., et al., *Grain boundary dominated ion migration in polycrystalline organic–inorganic halide perovskite films.* Energy & Environmental Science, 2016. **9**(5): p. 1752-1759.

83. Green, M.A. and K. Emery, *Solar cell efficiency tables.* Progress in Photovoltaics: Research and Applications, 1993. **1**(1): p. 25-29.

84. Rahimi, F., T. Tevi, and A. Takshi. *Photoelectrochemical reaction in conducting polymers for solar energy harvesting and charge storage*. in *Next Generation Technologies for Solar Energy Conversion VII*. 2016. International Society for Optics and Photonics.

85. Waldauf, C., et al., *Highly efficient inverted organic photovoltaics using solution based titanium oxide as electron selective contact.* Applied Physics Letters, 2006. **89**(23): p. 233517.

86. Nath, P., *Method of encapsulating a photovoltaic device*. 1993, Google Patents.

87. Bakin, A., et al., *ZnMgO-ZnO quantum wells embedded in ZnO nanopillars: Towards realisation of nano-LEDs.* physica status solidi (c), 2007. **4**(1): p. 158-161.

88. Hua, G., et al., *Fabrication of ZnO nanowire arrays by cycle growth in surfactantless aqueous solution and their applications on dye-sensitized solar cells.* Materials Letters, 2008. **62**(25): p. 4109-4111.

89. Koleske, J.V. *Paint and coating testing manual: of the Gardner-Sward handbook; Paint testing manual*. 1995. ASTM.

90. Kasai, H., et al., *Fabrication and spectroscopic characterization of organic nanocrystals*, in *Handbook of Nanostructured Materials and Nanotechnology*. 2000, Elsevier. p. 433-473.

91. Ryu, K.S., et al., *Electrochemical supercapacitor based on polyaniline doped with lithium salt and active carbon electrodes.* Solid State Ionics, 2004. **175**(1-4): p. 765-768.

92. Ryu, K.S., et al., *Symmetric redox supercapacitor with conducting polyaniline electrodes.* Journal of Power Sources, 2002. **103**(2): p. 305-309.

93. Cao, P.-F., J.D. Mangadlao, and R.C. Advincula, *Stimuli-responsive polymers and their potential applications in oil-gas industry.* Polymer Reviews, 2015. **55**(4): p. 706-733.

94. Ouyang, J., et al., *High-conductivity poly (3, 4-ethylenedioxythiophene): poly (styrene sulfonate) film and its application in polymer optoelectronic devices.* Advanced Functional Materials, 2005. **15**(2): p. 203-208.

95. Fan, B., X. Mei, and J. Ouyang, *Significant conductivity enhancement of conductive poly (3, 4-ethylenedioxythiophene): poly (styrenesulfonate) films by adding anionic surfactants into polymer solution.* Macromolecules, 2008. **41**(16): p. 5971-5973.

96. Lenz, A., et al., *The electronic structure and reflectivity of PEDOT: PSS from density functional theory.* Chemical physics, 2011. **384**(1-3): p. 44-51.

97. Groenendaal, L., et al., *Poly (3, 4-ethylenedioxythiophene) and its derivatives: past, present, and future.* Advanced materials, 2000. **12**(7): p. 481-494.

98. Zhang, F., et al., *Energy level alignment and morphology of interfaces between molecular and polymeric organic semiconductors.* Organic Electronics, 2007. **8**(5): p. 606-614.

99. Shrotriya, V., et al., *Transition metal oxides as the buffer layer for polymer photovoltaic cells.* Applied Physics Letters, 2006. **88**(7): p. 073508.

100. Anthopoulos, T.D., et al., *Solution processable organic transistors and circuits based on a C 70 methanofullerene.* Journal of applied physics, 2005. **98**(5): p. 054503.

101. Kronholm, D. and J.C. Hummelen, *Fullerene-based n-type semiconductors in organic electronics.* Material Matters, 2007. **2**: p. 16-20.

102. Hillson, P. and R. McKay, *Aggregation of dye molecules in aqueous solution a polarographic study.* Transactions of the Faraday Society, 1965. **61**: p. 374-382.

103. Wopschall, R.H. and I. Shain, *Adsorption characteristics of the methylene blue system using stationary electrode polarography.* Analytical Chemistry, 1967. **39**(13): p. 1527-1534.

104. Farag, A. and I. Yahia, *Structural, absorption and optical dispersion characteristics of rhodamine B thin films prepared by drop casting technique.* Optics Communications, 2010. **283**(21): p. 4310-4317.

105. Davidson, A., *The effect of the metal atom on the absorption spectra of phthalocyanine films.* The Journal of Chemical Physics, 1982. **77**(1): p. 168-172.

106. Zhou, Y., et al., *A universal method to produce low–work function electrodes for organic electronics.* Science, 2012. **336**(6079): p. 327-332.

107. Wenk, H.-R. and A. Bulakh, *Minerals: their constitution and origin*. 2016: Cambridge University Press.

108. Shao, S., et al., *Highly Reproducible Sn-Based Hybrid Perovskite Solar Cells with 9% Efficiency.* Advanced Energy Materials, 2018. **8**(4): p. 1702019.

109. Tavakoli, M.M., et al., *Large-Grain Tin-Rich Perovskite Films for Efficient Solar Cells via Metal Alloying Technique.* Advanced Materials, 2018. **30**(11): p. 1705998.

110. Xue, J. and S.R. Forrest, *Carrier transport in multilayer organic photodetectors: I. Effects of layer structure on dark current and photoresponse.* Journal of applied physics, 2004. **95**(4): p. 1859-1868.

111. Montero Martín, J.M., et al., *Trap-limited mobility in space-charge limited current in organic layers.* 2009.

112. Lin, M.-C., *Space-charge effects of electrons and ions on the steady states of field-emission-limited diodes.* Journal of Vacuum Science & Technology B: Microelectronics and Nanometer Structures Processing, Measurement, and Phenomena, 2005. **23**(2): p. 636-639.

113. Yoon, S., et al., *Low dark current inverted organic photodiodes using anionic polyelectrolyte as a cathode interlayer.* Applied Physics Letters, 2017. **110**(8): p. 083301.

114. Armin, A., et al., *Narrowband light detection via internal quantum efficiency manipulation of organic photodiodes.* Nature communications, 2015. **6**: p. 6343.

115. Moulé, A.J., J.B. Bonekamp, and K. Meerholz, *The effect of active layer thickness and composition on the performance of bulk-heterojunction solar cells.* Journal of applied physics, 2006. **100**(9): p. 094503.

116. Rahimi, F., et al., *Photo-electrochemical characterization of CH 3 NH 3 PbI 3 Perovskite deposited on ZnO and TiO 2 mesoporous structures during its dynamic restoration.* Journal of Applied Electrochemistry, 2017. **47**(3): p. 305-313.

117. Kojima, A., et al., *Organometal halide perovskites as visible-light sensitizers for photovoltaic cells.* Journal of the American Chemical Society, 2009. **131**(17): p. 6050-6051.

118. Hashmi, G., et al., *Review of materials and manufacturing options for large area flexible dye solar cells.* Renewable and Sustainable Energy Reviews, 2011. **15**(8): p. 3717-3732.

119. Saliba, M., et al., *A molecularly engineered hole-transporting material for efficient perovskite solar cells.* Nature Energy, 2016. **1**(2): p. 15017.

120. Chen, W., et al., *Efficient and stable large-area perovskite solar cells with inorganic charge extraction layers.* Science, 2015. **350**(6263): p. 944-948.

121. Zhou, Y., et al. *Thermal stress analysis of mesoporous perovskite solar cell by finite element method*. in *Electronic Packaging Technology (ICEPT), 2015 16th International Conference on*. 2015. IEEE.

122. Noel, N.K., et al., *Lead-free organic–inorganic tin halide perovskites for photovoltaic applications.* Energy & Environmental Science, 2014. **7**(9): p. 3061-3068.

123. Niu, G., X. Guo, and L. Wang, *Review of recent progress in chemical stability of perovskite solar cells.* Journal of Materials Chemistry A, 2015. **3**(17): p. 8970-8980.

124. Kim, H.-S., et al., *Lead iodide perovskite sensitized all-solid-state submicron thin film mesoscopic solar cell with efficiency exceeding 9%.* Scientific reports, 2012. **2**: p. 591.

125. Eperon, G.E., et al., *The importance of moisture in hybrid lead halide perovskite thin film fabrication.* ACS nano, 2015. **9**(9): p. 9380-9393.

126. Xu, J., et al., *Integrated Photo-Supercapacitor Based on PEDOT Modified Printable Perovskite Solar Cell.* Advanced Materials Technologies, 2016. **1**(5).

127. Baruah, S. and J. Dutta, *Hydrothermal growth of ZnO nanostructures.* Science and Technology of Advanced Materials, 2009. **10**(1): p. 013001.

128. Lee, S.-W., et al., *Effects of TiCl4 treatment of nanoporous TiO2 films on morphology, light harvesting, and charge-carrier dynamics in dye-sensitized solar cells.* The Journal of Physical Chemistry C, 2012. **116**(40): p. 21285-21290.

129. Son, D.-Y., et al., *11% efficient perovskite solar cell based on ZnO nanorods: an effective charge collection system.* The Journal of Physical Chemistry C, 2014. **118**(30): p. 16567-16573.

130. Chueh, C.-C., C.-Z. Li, and A.K.-Y. Jen, *Recent progress and perspective in solution-processed Interfacial materials for efficient and stable polymer and organometal perovskite solar cells.* Energy & Environmental Science, 2015. **8**(4): p. 1160-1189.

131. Banyamin, Z.Y., et al., *Electrical and optical properties of fluorine doped tin oxide thin films prepared by magnetron sputtering.* Coatings, 2014. **4**(4): p. 732-746.

132. Oku, T., *Crystal structures of CH3NH3PbI3 and related perovskite compounds used for solar cells*, in *Solar Cells-New Approaches and Reviews*. 2015, InTech.

133. Gao, X., et al., *Enhanced photovoltaic performance of perovskite CH 3 NH 3 PbI 3 solar cells with freestanding TiO 2 nanotube array films.* Chemical Communications, 2014. **50**(48): p. 6368-6371.

134. Xiao, Z., et al., *Thin-film semiconductor perspective of organometal trihalide perovskite materials for high-efficiency solar cells.* Materials Science and Engineering: R: Reports, 2016. **101**: p. 1-38.

135. Ogomi, Y., et al., *CH3NH3Sn x Pb (1–x) I3 Perovskite solar cells covering up to 1060 nm.* The journal of physical chemistry letters, 2014. **5**(6): p. 1004-1011.

136. Batalla García, B., et al., *Effect of pore morphology on the electrochemical properties of electric double layer carbon cryogel supercapacitors.* Journal of Applied Physics, 2008. **104**(1): p. 014305.

137. Varshni, Y.P., *Temperature dependence of the energy gap in semiconductors.* physica, 1967. **34**(1): p. 149-154.

138. Fang, Y., et al., *Highly narrowband perovskite single-crystal photodetectors enabled by surface-charge recombination.* Nature Photonics, 2015. **9**(10): p. 679-686.

139. Hao, F., et al., *Lead-free solid-state organic–inorganic halide perovskite solar cells.* Nature Photonics, 2014. **8**(6): p. 489.

140. Serrano-Lujan, L., et al., *Tin-and Lead-Based Perovskite Solar Cells under Scrutiny: An Environmental Perspective.* Advanced Energy Materials, 2015. **5**(20).

141. Ashcroft, N.W., N.D. Mermin, and S. Rodriguez, *Solid state physics.* American Association of Physics Teachers, 1998.

142. Kim, J., et al., *The role of intrinsic defects in methylammonium lead iodide perovskite.* The journal of physical chemistry letters, 2014. **5**(8): p. 1312-1317.

143. Park, N.-G., et al., *Towards stable and commercially available perovskite solar cells.* Nature Energy, 2016. **1**(11): p. 16152.

144. Green, M.A., et al., *Solar cell efficiency tables (version 50).* Progress in Photovoltaics: Research and Applications, 2017. **25**(7): p. 668-676.

145. Aristidou, N., et al., *Fast oxygen diffusion and iodide defects mediate oxygen-induced degradation of perovskite solar cells.* Nature Communications, 2017. **8**: p. 15218.

146. Mosconi, E., et al., *First-principles modeling of mixed halide organometal perovskites for photovoltaic applications.* The Journal of Physical Chemistry C, 2013. **117**(27): p. 13902-13913.

147. Walsh, A., et al., *Self-Regulation Mechanism for Charged Point Defects in Hybrid Halide Perovskites.* Angewandte Chemie International Edition, 2015. **54**(6): p. 1791-1794.

148. Motta, C., et al., *Revealing the role of organic cations in hybrid halide perovskite CH 3 NH 3 PbI 3.* Nature communications, 2015. **6**: p. 7026.

149. Varadwaj, A., P.R. Varadwaj, and K. Yamashita, *Hybrid organic–inorganic CH3NH3PbI3 perovskite building blocks: Revealing ultra-strong hydrogen bonding and mulliken inner complexes and their implications in materials design.* Journal of computational chemistry, 2017. **38**(32): p. 2802-2818.

150. Sakai, N., et al., *The mechanism of toluene-assisted crystallization of organic–inorganic perovskites for highly efficient solar cells.* Journal of Materials Chemistry A, 2016. **4**(12): p. 4464-4471.

151. Lewis, A.E., et al., *Unveiling the Concentration-Dependent Grain Growth of Perovskite Films from One-and Two-Step Deposition Methods: Implications for Photovoltaic Application.* ACS applied materials & interfaces, 2017. **9**(30): p. 25063-25066.

152. Weller, M.T., et al., *Complete structure and cation orientation in the perovskite photovoltaic methylammonium lead iodide between 100 and 352 K.* Chemical Communications, 2015. **51**(20): p. 4180-4183.

153. Mashiyama, H., et al., *Disordered Configuration of Methylammonium of CH3NH3PbBr3 Determined by Single Crystal Neutron Diffractometry.* Ferroelectrics, 2007. **348**(1): p. 182-186.

154. Fatemeh Rahimi, S.P.C., Christos Ferekides, Andrew M. Hoff, *Methylammonium iodide and its effect as an intrinsic defect in perovskite structure and device performance* 2018.

155. D'Innocenzo, V., et al., *Tuning the light emission properties by band gap engineering in hybrid lead halide perovskite.* Journal of the American Chemical Society, 2014. **136**(51): p. 17730-17733.

156. Vorpahl, S.M., et al., *Impact of microstructure on local carrier lifetime in perovskite solar cells.* Science, 2015: p. aaa5333.

157. Pelant, I. and J. Valenta, *Luminescence spectroscopy of semiconductors*. 2012: Oxford University Press.

158. Wright, A.D., et al., *Electron–phonon coupling in hybrid lead halide perovskites.* Nature communications, 2016. **7**: p. 11755.

159. Mashiyama, H., Y. Kurihara, and T. Azetsu, *Disordered cubic perovskite structure of CH3NH3PbX3 (X= Cl, Br, I).* Journal of the Korean Physical Society, 1998. **32**: p. S156-S158.

160. Poglitsch, A. and D. Weber, *Dynamic disorder in methylammoniumtrihalogenoplumbates (II) observed by millimeter-wave spectroscopy.* The Journal of chemical physics, 1987. **87**(11): p. 6373-6378.

161. Baikie, T., et al., *Synthesis and crystal chemistry of the hybrid perovskite (CH 3 NH 3) PbI 3 for solid-state sensitised solar cell applications.* Journal of Materials Chemistry A, 2013. **1**(18): p. 5628-5641.

162. Whitfield, P., et al., *Structures, Phase Transitions and Tricritical Behavior of the Hybrid Perovskite Methyl Ammonium Lead Iodide.* Scientific reports, 2016. **6**: p. 35685.

163. Luo, S. and W.A. Daoud, *Crystal Structure Formation of CH3NH3PbI3-xClx Perovskite.* Materials, 2016. **9**(3): p. 123.

164. Batsanov, S., *The concept of electronegativity and structural chemistry*. Vol. 15. 1990: CRC Press.

165. Wilkinson, A.P., et al., *In situ x-ray diffraction study of crystallization kinetics in PbZr1-xTixO3,(PZT, x= 0.0, 0.55, 1.0).* Chemistry of Materials, 1994. **6**(6): p. 750-754.

166. Edri, E., et al., *Why lead methylammonium tri-iodide perovskite-based solar cells require a mesoporous electron transporting scaffold (but not necessarily a hole conductor).* Nano letters, 2014. **14**(2): p. 1000-1004.

167. Coll, M., et al., *Polarization switching and light-enhanced piezoelectricity in lead halide perovskites.* The journal of physical chemistry letters, 2015. **6**(8): p. 1408-1413.

168. Quarti, C., et al., *Structural and optical properties of methylammonium lead iodide across the tetragonal to cubic phase transition: implications for perovskite solar cells.* Energy & Environmental Science, 2016. **9**(1): p. 155-163.

169. Shaw, T., S. Trolier-McKinstry, and P. McIntyre, *The properties of ferroelectric films at small dimensions.* Annual Review of Materials Science, 2000. **30**(1): p. 263-298.

170. Li, X. and J. Wang, *Effect of grain size on the domain structures and electromechanical responses of ferroelectric polycrystal.* Smart Materials and Structures, 2016. **26**(1): p. 015013.

171. Murduck, J., et al., *A low-inductance, low-I/sub c/HTS junction process.* IEEE transactions on applied superconductivity, 1997. **7**(2): p. 2940-2943.

172. Im, J.-H., et al., *Growth of CH3NH3PbI3 cuboids with controlled size for high-efficiency perovskite solar cells.* Nature nanotechnology, 2014. **9**(11): p. 927-932.

173. Armin, A., et al., *Thick junction broadband organic photodiodes.* Laser & Photonics Reviews, 2014. **8**(6): p. 924-932.
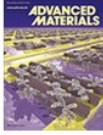
174. Lyons, D.M., et al., *Narrow band green organic photodiodes for imaging.* Organic Electronics, 2014. **15**(11): p. 2903-2911.

175. Nie, W., et al., *Light-activated photocurrent degradation and self-healing in perovskite solar cells.* Nature communications, 2016. **7**: p. 11574.

176. Schmidt, T., K. Lischka, and W. Zulehner, *Excitation-power dependence of the near-band-edge photoluminescence of semiconductors.* Physical Review B, 1992. **45**(16): p. 8989.

177. Stoumpos, C.C., C.D. Malliakas, and M.G. Kanatzidis, *Semiconducting tin and lead iodide perovskites with organic cations: phase transitions, high mobilities, and near-infrared photoluminescent properties.* Inorganic chemistry, 2013. **52**(15): p. 9019-9038.

178. Pizani, P., et al., *Photoluminescence of disordered ABO 3 perovskites.* Applied Physics Letters, 2000. **77**(6): p. 824-826.

179. Saffari, M., et al., *DFT analysis and FDTD simulation of CH3NH3PbI3− x Cl x mixed halide perovskite solar cells: role of halide mixing and light trapping technique.* Journal of Physics D: Applied Physics, 2017. **50**(41): p. 415501.

180. Varadwaj, P.R., A. Varadwaj, and K. Yamashita, *Why Do Eight Units of Methylammonium Enclose PbI6 Octahedron in Large-Scale Crystals of Methylammonium Lead Iodide Perovskite Solar Cell? An Answer from First-Principles Study.* arXiv preprint arXiv:1704.05691, 2017.

181. Pettersson, L.A., L.S. Roman, and O. Inganäs, *Modeling photocurrent action spectra of photovoltaic devices based on organic thin films.* Journal of Applied Physics, 1999. **86**(1): p. 487-496.

182. Landi, G., et al., *Correlation between electronic defect states distribution and device performance of perovskite solar cells.* Advanced Science, 2017. **4**(10).

183. Armin, A., et al., *Balanced Carrier Mobilities: Not a Necessary Condition for High-Efficiency Thin Organic Solar Cells as Determined by MIS-CELIV.* Advanced Energy Materials, 2014. **4**(4).

184. Goodman, A.M. and A. Rose, *Double Extraction of Uniformly Generated Electron-Hole Pairs from Insulators with Noninjecting Contacts.* Journal of Applied Physics, 1971. **42**(7): p. 2823-2830.

185. Jeon, N.J., et al., *Compositional engineering of perovskite materials for high-performance solar cells.* Nature, 2015. **517**(7535): p. 476.

186. Conings, B., et al., *Intrinsic thermal instability of methylammonium lead trihalide perovskite.* Advanced Energy Materials, 2015. **5**(15).

187. Eperon, G.E., et al., *Formamidinium lead trihalide: a broadly tunable perovskite for efficient planar heterojunction solar cells.* Energy & Environmental Science, 2014. **7**(3): p. 982-988.

188. Lin, W.-S., G.-M. Sung, and J.-L. Lin, *High performance CMOS light detector with dark current suppression in variable-temperature systems.* Sensors, 2016. **17**(1): p. 15.

189. Culurciello, E., R. Etienne-Cummings, and K.A. Boahen, *A biomorphic digital image sensor.* IEEE Journal of Solid-State Circuits, 2003. **38**(2): p. 281-294.

190. Sarkar, P.K., et al., *Incorporation of SnO 2 nanoparticles in PMMA for performance enhancement of a transparent organic resistive memory device.* RSC Advances, 2015. **5**(128): p. 105661-105667.

191.   Lin, Q., et al., *Filterless narrowband visible photodetectors.* Nature Photonics, 2015. **9**(10): p. 687-694.

192.   Li, D., et al., *High performance organic-inorganic perovskite-optocoupler based on low-voltage and fast response perovskite compound photodetector.* Scientific reports, 2015. **5**: p. 7902.

193.   Koster, L.J.A., et al., *Quantifying bimolecular recombination losses in organic bulk heterojunction solar cells.* Advanced Materials, 2011. **23**(14): p. 1670-1674.

194.   Jain, S., et al., *Injection-and space charge limited-currents in doped conducting organic materials.* Journal of applied physics, 2001. **89**(7): p. 3804-3810.

195.   Montero, J.M. and J. Bisquert, *Interpretation of trap-limited mobility in space-charge limited current in organic layers with exponential density of traps.* Journal of Applied Physics, 2011. **110**(4): p. 043705.

196.   Kumar, A., S. Sista, and Y. Yang, *Dipole induced anomalous S-shape I-V curves in polymer solar cells.* Journal of Applied Physics, 2009. **105**(9): p. 094512.

197.   Jørgensen, M., K. Norrman, and F.C. Krebs, *Stability/degradation of polymer solar cells.* Solar energy materials and solar cells, 2008. **92**(7): p. 686-714.

198.   Krebs, F.C. and K. Norrman, *Analysis of the failure mechanism for a stable organic photovoltaic during 10 000 h of testing.* Progress in Photovoltaics: Research and Applications, 2007. **15**(8): p. 697-712.

199.   Liu, L., et al., *High-detectivity ultraviolet photodetectors based on laterally mesoporous GaN.* Nanoscale, 2017. **9**(24): p. 8142-8148.

200.   Razzak, M.I., S. Naz, and A. Zaib, *Deep Learning for Medical Image Processing: Overview, Challenges and the Future*, in *Classification in BioApps*. 2018, Springer. p. 323-350.

201.   Rahimi, F. and A. Takshi. *Energy storage capability of the dye sensitized solar cells via utilization of highly porous carbon electrodes*. in *Next Generation Technologies for Solar Energy Conversion VII*. 2016. International Society for Optics and Photonics.

202.   Takshi, A., T. Tevi, and F. Rahimi. *Organic photovoltaic devices with concurrent solar energy harvesting and charge storage capability*. in *Next Generation Technologies for Solar Energy Conversion VI*. 2015. International Society for Optics and Photonics.

203.   Takshi, A., J. Bebeau, and F. Rahimi. *Perovskite based photosensor for electrochemical studies*. in *Organic Sensors and Bioelectronics IX*. 2016. International Society for Optics and Photonics.

APPENDIX A: COPYRIGHT PERMISSIONS

The permission below is for the use of material in Figure 2.1.

The permission below is for the use of material in Figure 2.3.

Copyright Status

NREL-authored documents are sponsored by the U.S. Department of Energy under Contract DE-AC36-08GO28308. Accordingly, with respect to such documents, the U.S. Government and others acting on its behalf retain a paid-up nonexclusive, irrevocable world-wide license to reproduce, prepare derivative works, distribute copies to the public, and perform publicly and display publicly, by or on behalf of the Government. Use of documents available from or referenced by this server may be subject to U.S. and foreign Copyright Laws.

The permission below is for the use of material in Figure 2.5.

The permission below is for the use of material in Figure 3.8.

The permission below is for the use of material in Figure 3.9.

The permission below is for the use of material in Figure 3.12.

The permission below is for the use of material in Figure 3.15.

The permission below is for the use of material in part 4.1.1 including Figure 4.1-4.7.